A Fuel-Cell Vehicle Test Station

by

Michelle I. Thorne

A thesis

presented to the University of Waterloo

in fulfillment of the

thesis requirement for the degree of

Master of Applied Science

in

Electrical and Computer Engineering

Waterloo, Ontario, Canada, 2008

AUTHOR'S DECLARATION

I hereby declare that I am the sole author of this thesis. This is a true copy of the thesis, including any required final revisions, as accepted by my examiners.

I understand that my thesis may be made electronically available to the public.

Abstract

Due to concerns about energy security, rising oil prices, and adverse effects of internal combustion engine vehicles on the environment, the automotive industry is quickly moving towards developing efficient "green" vehicles. Fuel cell-powered vehicles offer high efficiency and practically zero emissions. The main obstacles for widespread commercial production of fuel cell vehicles are high cost and short lifetime of fuel cell stacks, lack of a hydrogen infrastructure, and generation of hydrogen in an environmentally-friendly manner and its storage. Using actual fuel cells and actual vehicular loads in the study of fuel cell vehicular systems can be prohibitive due to cost (initial and running) and safety issues. It is very desirable to have a test station that emulates a vehicle with a high degree of accuracy and flexibility to alleviate cost and safety issues.

This thesis proposes a design for a test station that emulates the drive train of a typical fuel cell-powered vehicle that is equipped with regenerative braking capability. As part of the test station, a fuel cell emulator is designed and validated through simulation based on the Nexa Fuel Cell power module manufactured by Ballard Power Systems.

As another building block for the test station, a bi-directional controllable DC load is developed that can realize a given drive cycle for the scaled-down version of a given vehicle. The load allows simulation of regenerative braking capability. The performance of the load is validated through simulation.

A DC-DC boost converter for controlling the fuel cell power, as well as an energy storage system for assisting the fuel cell in providing the required power during high-demand periods, are incorporated into the proposed test station. Simulation results are used to show that the test station is capable of simulating the real-life conditions experienced by actual fuel cell vehicles on the road. The test station, when realized by hardware, can be used for performing a wide range of studies on the drive train architecture and power management of fuel cell vehicles.

Acknowledgements

I would like to acknowledge my professor, Dr. Kazerani, for all his guidance and invaluable advice during this program. I would also like to thank all my friends and research colleagues for all the help they have given me. Whenever I needed help brain storming or assistance in performing a task they always leant a helping hand. You have my gratitude.

I would like to thank my parents for encouraging me to take this step in my career. They have always been great teachers to me and have always pushed me to do my best. I also want to thank my in-laws for all of their support when I needed it most.

Lastly, I would like to thank my husband, Stephen, for all of his love, support, and devotion. He is the source of my strength. Without him, I would not have been able to complete this program.

Dedication

For my loving husband who is the source of all my inspiration…

Table of Contents

List of Figures

List of Tables

List of Acronyms

AC	Alternating Current
AFC	Alkaline Fuel Cells
BU	Battery Unit
CO_2	Carbon Dioxide
DBR	Diode Bridge Rectifier
DC	Direct Current
EPA	Environmental Protection Agency
FC	Fuel Cell
FCE	Fuel Cell Emulator
FCHV	Fuel Cell Hybrid Vehicle
FCV	Fuel Cell Vehicle
GM	General Motors
H_3PO_4	Phosphoric Acid
KCL	Kirchhoff's Current Law
KOH	Potassium Hydroxide
MEA	Membrane Electrode Assembly
MPPT	Maximum Power Point Tracking
NaOH	Sodium Hydroxide
NASA	National Aeronautics and Space Administration
PAFC	Phosphoric Acid Fuel Cell
PEM/PEMFC	Polymer Electrolyte Membrane Fuel Cell
PFC	Power Factor Correction
PI	Proportional and Integral controller
PSIM	Power electronic simulation software package by PowerSim Inc.
PV	Photovoltaic
PWM	Pulse Width Modulation
RMS	Root Mean Square
SCR	Silicon Controlled Rectifier

SLPM	Standard Liters per Minute
SOC	State-of-charge
SPE	Solid Polymer Electrolyte
UC	Ultra-capacitor

Chapter 1

Introduction

1.1 Background and Motivation

As traditional fuel sources become scarce and the fear of global warming grows, researchers turn their attention to new energy sources. Solar and wind power are the most popular and well known renewable sources, followed by geothermal, hydroelectric, and bio-fuel. Bio-fuel is the only candidate listed above that can be applied to moving vehicles. Gasoline is mixed with plant and/or animal oils to produce a cleaner burning fuel. E85, which is the most popular, is being introduced in parts of North America. It is composed of 85% ethanol and 15% gasoline to reduce vehicle emissions by up to 40%. While this new fuel is more economical and environmentally friendly, this is only a short-term solution to fuel shortages and reversing the damage to the planet. Emissions must be reduced to 0%. A new and fast growing solution that incorporates using a renewable fuel and produces zero emissions is fuel cells, rendering the internal combustion engine obsolete [1].

Fuel cells produce electricity from a chemical reaction where the by-product is water. This fact makes fuel cells extremely attractive for eliminating emissions. One disadvantage of fuel cells is their slow response time. This will be explained in more detail in chapter 2. To solve this problem, energy storage devices are often incorporated into power management systems to ensure all sources of energy as well as the load(s) operate correctly and within safety parameters.

A simple fuel cell-powered hybrid energy system, shown in Figure 1.1, is introduced in [2]. It is simply a fuel cell, connected to a load through a DC-DC converter. The converter used is a buck converter which steps the voltage down from the output of the fuel cell to the input of the load. It is not clear what load was used in this study; however, lowering the voltage results in an increase in current. A high current requires larger wires and more expensive components, as well as higher

magnetic and electric fields and can be dangerous in a small laboratory environment. If the load requires a large current then this is unavoidable; however, every effort should be made to reduce the current.

To compensate for the slow response time of the fuel cell, a storage battery is connected in parallel to the load on the high-voltage DC bus through a battery controller. The battery that was used for this study was a lead-acid battery [2]. Lead-acid batteries are not very desirable because they are very large and heavy with a low energy to volume ratio. Charging and discharging safely and efficiently can take a relatively long period of time. If the batteries are not maintained, they can be dangerous to use and hazardous to the environment. The battery controller is nothing more than a switch that controls the battery current which then stabilizes the load current during load changes.

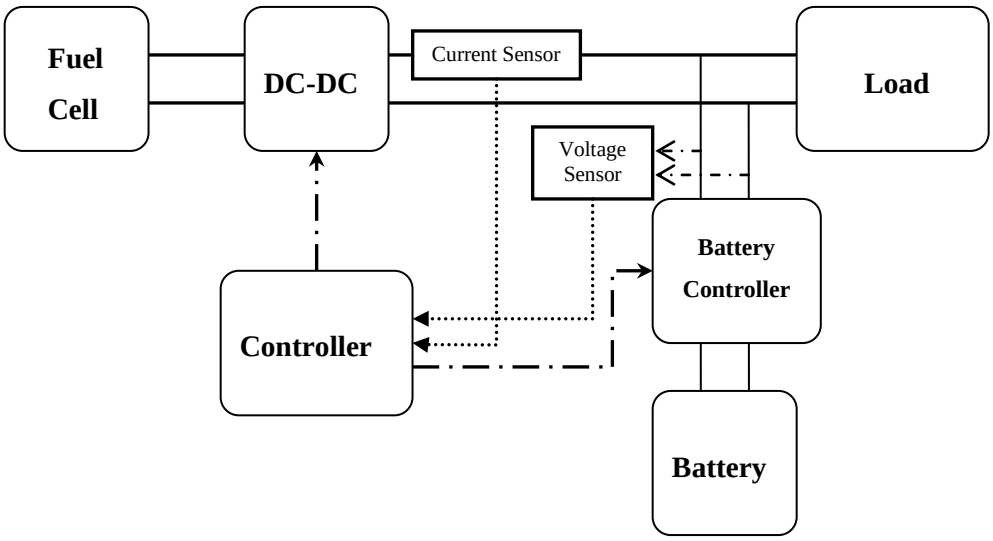

Figure 1.1 A fuel cell-powered hybrid energy system [2].

The controllers manage the power by incorporating a current loop to control the charging and discharging of the battery and a voltage loop to control the output voltage of the buck converter [2]. This control scheme attempts to control two variables instead of one. These two variables are related by the amount of power drawn by the load, so there is no need to control both of them. The voltage on the high-voltage DC bus can be maintained by both the battery (if connected directly to the bus)

and by the output of the converter. If the load requests a change in power, the current will change automatically based on conservation of power and KCL. While the concept of this power management scheme is sound, this is not the best implementation to propel a vehicle, for several reasons. First, a buck converter is used which means the fuel cell has to output a higher voltage than is used. This results in needing a larger and more expensive fuel cell than is really needed and can possibly introduce losses into the system. Second, lead-acid batteries are used for storage. Lead-acid batteries are one of the heaviest batteries available. When designing a propulsion system for a vehicle, lighter components are preferable so that less energy is needed to propel the vehicle forward. Third, the control system is more complicated than it needs to be. Both voltage and current do not need to be controlled. Only one should be controlled, and the other will adjust based on the power level of the system.

A similar topology, shown in Figure 1.2, was used by Honda in the design of the Honda FCX hydrogen fuel cell automobile. A buck converter was used in conjunction with an ultra-capacitor instead of a battery [3]. Using an ultra-capacitor is an improvement over the previously discussed topology. An ultra-capacitor can charge and discharge more quickly, maintain the voltage on the high-voltage DC bus, and is much lighter than a lead-acid battery. However, employing a buck converter, which the designers called a voltage control unit, does not result in the best use of the fuel cell. Decreasing the voltage will increase the current increasing costs and safety concerns. Also, by decreasing the voltage with a buck converter requires that the fuel cell has a larger output voltage than required by the load, making it more expensive than when a smaller fuel cell is used with a boost converter.

Another topology that was introduced in [4] used a multi-input, single-output converter. This converter can be constructed from a three-phase AC-DC converter. Each phase is a DC-DC boost converter, with two of the branches having a bi-directional capability. Each phase of the converter will control one of three power sources: a fuel cell (FC), a battery unit (BU), which is made up of lead-acid batteries, and an ultra-capacitor bank (UC). This topology is shown in Figure 1.3. By using all three sources, the size of the fuel cell can be decreased even more, making the system more

economical. The battery unit provides the difference in the power requested by the vehicle and the power the fuel cell is able to provide. During these small power transients, the battery unit can charge and discharge through a bi-directional converter.

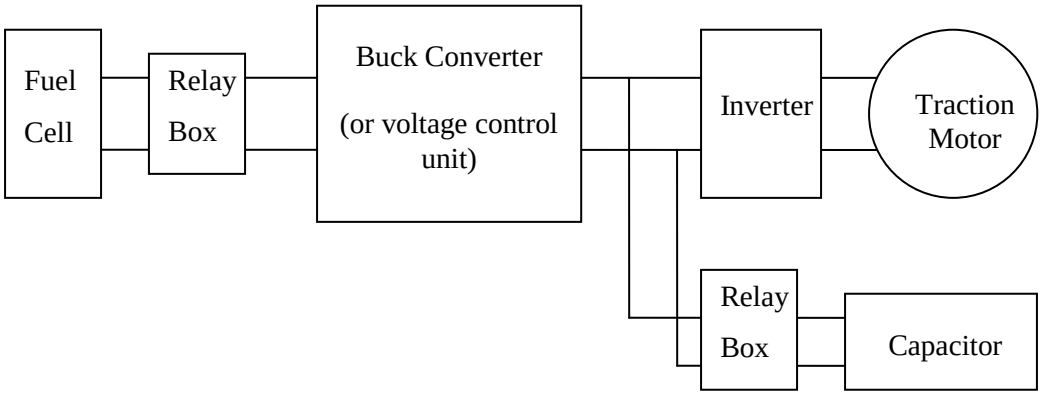

Figure 1.2 Topology of the Honda FCX hydrogen fuel cell vehicle presented in [3].

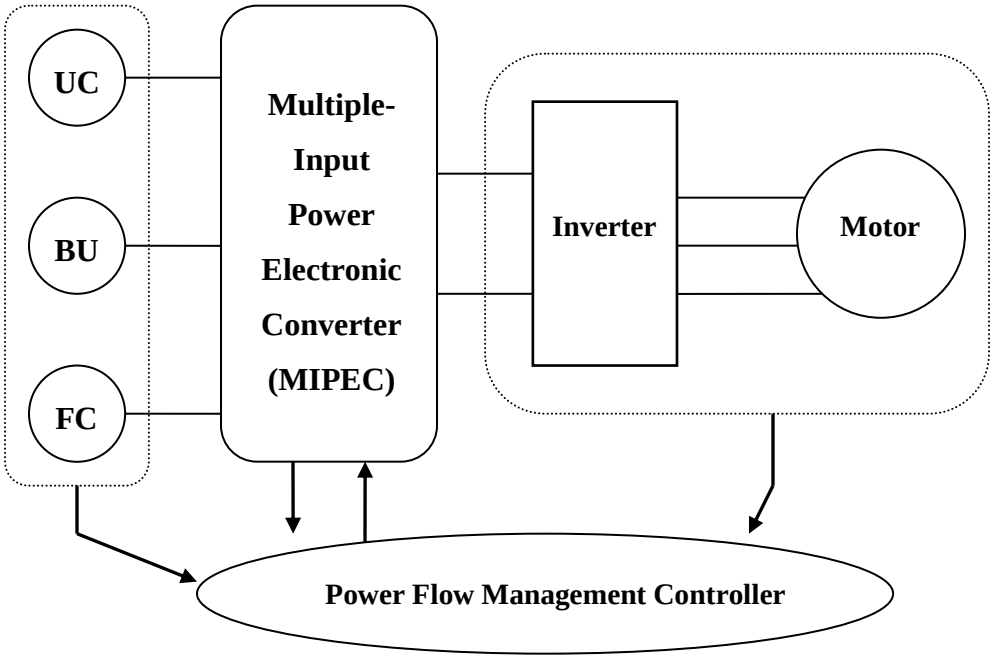

Figure 1.3 Topology based on a Multiple-Input, Single Output converter [4]

During acceleration and braking cycles, the power required to achieve these maneuvers results in power peaks. Neither the fuel cell nor the battery unit is designed to accommodate these large transients, so the designers have enlisted an ultra-capacitor bank to minimize these power swings. The ultra-capacitors are used whenever the sum of the fuel cell and the battery bank is still insufficient to handle the demand of the load. The capacitors are then charged during regenerative braking. The branch that is connected to the fuel cell is not bi-directional so as not to damage the fuel cell. This topology is a great solution to some of the problems discussed with the earlier designs. However, having a converter on each power source is unnecessary. The third source, either the batteries or the ultra-capacitors, can be connected to the high-voltage bus directly, to balance out the small differences in power provided versus power supplied. By keeping the voltage of the high-voltage DC bus constant, only the current will change. The source on the high-voltage DC bus can balance the powers automatically according to KCL. Eliminating a converter, as well as incorporating a different type of battery, will make the design more robust and economical [4].

The suggestion described above to simplify the topology is incorporated into the power management system discussed in [5]. The goal of [5] is to combine a fuel cell with a photovoltaic (PV) array to create a reliable power source. As shown in Figure 1.4, this system still uses a battery for the fuel cell due to its slow response time; however, the usage of a Lithium Ion battery is a great improvement over the previous designs. They are much lighter and can charge and discharge more quickly than lead-acid batteries. Also, the battery is connected directly to the high-voltage DC bus while the PV array, the fuel cell, and the load(s) are all connected using a converter. Each component in this system is used in the following ways: the PV array provides as much of the average power demanded by the load as possible, the fuel cell makes up for the part of power that the PV array cannot provide, and the battery provides or absorbs any transient power during load changes. The boost converter, which the fuel cell uses to connect to the DC bus, helps regulate the bus voltage as well as limit the output current so as not to damage the battery or the fuel cell. The PV array uses a buck converter that helps it track the maximum power point (MPPT).

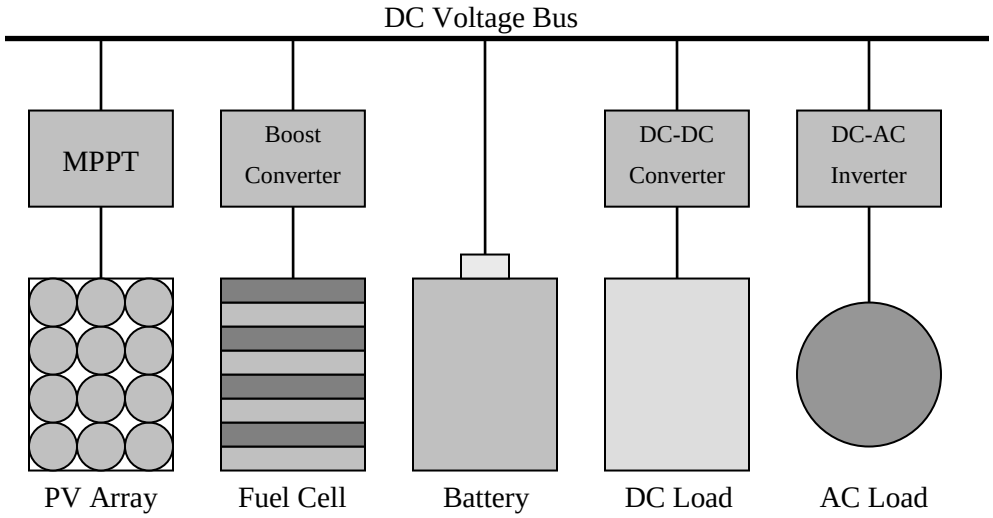

Figure 1.4 Topology for power management of a PV-Fuel Cell power system [5].

This system is the best design discussed thus far. Even though it is very unlikely that a PV array can be used to design consumer vehicles, the overall concept of the system can be used to build a power management system to demonstrate electrically, a vehicular drive train powered by a fuel cell with regenerative braking capability. By removing the PV array and the AC load, we are left with the fuel cell, the battery, and the DC load, in which case only one converter is needed between the fuel cell and the load. This design will be discussed in further detail in the next section.

1.2 Concept of Test Station

The goal of this work is to design a test station that simulates a fuel cell powered vehicular drive-train. The idea for the topology of this station was introduced in the previous section. The setup is shown in Figure 1.5.

The fuel cell is connected to the high-voltage DC bus through a DC-DC boost converter to increase the output voltage of the fuel cell and to control the power drawn from the fuel cell. Since fuel cells can be expensive to run and have a relatively short life span, a fuel cell emulator (FCE) is designed using a power converter. This FCE behaves like the fuel cell, providing the same amount

of voltage and current, at the same operating point, as dictated by the polarization curve of the fuel cell. This will be discussed in more detail in chapter 2.

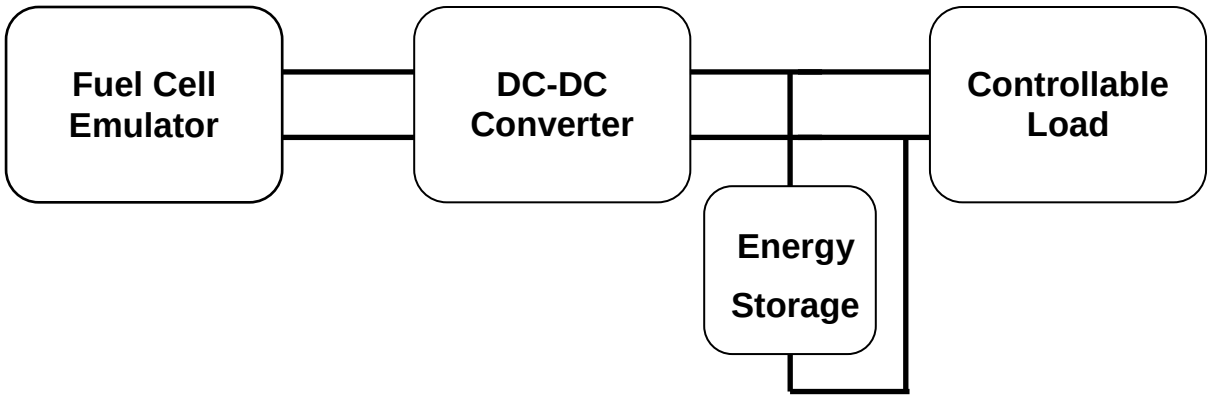

Figure 1.5 Block diagram of test station setup

A boost converter was selected as a DC-DC converter for the reasons described in the previous section. The boost converter steps up the fuel cell voltage, thus reducing the level of the current required by the load. As a result, a smaller fuel cell with a lower output voltage can be used. In this setup, the boost converter controls the output current of the FCE. It also controls the rate of change of the FCE output current from one operating point to another in response to the changes in the load, simulating the slow response time of the fuel cell.

Energy storage is connected to the high-voltage DC bus in parallel with the load. The power that is provided or absorbed by the energy storage is governed by conservation of power and by KCL. For this study, a bank of batteries was considered for energy storage. The design and simulations were based on Lithium Ion batteries due to their faster charge and discharge. The Lithium Ion batteries are also a good choice for experimental work due to their lighter weight. Several batteries were connected in series to achieve the required voltage level of the high-voltage DC bus. The possibility of using capacitors either in place of or in conjunction with the batteries for storage will be considered for future work.

A controllable DC load has been designed to simulate a vehicular load with regenerative braking capability. It utilizes a bi-directional DC-DC converter and a battery in parallel with a load resistor to achieve regenerative braking capability. When the controllable DC load is operating normally, either the battery is charging or the load resistor is connected to absorb power when the battery is fully charged. During regenerative braking, the resistor is disconnected, allowing the battery to discharge to the high-voltage DC bus. The control circuit is designed such that any given drive cycle can be programmed into the controller and the required power versus time is calculated accordingly. The power reference is then manipulated to obtain the current reference signal to control the current. Since the converter is bi-directional, the current is also bi-directional, resulting in a current reference signal that can assume positive or negative values. The sign of the power reference determines the mode of operation of the load. This will be explained in more detail in chapter 3.

1.3 Scope of Work

The scope of this thesis is limited to the design simulation of a test bench for the drive-train of a fuel cell-powered vehicle equipped with regenerative braking capability. In the process, a fuel cell emulator (FCE) and a controllable DC load are designed and tested. It is the intention of this thesis to verify the capability of each building block as well as the complete test bench through simulation All models used in simulations were based on actual components. Testing this station experimentally is saved for future work.

1.4 Organization

This thesis is organized into five chapters. Chapter 1 is the introduction to this research reported in the thesis. The FCE is explained in chapter 2 accompanied by a literature review on fuel cells, including history, types, function, and vehicular applications. The FCE topology is proposed and conditioning of the input and the output power of the FCE is discussed. Lastly, simulation results of the design as well as comparisons to the fuel cell that was emulated are presented.

The bi-directional controllable DC load is explained in chapter 3. It begins with a literature review performed to select the best bi-directional converter for the application. The topology and control are explained and results of simulations are shown.

The fourth chapter combines the fuel cell emulator and controllable DC load and demonstrates the entire test bench setup as shown in Figure 1.5. The design and functionality are discussed and simulation results are given. Finally, conclusions of the research and suggested items for future work appear in chapter 5.

Chapter 2

Fuel Cell Emulator

2.1 Literature Review

Before the Fuel Cell Emulator (FCE) can be considered, first an understanding of the different types of fuel cells, their applications and importance, and fuel cell operation must be discussed.

2.1.1 Fuel Cell

Gregor Hoogers describes fuel cells as "an electrochemical device that continuously converts chemical energy into electrical energy (and some heat) for as long as fuel and oxidant are supplied" [6]. There are many different types of fuel cells, each using a different fuel and electrolyte; however, the principle of operation is essentially the same in all types. Fuel cells can be broken up into two categories: high-temperature fuel cells and low-temperature fuel cells. High-temperature fuel cells operate between 650°C and 1000°C, and are mainly used for large-scale power generation. Low-temperature fuel cells operate between 60°C and 200°C, making them much more attractive for low-power, portable, and vehicular applications. There are three types of low-temperature fuel cells, phosphoric-acid fuel cells (PAFC), alkaline fuel cells (AFC) and polymer electrolyte membrane fuel cells (PEMFC) [6], [7].

PAFCs have the highest operating temperature of all the low-temperature fuel cells, at 200°C. Its electrolyte is molten H_3PO_4 and is mainly used for medium-scale power generation [6].

AFCs are the oldest fuel cells in use. NASA used them on board the Gemini and Apollo spacecrafts. The operating temperature is in the range 60-120°C. The electrolyte utilized by these modules can be either KOH or NaOH. These electrolytes cannot tolerate CO_2 in the system or the electrolyte would absorb it and reduce its conductivity. As a result, NASA had to scrub the fuel free

of CO_2. The fuel used was H_2, which was an impure reformate, and air was used as the oxidant. This drawback has prevented the AFC from being more widely used [6].

Finally, the PEMFC, which has the lowest operating temperature of any of the low-temperature fuel cells, operates in the range 50-100°C. In the 1960s, PEM fuel cells were known as solid polymer electrolyte (SPE) fuel cells [7]. It was refined by Ballard Power Systems in the 1980s to make fuel cells lighter and more compact. The structure that makes up the PEM fuel cell is based on the membrane electrode assembly (MEA) which is no thicker than a few hundred microns. The anode, cathode, and electrolyte, which is a plastic-like polymer membrane, are all sandwiched together to form the MEA. This compact design has proved to be very unique and so versatile that this is the only type of fuel cell currently being considered for vehicular applications [6].

What makes fuel cells so important to us today? Frano Barbir states that "a fuel cell is an electrochemical energy converter that converts the chemical energy of fuel directly into DC electricity [7]." The key word in this phrase is "directly". Conventionally, the energy conversion process usually occurs over several steps:

- First the fuel is burned which converts the chemical energy stored in the fuel into thermal energy or heat.
- Then the heat is transferred to water, which creates steam, with high thermal energy content.
- The thermal energy is then converted to mechanical energy by using the steam to rotate a turbine.
- Lastly, the mechanical energy is converted to electrical energy by using the turbine to run the generator.

Through each of these steps, energy can be lost along the way. Converting chemical energy to electrical energy in one step can make this process much cheaper and more efficient. However, this has not been realized yet and must wait for further advancements in fuel cell technology [7].

Fuel cells have been around for nearly two centuries, since Sir William Grove first invented the concept in 1839. It did not become useful until Francis T. Bacon made the first practical fuel cell in 1937. By the 1950s and 1960s fuel cell technology made its way into space travel applications. However, this technology is still considered relatively new. New advances in fuel cell assembly, materials, and fuel reformation continue to occur, giving fuel cell technology great potential to one day outperform conventional energy conversion methods and energy sources used today. Fuel cells have become very important recently because they have the potential to offer [7]:

- Better efficiency,
- Low to zero emissions,
- Lower cost,
- Longer life due to no moving parts,
- Less noise pollution,
- Higher versatility due to its ability to achieve any power level through a modular, compact design, and lower weight, and
- Reducing North America's dependence on foreign oil when hydrogen fuel is made from renewable sources.

Because of these potential promises, fuel cells can have a wide range of applications, mostly in transportation. Fuel cells can be used in automobiles, motor bikes, scooters, golf carts, farming and construction equipment, space travel, trains, boats, and airplanes. Aside from transportation, fuel cells can also be used for back up power, portable power, and distributed power generation. The wide range of applications shows the versatility and usefulness of a new and upcoming power source that is bound to be the wave of the future [7].

Presently, the main application that public demand and researchers are most concerned with is vehicular propulsion; however, this is not a recent interest. This is a concept that goes back to at least the early 1960s. In 1964, GM began researching possibilities for electric vehicles. The fuel cell

was the main power source under consideration, in which it presented two important advantages over using batteries. It was not restricted to a small distance range, like batteries, and its efficiency was not dependent on operating temperature which allowed for better fuel economy. By 1966, GM invented the Electrovan, the world's first fuel cell vehicle. It used alkaline fuel cells with liquid hydrogen and oxygen as its fuel and oxidizer. It had a driving range of 150 miles (240km) and could travel at a maximum speed of 70 mph (110km/h) [6].

By 1991, GM was funded by the US Department of Energy to produce a methanol-powered electric vehicle. The plan was to use a reformer to extract hydrogen from the methanol fuel and feed it to the fuel cell. In 1998, GM delivered the Opel Zafira. The fuel cell could provide 50kW of power and included battery storage to supply and absorb power during transients and regenerative braking, respectively. The vehicle was able to travel 300 miles (483 km) with a maximum speed of 75mph (120km/h) [6].

Soon after the Opel Zafira was delivered, GM moved away from methanol reformer technology and continued with the belief that "hydrogen will be the long-term choice of fuel for transportation and that the hydrogen should come from renewable sources" [6]. GM then developed three fuel cell vehicles. The HydroGen1 in 2000, was based on the Opel Zafira but used liquid hydrogen as its fuel instead of methanol. The fuel cell power was increased to 75kW, providing a top speed of 90 mph (140km/h) but reducing the driving range to 250 miles (400km) per tank. The HydroGen3 was also based on the Opel Zafira and was introduced the following year, with a fuel cell that could provide power in the range 94-129kW. It had a top speed of 94 mph (150 km/h) and still had a driving range of 250 miles (400km) [6].

The third vehicle that GM introduced was the Chevrolet S-10 gasoline-powered fuel cell vehicle in August 2001. Using a Chevy S-10 pickup truck, the vehicle has been fitted with an on-board gasoline reformer to extract hydrogen from the fuel and feed it directly to the fuel cell stack. A disadvantage of this design is that the reformer takes up over half of the cargo space in the back of the truck. This truck was intended only to be a demonstration vehicle with a fuel cell only able to produce 25kW which translates to only 33 hp [6]. However, fuel economy is improved by 50% over

the conventional gas powered Chevy S-10, while reducing its emissions by half. GM has introduced this vehicle as a temporary solution since hydrogen is not widely available right now. Fuel cells have undoubtedly great potential in vehicle propulsion; however there is no infrastructure for the hydrogen fuel needed to power the vehicles. This is GM's solution to the problem now. This is meant as a stepping stone until an infrastructure for hydrogen fuel is in place [8]. Since 2001, GM has created a fleet of "green vehicles". Most are simply more fuel efficient than their competitors, while some can run on alternative fuels. Others are revolutionary, including an electric car that can recharge from a standard wall outlet. Their fleet includes several hybrid cars as well as a fuel cell powered Chevy Equinox that runs with zero emissions [9].

Other auto manufacturers have engaged in similar research and developed their own versions of fuel cell vehicles (FCV) or fuel cell hybrid vehicles (FCHV). Since 1996, Toyota has built several different incarnations of their FCHV using the RAV-4 and the Highlander starting with methanol reformer technology, moving to direct hydrogen, and then to gasoline reforming technology in 2001, also incorporating regenerative braking technology into some of the vehicle designs. The most popular and currently sold Toyota FCHV is the Toyota Prius. Ford, DaimlerChrysler, Mercedes, Mazda, Nissan, and Honda all took similar steps and made similar vehicles. As fuel cell technology improves, so does the performance of these vehicles. Possibly in the next decade, zero emission fuel cell vehicles will be available at an affordable price to the average consumer [6].

It has been discussed how widely beneficial this new technology is, but how does it work? In a Polymer Electrolyte Membrane (PEM) fuel cell, the membrane is gas tight, but can let protons pass through [7]. There have been many advances in producing polymer electrolyte membranes. A common material used is fluoroethylene. The most widely used is Nafion, developed by Dupont, that has become the "industry standard." The electrolyte must have strong bonds and be resistive to heat, chemical reactions, and water. This very last characteristic makes it easy to expel excess water from the fuel cell to prevent flooding. It also makes this material attractive for other uses such as outdoor attire and footwear. Even though the membrane is water resistant, it is thin enough to diffuse water through it [10].

This membrane is sandwiched between two conductive electrodes. These electrodes are generally made out of carbon fiber, making them porous and able to contain the gaseous fuel and oxidant. At the point where the electrode and membrane meet is a catalyst layer that is particle thin, usually made of platinum, platinum-ruthenium alloy, or lead, although platinum is most commonly used. Platinum is an expensive metal which makes fuel cells expensive as well. Efforts are being made to reduce the thickness of the catalyst layer, decreasing the amount of material used, thus lowering the cost of the fuel cell [6], [7]. These components make up the membrane electrode assembly (MEA). This is shown in Figure 2.1.

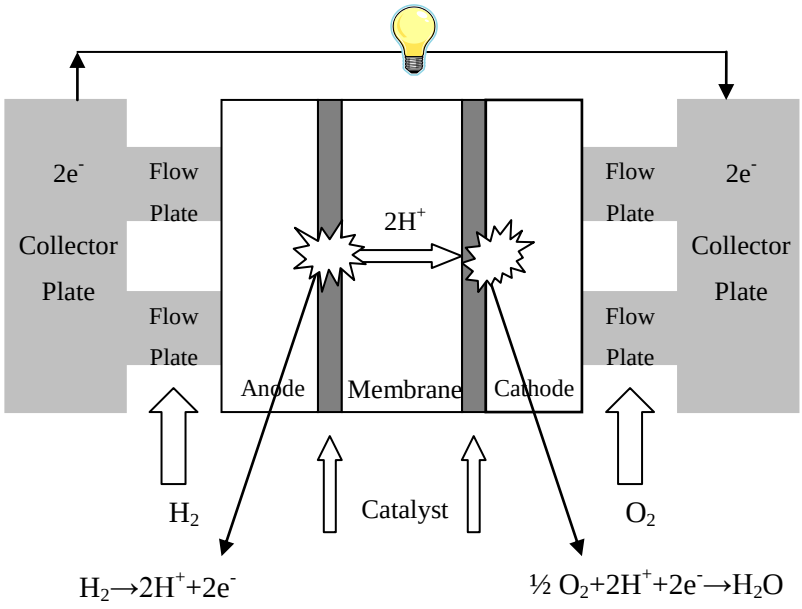

Figure 2.1 Functionality of a PEM fuel cell [7]

The operating process of the fuel cell is simply a series of processes and reactions that all occur simultaneously and interdependently. First, the fuel and reactant gases must flow through the flow plates to reach each electrode. Then the gases must be diffused through the porous material of the electrodes to reach the reaction site at the interface of the electrodes and membrane. Once there are enough reactants, the reactions shown in Figure 2.1 occur. During the reaction at the anode, the hydrogen, made up of a single proton and electron, splits. The electrons are collected by the

electrode, then transferred to the collector plates, and finally are transmitted to the external circuit, thus creating a DC current. The protons are swept through the membrane using a process called electro-osmotic drag. Electro-osmotic drag through porous membranes is highly dependent on the level of hydration. Therefore, water, in the form of vapor, must be present with the reactants to prevent evaporation and dehydration [6]. Once the electrons and the protons reach the cathode, they react with the oxygen and produce water. The presence of water also keeps the operating temperature of the MEA from rising above safe limits [7]. However, it is important that the level of water in the MEA not be too high; otherwise the water will flood the electrodes and block the pores needed to transfer the reactant gases and the products of the reactions [10]. Therefore, excess water must be expelled from the MEA. Excess gas that is too saturated must also be collected and expelled.

All of these processes are very dependent on one another. Each process takes a specific amount of time, making the start up time of a fuel cell relatively long. For each operating point, a special balance of reactants must be maintained and time must be allowed to change the levels of gases making the transient time relatively long as well. The overcoming of these short falls will be discussed in chapter 4.

2.1.2 Fuel Cell Emulator

It has been shown that fuel cells have a great potential for vehicular applications; however using them in the design process of a new system can be quite costly. Reasons for needing a simulated fuel cell include:

- Fuel cells are currently expensive
- Concerns exist about performance including:
    - Response to abrupt changes in load
    - Response to no-linear loads
    - Max power and current abilities

- Concerns exist about safety, cost, and storage of hydrogen fuel.

Some researchers have come up with ways of simulating a fuel cell to determine the type, size, and practicality of a fuel cell for a particular application. This has been demonstrated in [11]. Advantages to having a fuel cell simulator are:

- Cost of development is reduced
- Safety, cost, and storage of hydrogen are no longer an issue, saving both time and money
- Easy adjustment of simulator to model a wide range of fuel cells and power requirements
- Determination of actual fuel supply, preventing over spending and reducing costs
- Simulation of actual conditions for the system being tested.

Most attempts to simulate the fuel cell have been to create mathematical models or use lookup tables as in [12] and [13], to represent the fuel cell. In [11], a computerized fuel cell model was established using LabVIEW and was based on a 500W fuel cell stack manufactured by BCS Fuel Cells Inc. It uses an equation to calculate the output of the fuel cell. This is unrealistic as most fuel cell manufacturers provide data in the form of lookup tables or a curve, and not parameters of an equation relating voltage and current. The model has also been designed to provide information about hydrogen consumption, operating temperature, humidity, and efficiency. In the experimental setup, the load current was measured and fed into the computer model where the stack voltage of the fuel cell was determined. This voltage was compared to AC-DC converter output voltage and the error was passed to a PI controller which controlled the AC-DC converter. This setup is shown in Figure 2.2.

The design proposed in [11] is mainly used for large scale power generation applications. It utilizes an SCR converter to convert from AC to DC power. One of the challenges with using this converter is that it introduces low order harmonics. To attenuate these harmonics a large L-C filter must be used to obtain a very small corner frequency. [11] uses L = 17.5mH and C = 820μF to obtain a corner frequency of 42Hz. Using such a large inductor is expensive and takes up a lot of space. The

same problem exists for filtering of the lower-order current harmonics on the AC-side of the AC-DC converter. Another challenge is that the SCR converter operates at a much lower speed than a switch mode converter and may not be able to realize the V-I characteristics of all fuel cells. Furthermore, the large low-pass filter on the DC-side of the AC-DC converter will limit the system's bandwidth and its capability for high speed operation.

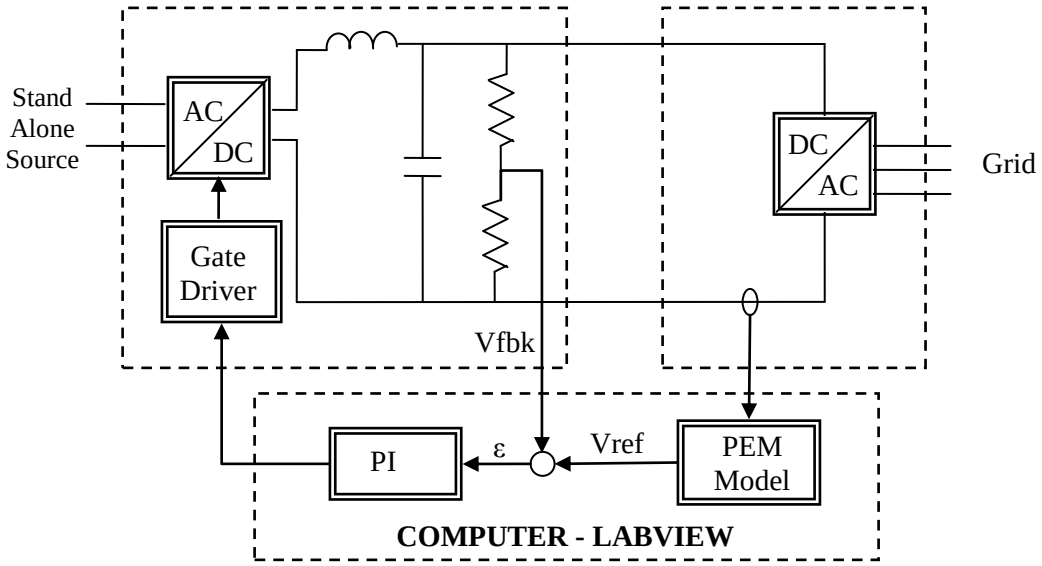

Figure 2.2 Fuel Cell Simulation design shown in [11]

By using a switch mode converter to convert from AC to DC and control the voltage that reaches the load, the response time would be faster, improving the performance of the simulator. A simulator utilizing a switch mode converter could simulate a wider range of fuel cells than the one presented in [11]. This is due to the fact that the speed of operation can be easily adjustable based on the transient characteristic of the fuel cell stack being simulated. Such a design is proposed in the following section. It can be divided into three parts: the buck converter, conditioning of input power, and conditioning of output power.

2.2 Proposed Fuel Cell Emulator (FCE)

2.2.1 Buck Converter

The main part of the FCE is the buck converter. This converter is a simple topology that produces a lower average output voltage than its DC input voltage. Any output voltage between zero and V_{in} can be obtained by varying the duty cycle of the switch. The converter assumes two topological modes depending on the position of the switch as shown in Figure 2.3 [14]. When the switch is closed, the diode is reverse-biased and represents an open circuit; therefore, the input current charges the inductor. The voltage across the inductor is the difference of the input voltage and the output voltage. When the switch is opened, the inductor resists the interruption of current by producing a voltage that forward biases the diode. The inductor current, i_L, remains continuous and circulates through the diode. For the inductor to maintain the current, it must discharge. In this state, the voltage across the inductor is the difference between zero and the output voltage, making it negative. Because of the steady-state inductor principle, the average voltage across the inductor must be zero. Therefore, the output voltage is governed by the following equation:

$$V_{out} = V_{in} d \tag{2-1}$$

where d is the switch duty cycle.

Due to the fluctuations in the output voltage caused by switching, a low-pass filter is required to obtain the average output voltage. To reduce these fluctuations and any harmonics, also caused by switching, the corner frequency of the low-pass filter must be at least one decade below the switching frequency [14]. This is discussed below in more detail.

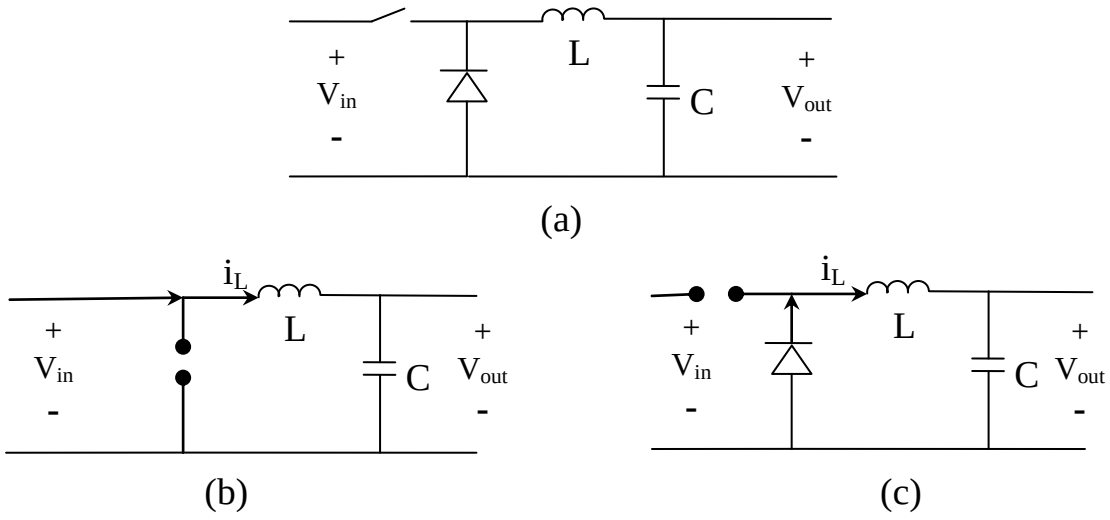

Figure 2.3 Operation of a buck converter (a) Basic buck converter topology (b) Topological mode 1: switch closed (c) Topological mode 2: switch open

When choosing the values for the low-pass filter of the FCE, three important design specifications had to be met. First, the ripple current had to be no more than 5% at a mid-range operating point. The operating point chosen is 680W on the polarization curve of the Nexa Fuel Cell (see Figure 2.6). The inductance can be calculated using the equation below [14].

$$L = \frac{V_{out}(1-d)}{I_{rip} I_{av} f} \tag{2-2}$$

By choosing V_{in} = 170 V, V_{out} = 34 V, f = 20kHz, I_{ripple} = 5% and I_{out} = 20A, the duty cycle can be calculated using (2-1) to be 0.2 and the inductance can be calculated using (2-2) to be 1mH. Since the ripple current is chosen to be 5%, this inductance ensures that the ripple will be at 5% to meet our first design specification.

Second, the ripple voltage at maximum output power had to be no more than 5%. The capacitance can be calculated using the equation below [14]:

$$\Delta V = \frac{I_{out}}{4Cf} \rightarrow C = \frac{I_{out}}{4\Delta V f} \tag{2-3}$$

By choosing I_{out} = 45A, f = 20kHz and $\Delta V \approx 4\%$ the capacitance can be calculated to be 500μH using (2-3). Since the ripple voltage was chosen to be less than 5%, this capacitance ensures that the ripple will be less than 5% to meet our second design specification.

Third, the corner frequency had to be at least one decade below the switching frequency, as stated above. We can double check that this is satisfied by using equation (2-4) [14].

$$f_c = \frac{1}{2\pi\sqrt{LC}} = \frac{1}{2\pi\sqrt{1mH \times 500\mu F}} = 225.07Hz \tag{2-4}$$

Since the switching frequency is 20 kHz, 225 Hz is well below one decade, so this design requirement has been met.

The design of the FCE is very closely related to a basic buck converter as described above. The input of the converter is assumed to be around 170 V DC, which is the DC output voltage of a single-phase diode bridge rectifier, fed from a 120-VAC supply with an output capacitor filter. This will be discussed in further detail in the next section. The output of the converter was designed to be the actual voltage and current output of the Nexa Fuel Cell module from Ballard Power Systems (Appendix A). The output characteristic, as well as the control, will be discussed later in this section. The high-level design of the FCE is shown in Figure 2.4.

The control scheme is a major part of the FCE. It is responsible for the output matching the Nexa Fuel Cell polarization curve. As mentioned in section 2.1, mathematical models have been used to simulate a fuel cell. One such model, explained in [15], was used as a starting point for the control scheme. The equation used is shown below.

$$V = N\left[E - \blacklozenge + i_n \widetilde{r} - A\ln\left(\frac{i+i_n}{i_0}\right) + B\ln\left(l - \frac{i+i_n}{i_l}\right)\right] \tag{2-5}$$

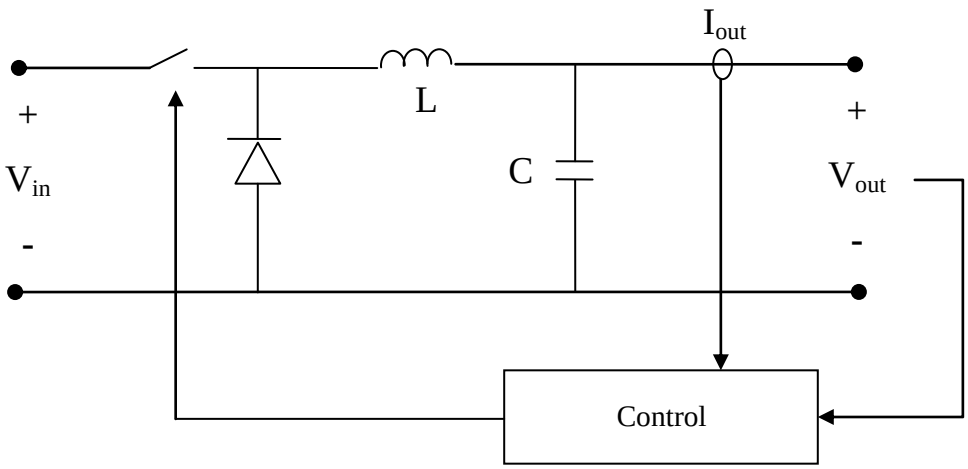

Figure 2.4 Design of the Fuel Cell Emulator based on a buck converter

According to [15], N is the number of fuel cells in the stack, E is the open circuit voltage of each individual cell, i is the current density, i_n is the internal current density, r is the area specific resistance of each individual cell, A is the activation voltage loss coefficient, i_0 is the exchange current density at the reaction site, B is the mass transport voltage loss coefficient, and i_l is the limited current density. It is not likely to know the specific coefficients of each fuel cell stack that a manufacturer makes, making the use of this equation unrealistic for a control scheme. However, [15] does provide some typical values for the constants to obtain a polarization curve. The values are: N = 50, E = 1.2 V, i_n = 2 mA/cm^2, r = 30x10^{-6} kΩ.cm^2, A = 0.06 V, i_0 = 0.067 mA/cm^2, B = 0.05 V, and i_l = 900 mA/cm^2. The resulting polarization curve is shown in Figure 2.5.

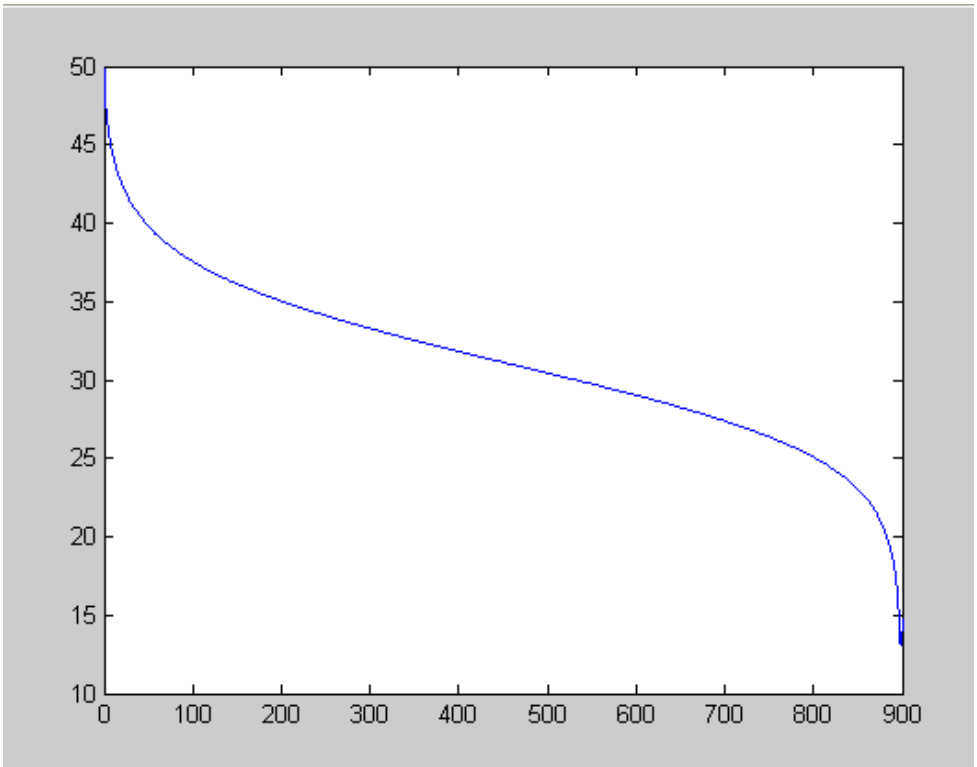

Figure 2.5 Polarization curve using Equation (2-5) and data from [15]

Unfortunately this method cannot be used for the control scheme because the parameters of the Nexa power module are not known. Therefore, our alternative is to use a lookup table. By using the polarization curve provided in the Nexa Fuel Cell manual [16], shown in Figure 2.6, and interpolation, Table 2-1 was obtained.

The control circuit of the buck converter is shown in Figure 2.7. The output current is fed into the control circuit. Table 2-1 is used to interpolate and output the corresponding voltage on the polarization curve to the PI controller as a reference. Also, the actual output voltage is fed into the control circuit as the feedback signal. The PI controller then reduces the error between the reference and the feedback signals and sends a switching signal to the switch to control the output voltage. The results are given in section 2.5.

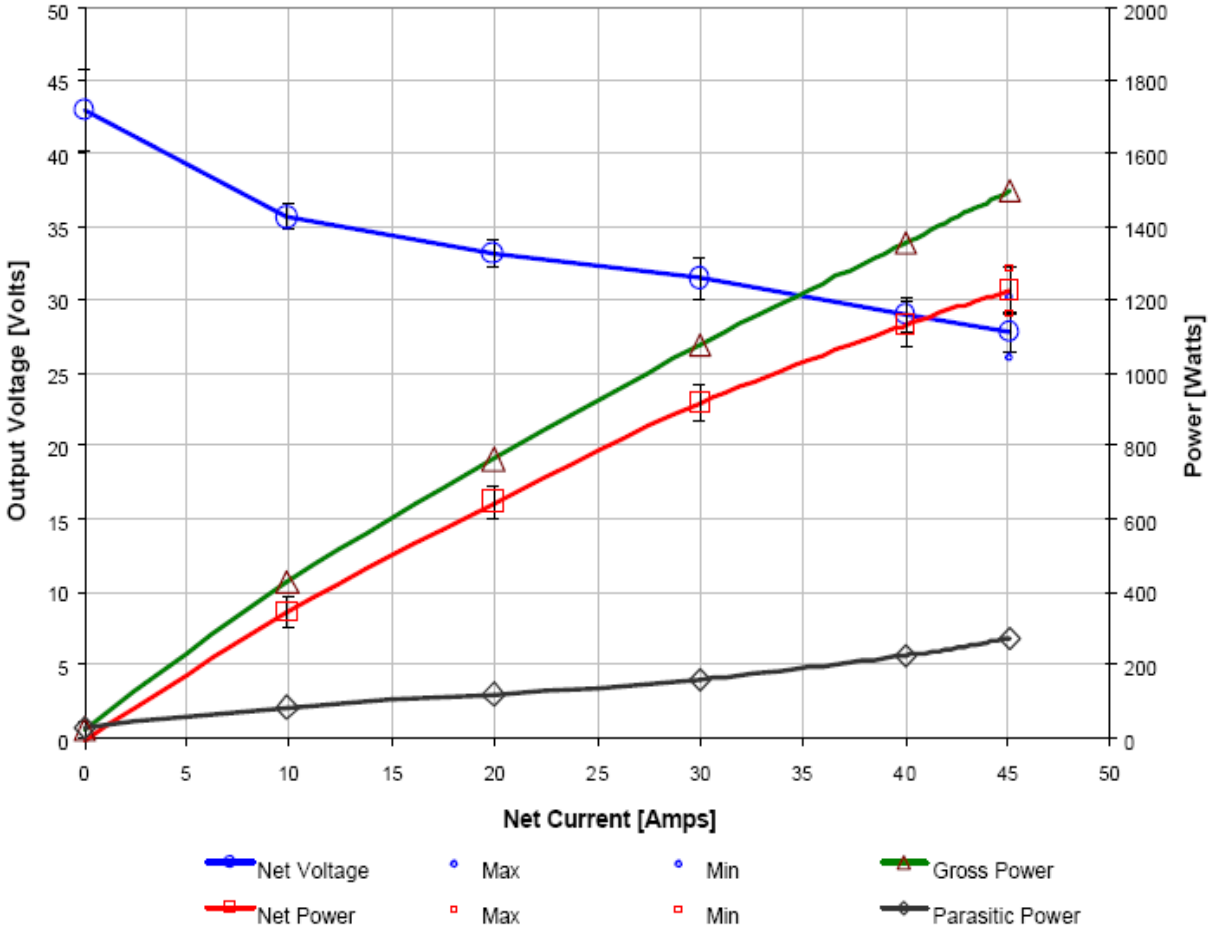

Figure 2.6 Polarization and power curves of the Nexa Fuel Cell module [16]

Table 2-1 Interpolated Table from Polarization Curve

Current (A)	Voltage (V)	Power (W)	Load (Ω)
0	43	0	∞
5	39.5	197.5	7.9
10	36	360	3.6
15	35	525	2.33
20	34	680	1.7
25	33	825	1.32
30	32	960	1.067
35	30.5	1067.5	0.87
40	29	1160	0.725
45	27	1215	0.6

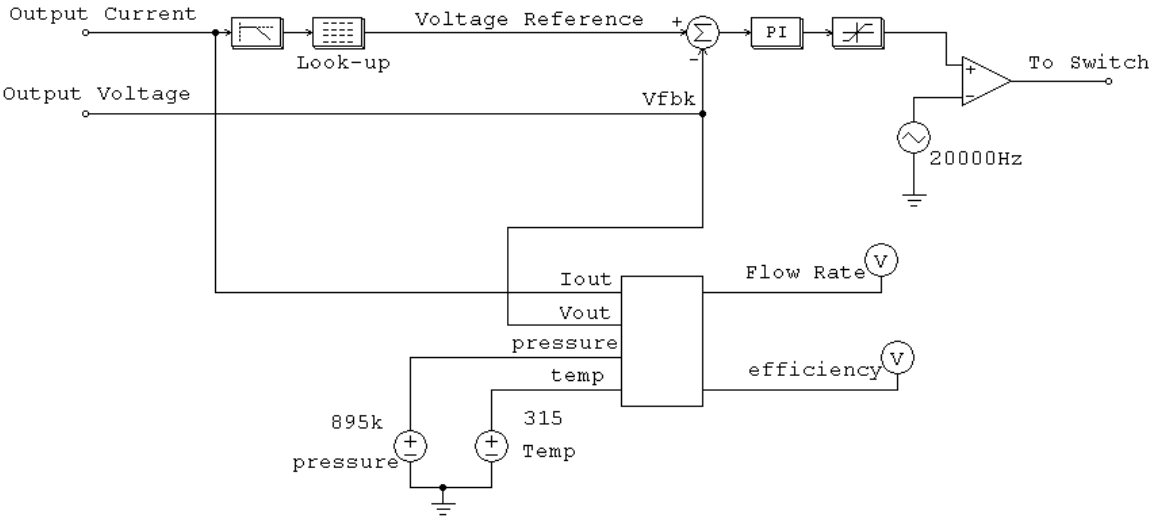

Figure 2.7 FCE control circuit

The other function of the control circuit is calculating the amount of hydrogen that would be used by the fuel cell. In addition, it will also calculate the efficiency of the stack. Inputs to this calculation circuit are the output voltage and current of the FCE. Then two calculations are done simultaneously. First the flow rate is calculated using a lookup table (Table 2-2), estimated from the chart shown in Figure 2.8 [16].

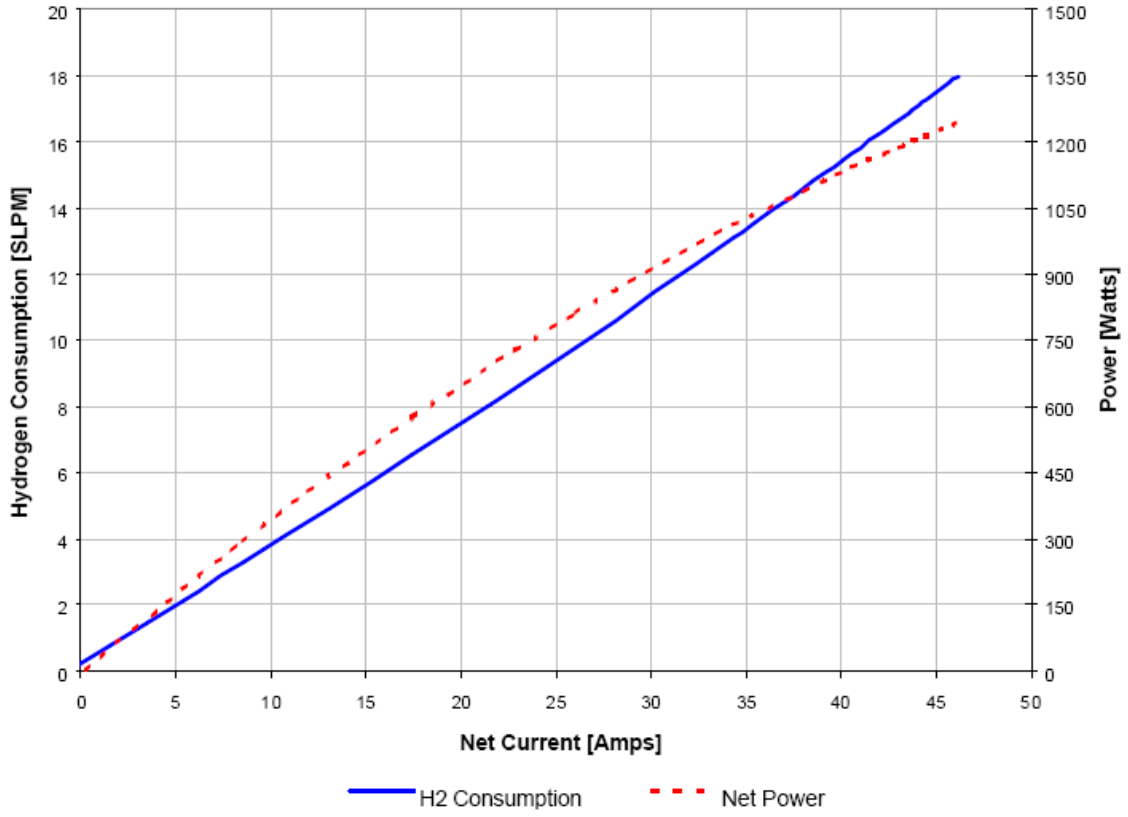

Figure 2.8 Hydrogen consumption rates of the Nexa Fuel Cell module [16]

The ideal gas law [17] was used to calculate the volume per minute that would be consumed given an operating point on the polarization curve, a pressure, and a temperature. According to [16], the Nexa Fuel Cell can operate within the pressure range 70-1720kPa and temperature range 278 – 353K (5-80°C). A mid-range pressure and temperature were chosen for the simulation to be 895kPa and 315K, respectively. The results will be given in section 2.5. An example of the calculation is shown below:

Assume 18 standard liters per minute (SLPM) are consumed at 273K and 1.013x10^5Pa. First, the amount of moles per minute must be found to convert to the new temperature and pressure chosen for the simulation. This calculation is found using:

$$n = \frac{pv}{RT} = \frac{(1.013\times10^5\,Pa)(18\times10^{-3}\,m^3)}{(8.31\,J/mol\cdot K)(273K)} = 0.804\,mol/\min \tag{2-6}$$

Then the new liters per minute can be calculated using:

$$v = \frac{nRT}{p} = \frac{(0.804\,mol/\min)\ (8.31\,J/mol\cdot K)(315K)}{895kPa} = 0.002\,m^3/\min \tag{2-7}$$

A full table and graph are shown in Appendix B.

Table 2-2 Hydrogen Consumption Lookup Table estimated from Figure 2.8 [16]

Current (A)	H_2 Consumption (SLPM)
0	0.25
5	2.0
10	3.99
15	5.95
20	7.9
25	9.85
30	11.8
35	13.75
40	15.70
45	18.0

Efficiency is the other output of this part of the control circuit. The efficiency calculation is done concurrently with the flow rate calculation above. From [16] and [17], it is found that there are

237.42 kJ/mol. Using this constant, we can calculate how much power is contained in the amount of hydrogen being consumed at the given rate above, and compare that to the net output power.

Assume 0.804 mol/min of hydrogen is being consumed by the fuel cell at full load.

$$237.42\,{}^{kJ}\!/_{mol} \times 0.804\,{}^{mol}\!/_{\min} = 190.885\,{}^{kJ}\!/_{\min} = 3181.428\,{}^{J}\!/_{\sec} \tag{2-8}$$

$$\eta\% = \frac{P_{out}}{P_{in}} = \frac{1200W}{3181.428W} = 37.7\% \tag{2-9}$$

According to Figure 2.9, this calculation agrees with the data given in [16].

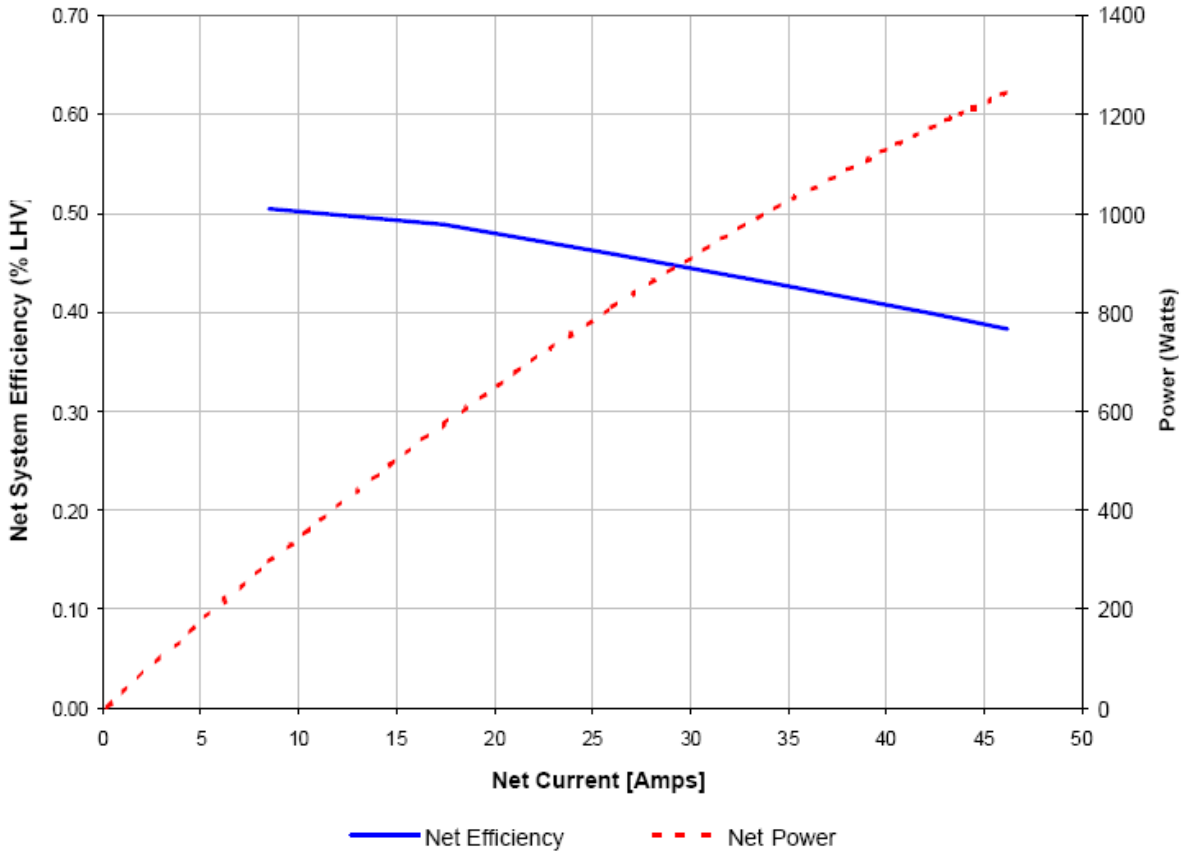

Figure 2.9 Net System efficiency curve of the Nexa Fuel Cell module [16]

2.2.2 Conditioning of Input Power

As mentioned in the previous section, the input voltage of the FCE is 170 V DC. This voltage was chosen based on the selected AC power source. To power the FCE, the notion is to use a standard wall outlet which provides $120V_{rms}$ AC making the peak voltage 170 V. This type of power is available everywhere in North America, allowing the FCE to be extremely flexible and versatile. To convert from $120V_{rms}$ AC into 170V DC, a diode bridge rectifier (DBR) was used.

A DBR is often used for electronic loads such as desktop computers and televisions that use DC rather than AC. The most common type of DBR is a single-phase rectifier shown in Figure 2.10. When V_{ac} is positive, diodes 1 and 2 conduct, while diodes 3 and 4 are reverse-biased and open circuited. When V_{ac} is negative, diodes 3 and 4 conduct while diodes 1 and 2 are reverse-biased and open circuited. The DC output is then a full-wave rectified sinusoid. Most DBRs use a large electrolytic capacitor to smooth the DC voltage waveform. The capacitor will discharge very slowly, depending on the time constant of the capacitor-load combination, when the DBR output voltage is smaller than the capacitor voltage, providing a rather constant voltage to the load. For this reason the capacitor must be relatively large. When the output of the DBR exceeds the voltage of the capacitor, the capacitor charges, drawing current from the DBR for the short charging period. This results in current spikes at the AC side.

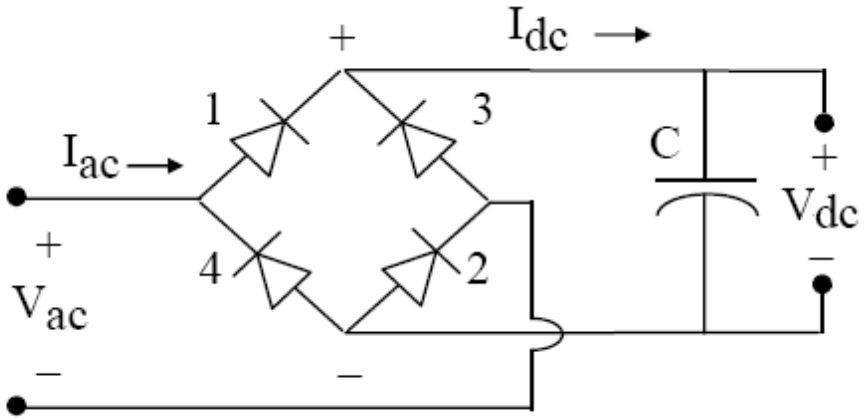

Figure 2.10 Single-Phase Diode Bridge Rectifier [14]

There were several problems that were faced with the conditioning of the input power for the FCE. One was to deal with the large current spikes on the AC side of the DBR. Another was to determine a large enough capacitor to reduce the ripples to 1-2%. If the ripples at full power are to be reduced to 2% of the peak voltage, then V_{ripple} is 3.4V. Therefore, the size of the capacitor was calculated to be [14]:

$$C = \frac{P}{2fV_{peak}V_{ripple}} = \frac{1200}{2 \times 60Hz \times 170V \times 3.4V} = 17.3mF \tag{2-10}$$

This is too large and not practical; plus, it does nothing to solve the problem with the current spikes on the AC side. Therefore, a different approach was needed.

To solve the problems mentioned above, a power factor correction circuit, presented in [18], will address these issues and improve the voltage and current input to the FCE. It can smooth the voltage and prevent the current spikes from ever being produced in the first place by shaping the AC-side current waveform. This design incorporates a DBR at the input and a boost converter as a transitional stage between the DBR and the FCE. Details of a boost converter will be discussed in section 2.2.3. The most important aspect about this circuit is the control scheme which takes care of waveshaping the DBR input current and controlling the FCE input voltage. A 2-loop control scheme is needed, one for the output voltage and one for the input current. The first loop uses the output voltage as a feedback signal and compares it to the desired output voltage; in this case it is 170V. This error is then reduced by the first PI controller. This PI controller must have a slow response so as not to compete with the controller in the current loop. The output of the controller is the scaling factor for the current reference. The output voltage of the DBR is a full-wave rectified sinusoid, as stated before. This is the desired shape of the current on the DC-side of the rectifier, since it results in a sinusoidal current on the AC-side of the DBR. Therefore, a signal derived from the output voltage of the DBR is multiplied by the scaling factor to obtain the reference signal for the current control loop. The output current of the DBR is then compared with the current reference signal and the error is passed to the second PI controller which has a very fast response to waveshape the DBR DC-side current. By using this method, the current spikes on the DBR AC-side have been avoided

and the ripples in the input voltage of the FCE have been reduced. This topology is discussed in [18] and is shown in Figure 2.11.

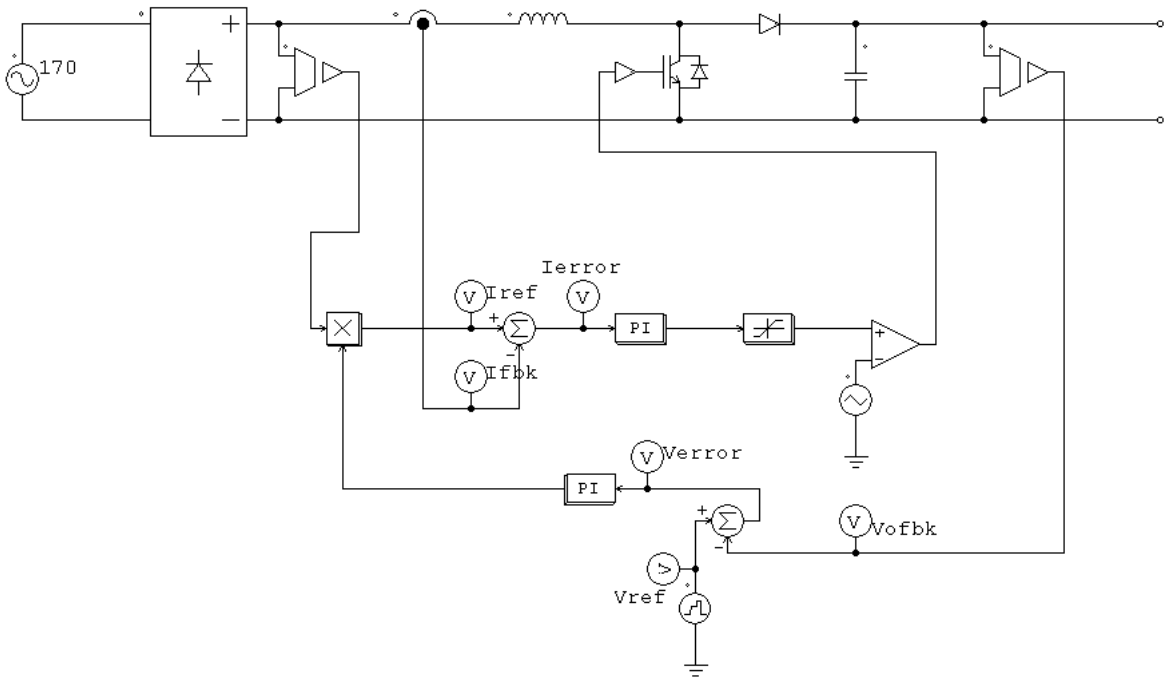

Figure 2.11 Power Factor Correction topology and control scheme [18]

2.2.3 Conditioning of Output Power

The output power, as explained in section 2.2.1, matches the polarization curve of the Nexa Fuel Cell module from Ballard Power Systems, shown previously in Figure 2.6. However, it was mentioned in section 2.1, and in chapter 1, that fuel cells have a time delay when changing operating points on the polarization curve. A load, especially a vehicular load, will request power changes much faster than the fuel cell can provide. This delay has not been incorporated into the FCE. Another aspect to point out is that very few applications require the exact voltage and current given by a fuel cell; usually this power is transformed by stepping the voltage up, and possibly using an inverter, to obtain the form of power that the load can accept.

Voltage step-up can be accomplished by using a basic boost converter between the output of the FCE and the high-voltage DC bus. A boost converter is a simple topology that produces an output DC voltage higher than its input DC voltage. Any output greater than or equal to V_{in} can be

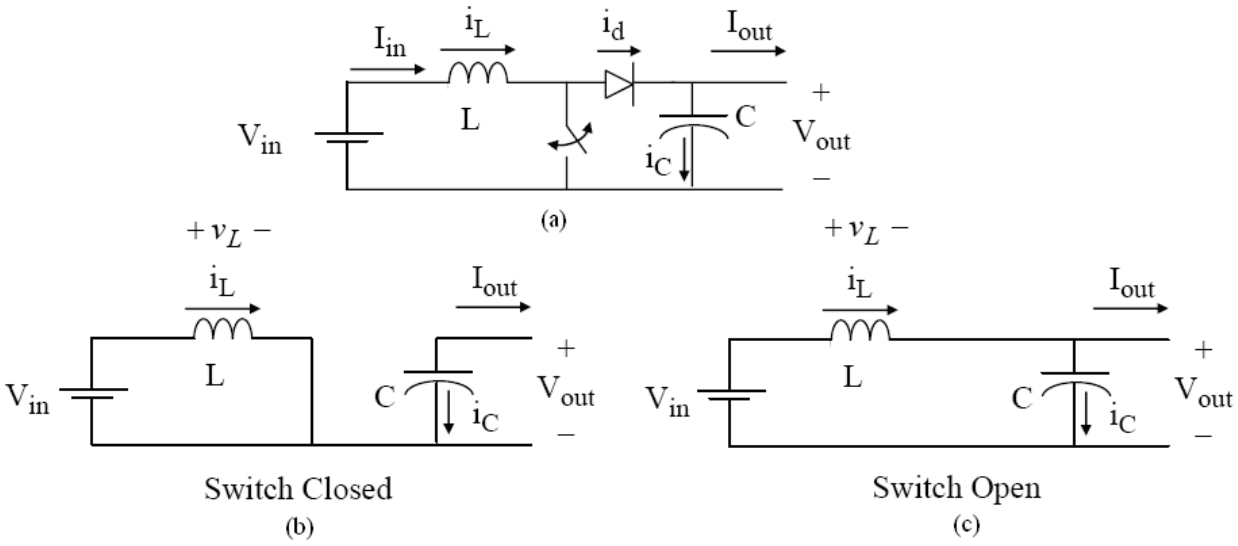

Figure 2.12 Operation of a boost converter (a) Basic boost converter topology (b) Topological mode 1: switch closed (c) Topological mode 2: switch open

obtained by varying the duty cycle of the switch; this results in 2 different topological modes shown in Figure 2.12 [14]. When the switch is closed, the diode is reverse-biased and open circuited; therefore, the input current charges the inductor. The voltage across the inductor is the difference between the input voltage and zero. The output power is being provided by the capacitor which is discharging. When the switch is opened, the diode is forward-biased by the L d/dt voltage generated by the inductor and begins to conduct. For the inductor to maintain the current it must discharge. In this state, the voltage across the inductor is the difference between V_{in} and the output voltage, making it negative. The current not only supplies the load at this point, but also charges the capacitor. Because of the steady-state inductor principle, the average voltage across the inductor must be zero. Therefore, the output voltage is governed by the following equation:

$$V_{out} = \frac{V_{in}}{1-d} \tag{2-11}$$

The boost converter can be used to control the output current, and thus the power output of the FCE. The delay of the Nexa power module can be incorporated by including a delay in the control loop. For this control scheme, the power reference signal of the load is used and the current reference is chosen using Table 2-1 as a lookup table. Then, the change in the reference signal is slowed down by passing it through a rate limiter. According to [16], the delay of the Nexa Fuel Cell module is 0.5 sec from no load to full load; therefore, the rate limiter is set to realize this rate of change. The output of the rate limiter is now the reference signal that is compared with the boost converter's input current. The error is then sent to the PI controller that will output the switching signal to control the switch. If the output of the boost converter is held constant, then as the power changes, only the output current will change based on the present power operating point. Another way to maintain the voltage on the high-voltage DC bus is by connecting the storage battery directly to the bus. However this will be discussed in chapter 4. The design of the boost converter and the corresponding control circuit is shown in Figure 2.13.

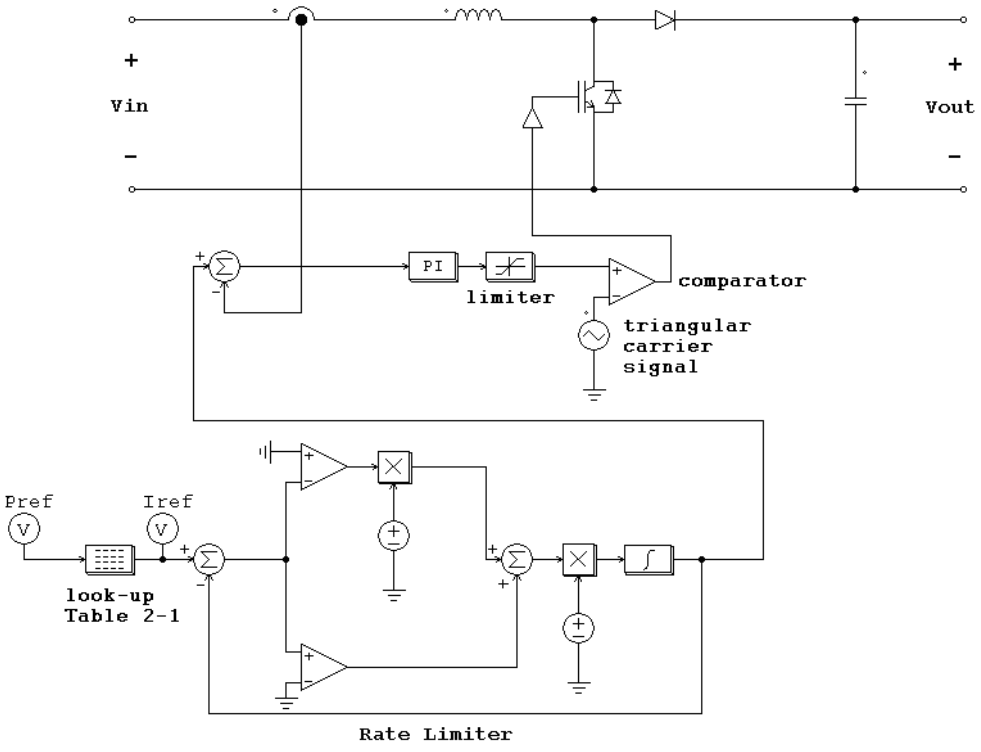

Figure 2.13 Boost Converter with Control and Rate Limiter

2.3 Simulation Results

The FCE, including the input and output power conditioning, were designed and simulated on the computer using PSIM, a power electronic circuit simulation package by PowerSim Inc. The load that was used to obtain the polarization curve of the FCE was a resistor bank. At every specified instant of time, a new resistor is progressively switched in, changing the amount of power that is drawn from the FCE. This continues over the course of the simulation until all the resistors in the resistor bank are switched in. This resistor bank is connected at the output of the boost converter. The resistance values in Table 2-1 were not used. The voltage at the output of the boost converter was kept constant at 100V. Therefore, new resistance values were calculated to obtain the correct power. These values are listed in Table 2-3.

As stated in section 2.2.3, the reference signal of the boost converter input current is chosen based on the power reference signal from the load. This method can only be used in the full test bench set up. Since a resistor load bank is being used to obtain the polarization curve, the reference signal was specified in the same manner as the load bank. At a specified time interval, a series of step voltage sources were used and each increased the power at staggered intervals to match the power requested in Table 2-3. The power signal was then passed through the lookup table to obtain the current reference, as described in section 2.2.3.

To decrease the running time of the simulation, the time interval between successive operating points was chosen to be 100ms, instead of one second, as with a real drive cycle from a vehicle. Therefore, in the simulation, 100ms will represent 1 second of real time.

In Figure 2.14, the simulation results obtained from PSIM are shown. These signals are the output voltage and current of the buck converter. It can be seen that as the current increases, the voltage decreases, just as was shown in Figure 2.6. The signals have a stair-step form because the system is held at each operating point for 100 milliseconds. The ramps reflect the time delay that was introduced into the control circuit of the boost converter; so one time interval (or 100 milliseconds) is

Table 2-3 Equivalent Resistance at Output of the Boost Converter for Polarization Curve Test

Power (W)	Equivalent Resistance (Ω)
0	Open
197.5	50.63
360	27.77
525	19.05
680	14.7
825	12.12
960	10.14
1067.5	9.367
1160	8.62
1215	8.23

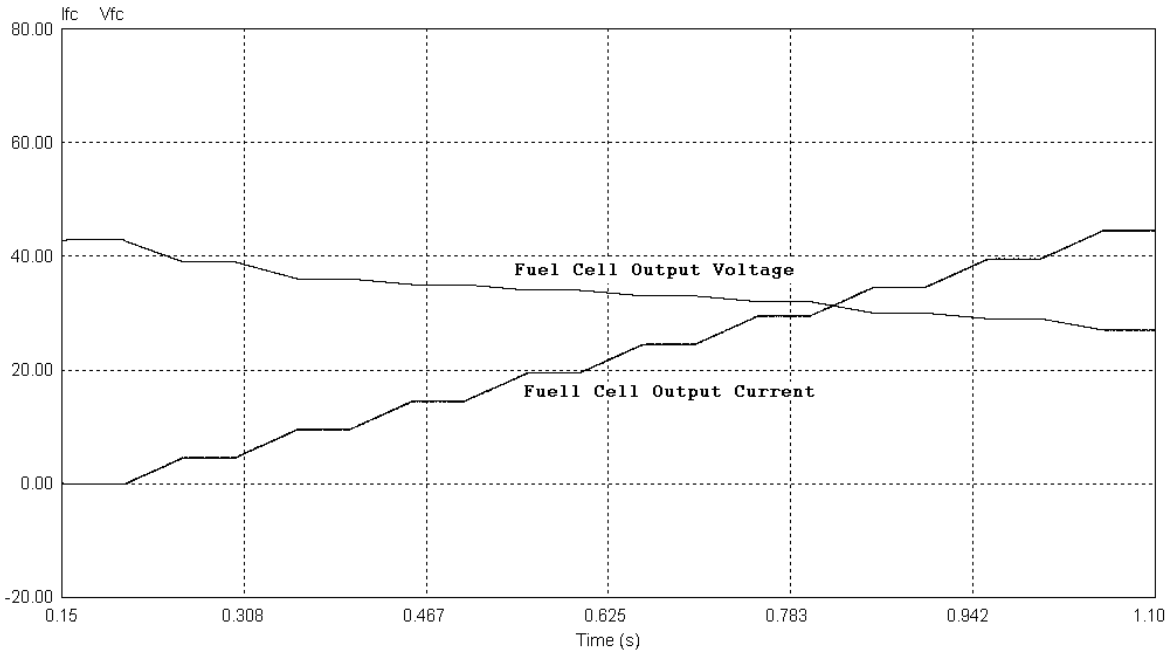

Figure 2.14 Voltage and Current simulation results of FCE for the Polarization Curve

from the beginning of one ramp to the start of the next. The time on the x-axis does not start at zero second. This is due to the system needing time to start up and charge all of the energy storage components. Therefore the polarization test actually started at 0.15 second. It is also shown in Figure 2.14 that the ripple in the voltage and current is negligible, just as the L-C filter in the buck converter had been designed to do.

The output power of the FCE was also obtained through PSIM simulation. This signal is a result of multiplying the voltage and current from Figure 2.14 together to obtain the power output of the FCE. It can be seen, in Figure 2.15, that even the ripple content in the product is negligible.

To show that this is the same as the polarization and power curves of the Nexa Fuel Cell module, the data from the lookup table, obtained from [16] and the data points obtained from the simulation results were charted with Excel. The resulting graph is shown in Figure 2.16. Since the data obtained from [16] was used as the reference for the FCE it was expected that the output of the FCE would closely match the experimental data provided by the Nexa manufacturer.

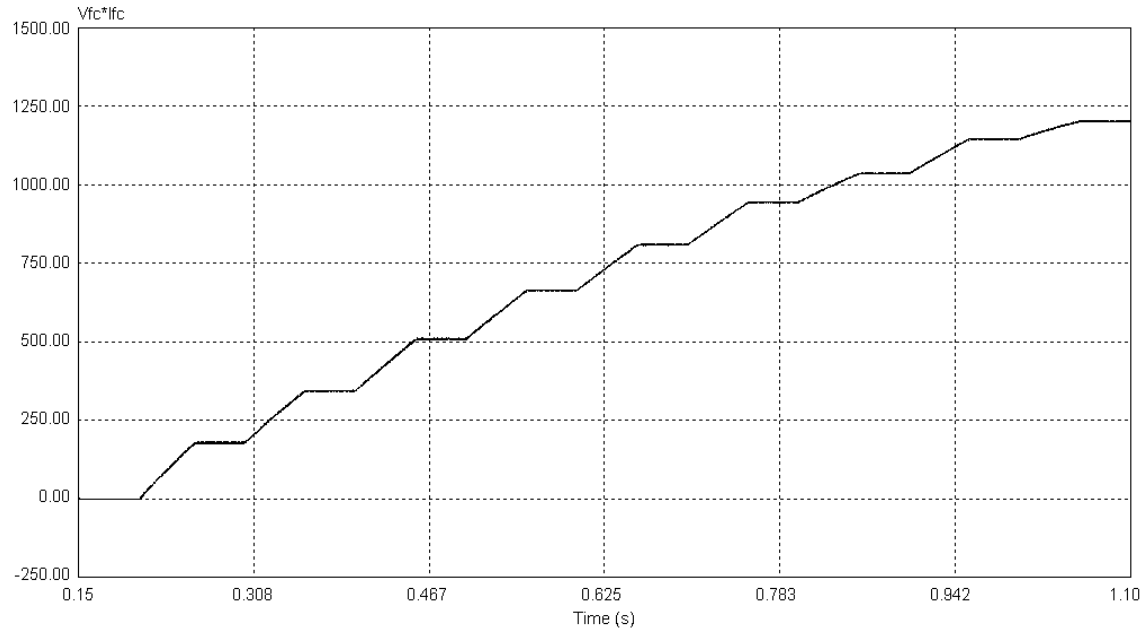

Figure 2.15 Power simulation results of the FCE for the Polarization Curve

As mentioned in section 2.1.2, the control circuit of the buck converter has also been designed to provide the H_2 consumption and efficiency of the Nexa Fuel Cell module to determine how much hydrogen would be needed if the Nexa were to be used for a certain application. Figure 2.17 shows the hydrogen consumption rate results for the FCE. As the power demand increases, so does the hydrogen consumption rate, shown in m^3/min; however, the data is not at standard pressure and temperature. The Nexa Fuel Cell module can operate in the pressure range 70-1720kPa and the temperature range 278 – 353K (5-80°C). A mid-point was chosen for this simulation at a pressure of 895kPa and a temperature of 315K.

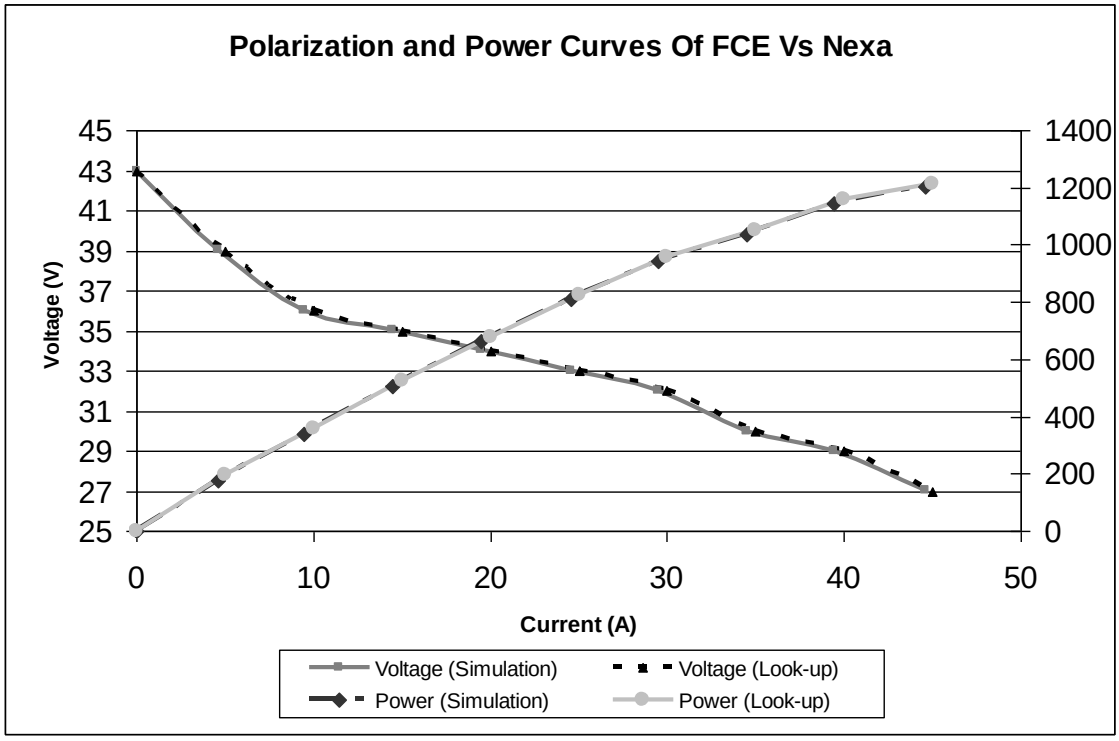

Figure 2.16 Polarization and power curves of FCE compared with Nexa

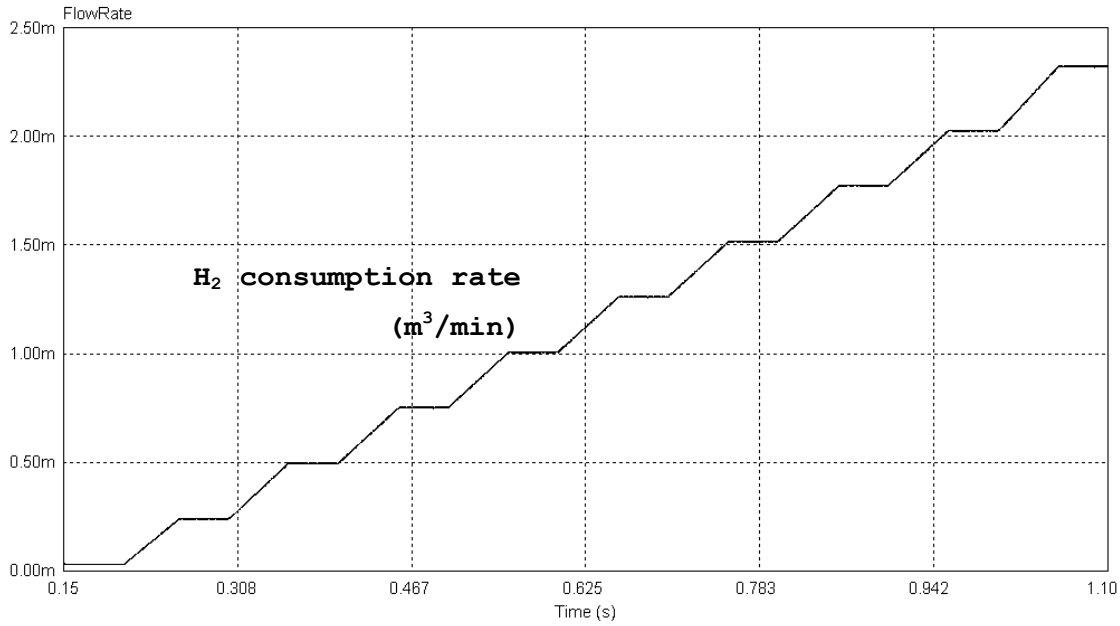

Figure 2.17 Hydrogen Consumption Rate simulation results of the FCE

To compare this with the data obtained from the Nexa Fuel Cell manual, the results in Figure 2.17 will have to be converted to standard liters per minute (SLPM). This was done using Excel. To convert to SLPM, a two-step procedure must be taken. First, the number of moles of gas must be calculated. The number of moles of matter never changes, regardless of pressure and temperature. However, volume does change with these two parameters. Therefore, to determine the volume of hydrogen being consumed at standard temperature and pressure, the moles of gas being consumed at a specified temperature and pressure must be calculated first. Then, the new volume can be determined using the standard temperature and pressure, 101 kPa and 273 K, respectively [17]. Using equation (2-6) and (2-7), Table 2-4 can be obtained.

It is shown in both Table 2-4 and Figure 2.18 that the rate of consumption of hydrogen, calculated by the FCE control circuit, represents the exact amount of hydrogen needed to fuel the Nexa Fuel Cell module under the same conditions. The data in Figure 2.18 is plotted against current to show its similarities to Figure 2.8, where hydrogen consumption was also plotted against current in [16]. By comparing these two figures, it is even more apparent that the results of the FCE represent the Nexa Fuel Cell module.

Table 2-4 Hydrogen consumption conversion from PSIM data into SLPM

Current (A)	H_2 (Simulation)	moles/min	H_2 in m^3/min (Simulation)	H_2 in SLPM (Simulation)	H_2 in SLPM (lookup)
0	3.26E-05	0.011163	0.000251	0.250743	0.25
5	0.00024	0.082085	0.001844	1.843767	2
10	0.000498	0.170222	0.003823	3.823476	3.99
15	0.000755	0.258231	0.0058	5.800312	5.95
20	0.001007	0.344327	0.007734	7.734165	7.9
25	0.001262	0.43147	0.009692	9.691533	9.85
30	0.001515	0.51788	0.011632	11.63247	11.8
35	0.001773	0.6061	0.013614	13.61403	13.75
40	0.002027	0.692996	0.015566	15.56586	15.7
45	0.002321	0.793538	0.017824	17.82421	18

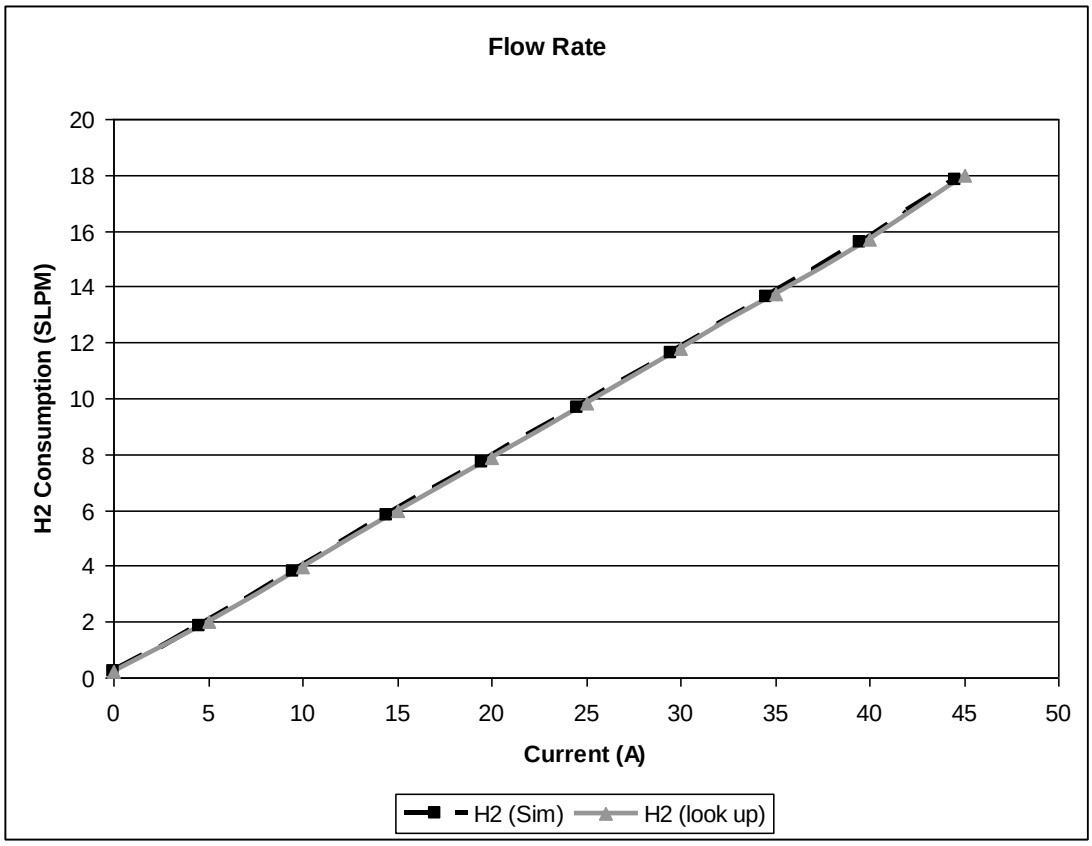

Figure 2.18 Flow Rate results of FCE compared with Nexa, shown in SLPM.

In addition to calculating the flow rate, the efficiency was also determined. The results of the simulation are shown in Figure 2.19. The start time of the graph is 0.35 second because that corresponds roughly to 300W. According to [16], the Nexa Fuel Cell module is operating at its maximum efficiency at this operating point. After that efficiency gradually declines to about 38% at maximum output power. For loads below 300W, efficiency quickly declines to zero as the auxiliary load takes over the hydrogen consumption. To ensure that these results compare with the specifications from Nexa Fuel Cell manual, data points were estimated from Figure 2.9, in the same manner as the lookup tables for the polarization curve and the hydrogen consumption, and charted against the results from PSIM. This comparison is shown in Figure 2.20.

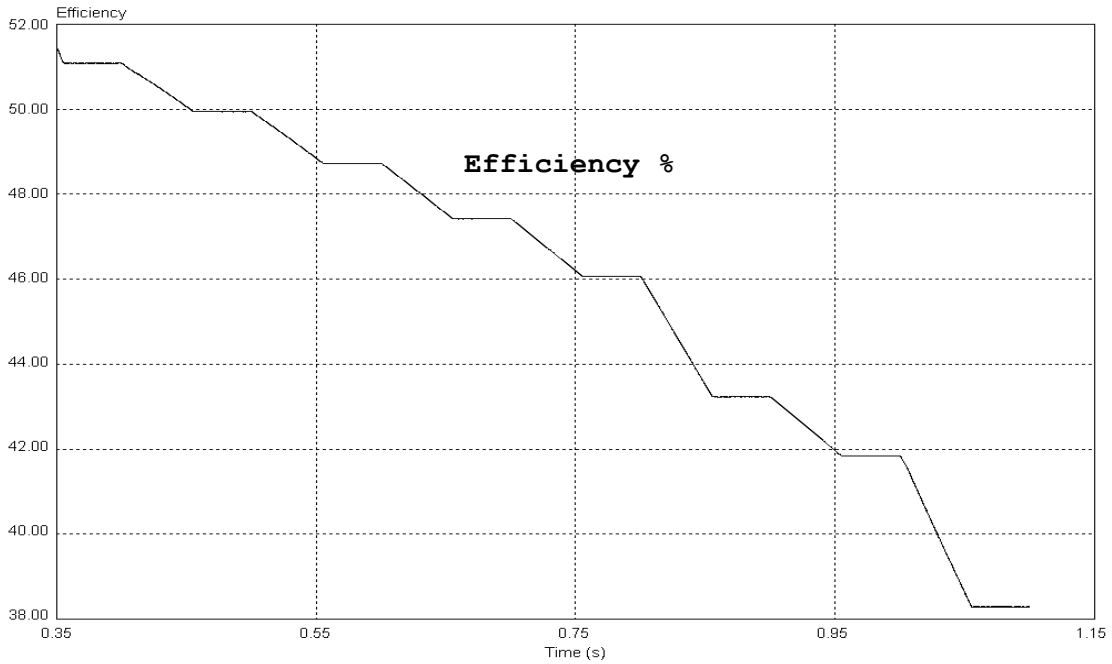

Figure 2.19 Efficiency results of FCE

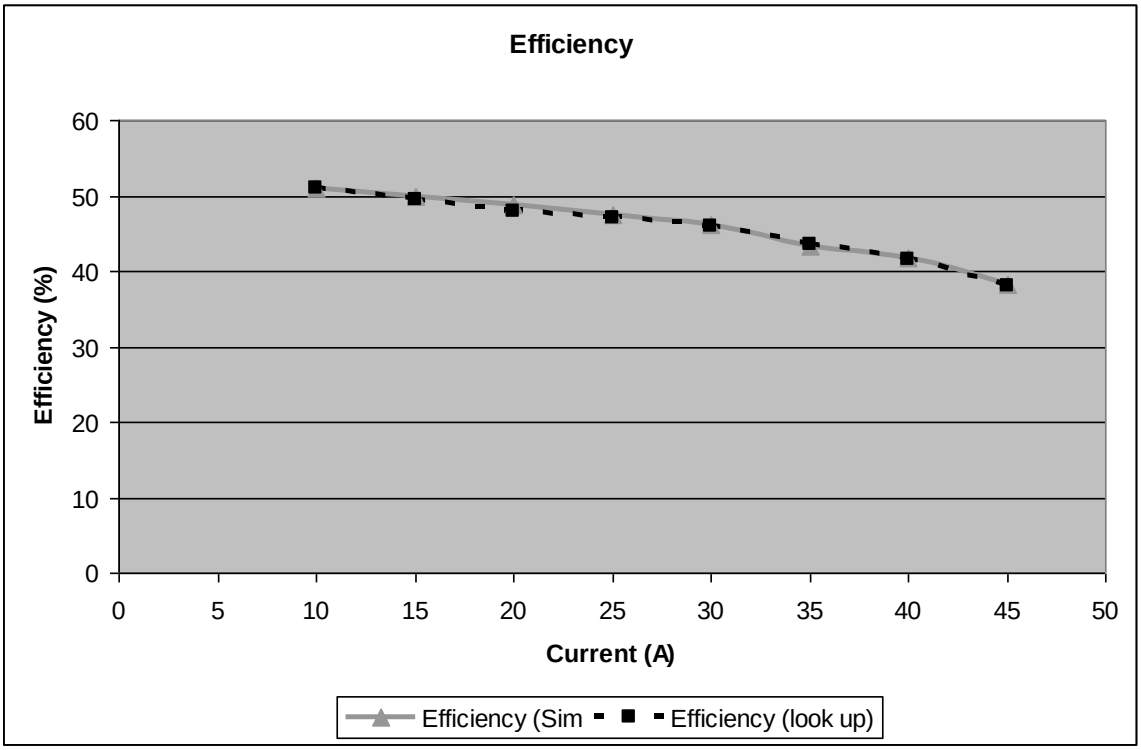

Figure 2.20 Efficiency results of FCE compared with Nexa

As with all previous results, the FCE results are comparable to and directly mimic the Nexa Fuel Cell module. These results show that the design of the FCE can directly replace the Nexa Fuel Cell for research, development, and testing purposes to reduce costs and development time and improve safety and working conditions.

In section 2.2.2, it was explained that a power factor correction circuit based on a DC-DC boost converter was used to improve the quality of the current on the AC-side of the DBR. Figure 2.21 illustrates the improvement made in the current waveform as a result of the adopted waveshaping technique. The switching-frequency ripples appear as a band around the centre line of the current waveform. The objective is to design a controller to shape the current in such a way that its centre line can closely follow the reference. In Figure 2.21, the current reference on the DC-side of the DBR has been shown in blue and the actual current on the AC-side has been shown to closely follow the reference (in red). The AC voltage has been shown in green to demonstrate that the current and voltage are in phase with one another. The challenge is to make the dead-time of the current around the zero-crossing disappear, as otherwise low-order harmonics produced will cause the quality of the waveform to deteriorate. Figure 2.22 shows the frequency spectrum of the AC-side current of the DBR. The frequency spectrum shows that the low-order harmonics have been drastically suppressed.

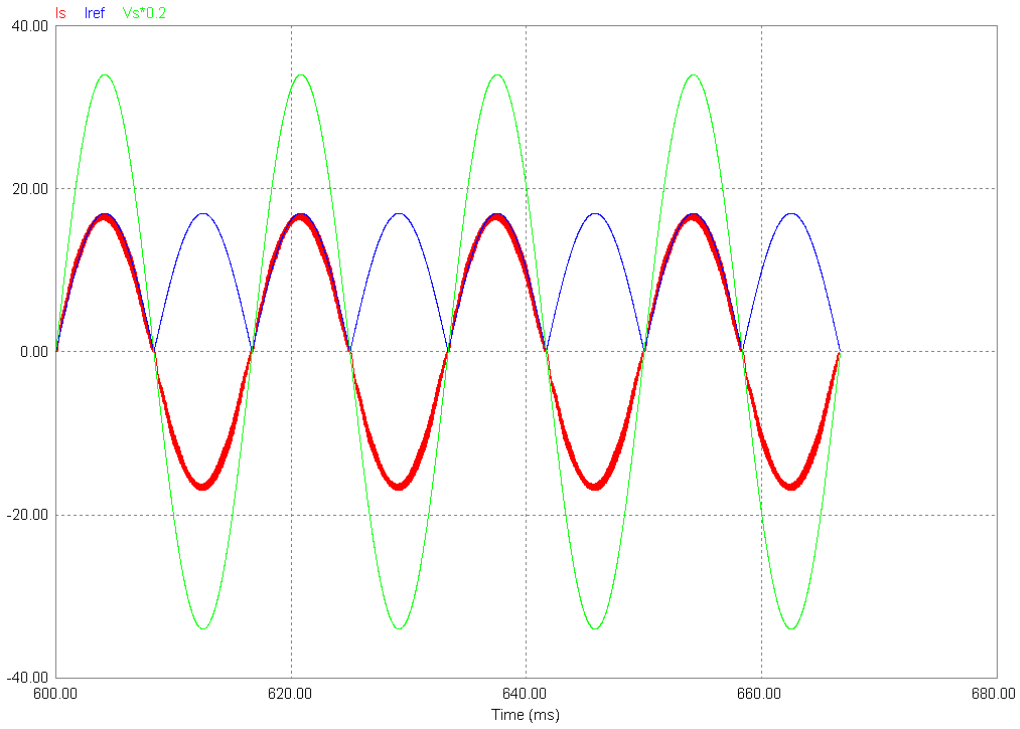

Figure 2.21 AC-side current and its reference at the interface of FCE with the grid

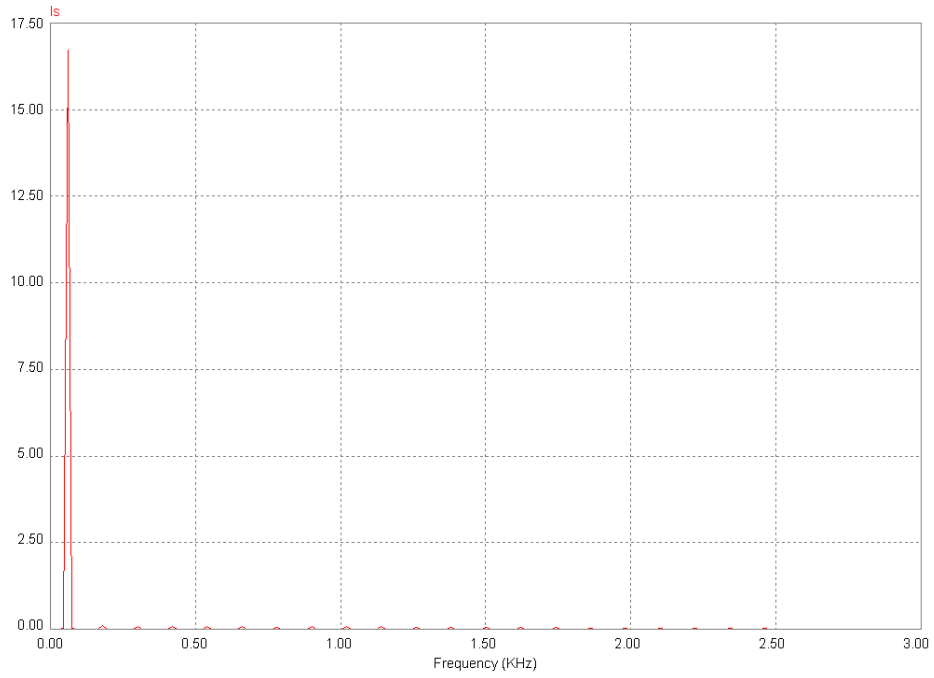

Figure 2.22 Frequency spectrum of the current drawn by the FCE from the grid

2.4 Summary

The objective of this chapter was to introduce a new fuel cell emulator. In section 2.1, a literature review was presented. It described a brief history of the fuel cell and explained the different types. Some vehicular applications were introduced from several automobile manufacturers, mainly GM. The operation of a fuel cell was also explained. Lastly, an existing fuel cell simulator was reviewed and a new idea for a fuel cell emulator (FCE) was introduced.

In section 2.2, the design of the FCE was explained. The main part of the FCE is based on a buck converter. To control the output power according to the Nexa polarization curve, the input and output power had to be conditioned. The input power to the FCE was converted from 120 V_{rms}-AC to 170 V-DC using a diode bridge rectifier and a boost converter acting as a wave shaping circuit. The output power was controlled by a boost converter that steps up the output voltage of the FCE to the voltage of the high-voltage DC bus. The boost converter also implements a time delay that matches the response time of the Nexa Fuel Cell module from Ballard Power Systems.

Lastly, in section 2.3, the simulation results of the FCE are presented. The results show that the FCE can behave as the Nexa Fuel Cell module at steady-state operating points under identical conditions.

Chapter 3

Bi-Directional Controllable DC Load

3.1 Literature Review

3.1.1 Concept

In the world today, there is an outcry for more efficient ways of producing and using energy. More efficient vehicles are a top priority. Part of the research concerning lower emissions and more fuel efficient engines involves a fuel cell-powered drive-train equipped with a regenerative braking system.

Regenerative braking is a novel concept commonly used in hybrid vehicles to capture the kinetic energy stored in the rotating parts of the moving vehicle when an attempt is made to stop the vehicle or reduce its speed. This energy is converted to electrical energy and stored in a battery or an ultra-capacitor bank to be used later when the energy is needed, e.g., during acceleration, thus reducing fuel consumption [19], [20]. In answer to the people who are skeptical about the true benefits of regenerative braking, a practical study performed in [19] proves that incorporating a regenerative braking system in a city bus, featuring frequent stops and short accelerations, would yield a potential savings of 59% in the cost of fuel.

In order to perform an experimental study on battery-electric and hybrid fuel cell vehicles in the setting of a lab, a scaled-down or a full-scale test bed should be used. The existing controllable DC loads, including the design introduced in [21] and discussed in section 3.1.2, are not regenerative, and as a result, are not capable of simulating regenerative braking. To fully study the regenerative mode of operation in a vehicle, the controllable load used must have regenerative capability, meaning it must a have bi-directional power flow capability.

Off-the-shelf controllable DC loads lack regenerative capability. They can be used for simulating a passive DC load profile as well as for testing the capabilities of different DC sources such as switch-mode power supplies, fuel cells, solar arrays, and batteries. Such loads can be costly and their design details are not available to customers. Also the capabilities of these devices are limited. The controllable DC load introduced in [21] features simplicity, speed, cost effectiveness, and versatility. This design consists of a DC-DC buck converter with a fixed resistor connected across its output terminals. Through proper control of the duty cycle of the switch, the resistance reflected on the input terminals of the buck converter is varied to realize the desired DC load profile. Even though this load can be adapted to a variety of applications, it is limited to one direction of power flow. Therefore, it cannot be used to emulate a vehicular load in a test bed where regenerative braking has to be studied. This shortcoming can be overcome using a bi-directional DC-DC converter.

3.1.2 Literature Review of Bi-Directional Converter Topologies

In searching for an appropriate bi-directional converter topology for the bi-directional controllable DC load, a few topologies were identified in the literature with applications in fuel cell systems energy storage and DC motor drives. These topologies are investigated in the following sub-sections to identify the most appropriate one for the application in hand.

3.1.2.1 Two-Stage and Three-Stage Bi-Directional Converters

The first topology to be considered has been proposed for connecting batteries and ultra-capacitors to the DC bus of a fuel cell-powered system [22]. Battery and ultra-capacitor are used in fuel cell systems as energy storage to respond quickly to fast load changes that cannot be followed by the fuel cell and make up for the delays involved in fuel cell cold starts.

The circuit diagram of the two-stage bi-directional converter topology proposed in [22] is shown in Figure 3.1. The control strategy is very straightforward. To control the power flow from the high-voltage side to the low-voltage side, the converter operates in buck mode (similar to the buck converter described in section 2.2.1), where the switch Q_1 is turned on and off according to a PWM pattern to realize the desired amount of power transferred, and Q_2 is left in the off position and only

its anti-parallel diode participates in operation. If it is necessary to reverse the direction of power flow, the converter is operated in boost mode, where the switch Q_2 is turned on and off under PWM control to make the power transfer follow the corresponding reference signal and Q_1 is left

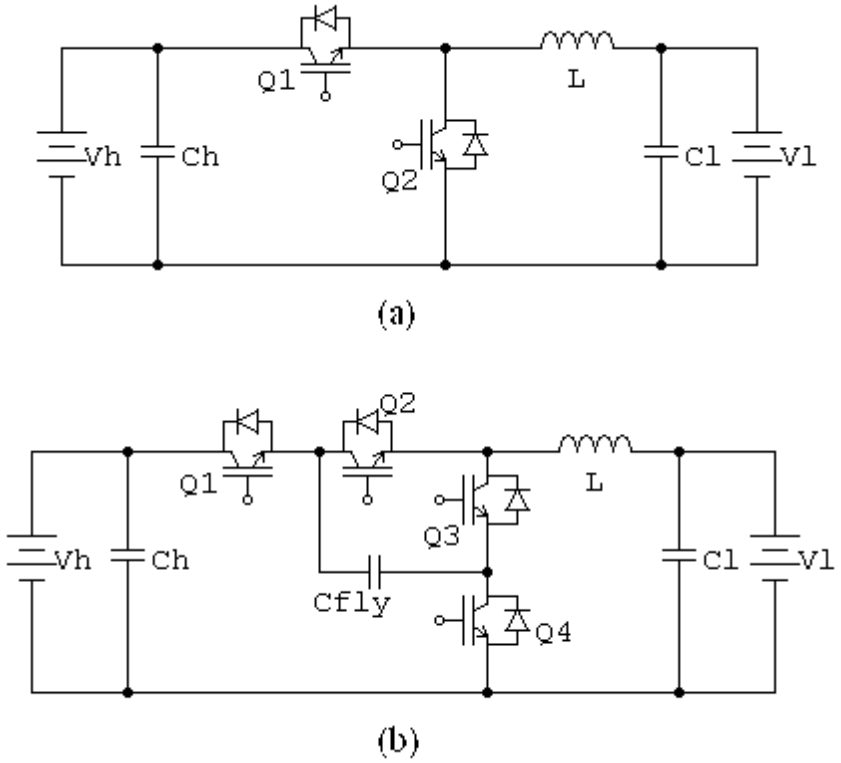

Figure 3.1 Bi-directional converter topologies introduced in [22]: (a) Two-stage bi-directional converter (b) Three-stage bi-directional converter.

in the off position and only its anti-parallel diode participates in the operation.

The author of [22] identifies two disadvantages to the design shown in Figure 3.1(a):

- High switch voltages, and
- Large components required when the input voltage is large, making the design bulky and expensive.

To overcome the drawbacks of two-stage bi-directional converter, reference [22] proposes a three-stage bi-directional topology, as shown in Figure 3.1(b). Adding another stage with two more switches and a capacitor, both power circuit and control system become more complex, making the design more costly. The advantages to this new design are:

- Less voltage stress on the switches, and
- Slightly smaller components.

In seeking a design for the bi-directional controllable load, the two-stage converter was preferred due its simplicity of both power and control circuits.

3.1.2.2 Isolated Bi-Directional Converters

This section introduces two different isolated bi-directional converters. The first topology, shown in Figure 3.2, has been proposed in [23]. The design has a higher degree of complexity compared with those proposed in [22]. The isolated bi-directional converter topology employs an H-bridge converter on the low-voltage side of the isolation transformer and a half-bridge converter on the high-voltage side. The switch S_c is an auxiliary switch that controls the clamp capacitor. Advantages of this topology include:

- Zero-voltage switching operation for all switches,
- Constant clamping voltage across all switches,
- Simple gate driver implementation,
- No voltage overshoot,
- No snubbing required, and
- Electric isolation.

Although this is an interesting design, the goal is to keep the bi-directional converter as simple and inexpensive as possible. This design uses seven switches and a transformer, complicating both power and control circuits, and making the design bulky and costly. This is not the most elegant and robust design. However, a non-isolated bi-directional converter topology, based on an H-bridge converter, was considered when making the final decision for the controllable load design.

The isolated bi-directional converter topology shown in Figure 3.3 has been proposed in [24] for interfacing energy storage devices with a DC bus. It is composed of two H-bridge converters on each side of an isolation transformer. The advantages of this design are capability of voltage level adjustment and isolation. The disadvantages are due to the use of a high-frequency isolation transformer and a large number of switches, as well as limitation in the permissible DC voltage range

based on power loss and peak current considerations. Again, for both designs shown in Figures Figure 3.2 and Figure 3.3, the advantages do not outweigh the complexity.

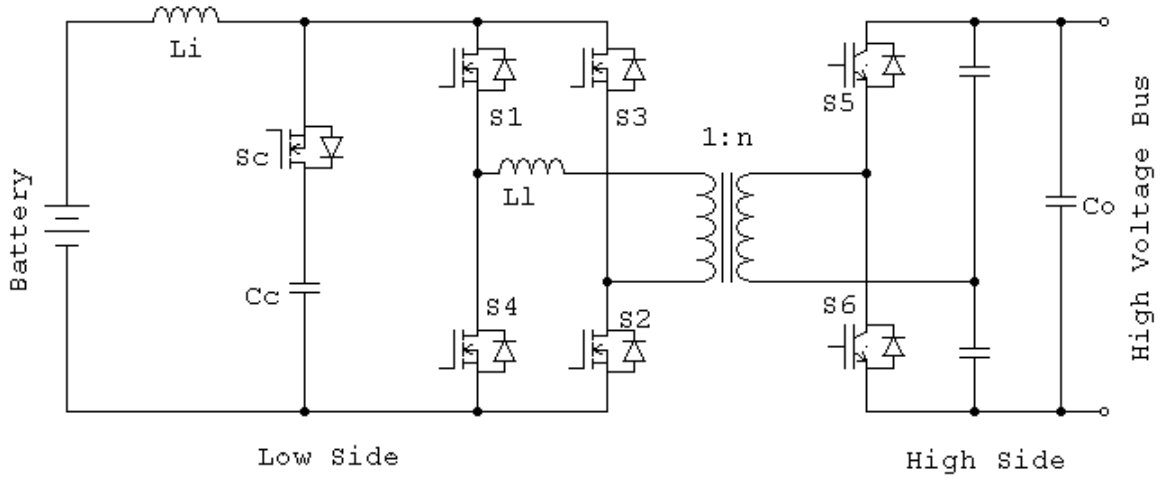

Figure 3.2 Isolated bi-directional converter proposed in [23]

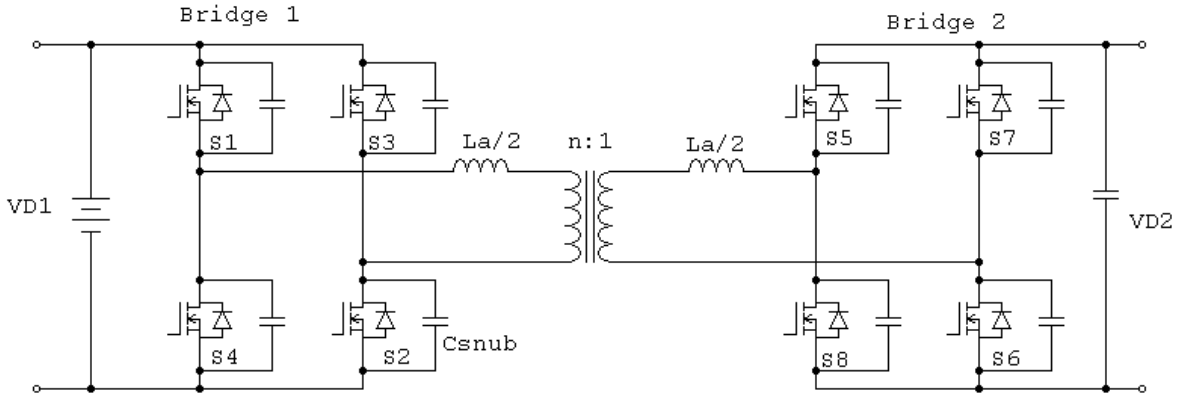

Figure 3.3 Isolated bi-directional converter proposed in [24].

3.1.2.3 H-Bridge Converter

A full-bridge DC-DC converter (also known as an H-bridge converter) [14], shown in Figure 3.4, can also realize a bi-directional DC-DC converter. The advantages of this converter topology are its simplicity of design and control, and lower number of switches compared with other topologies

derived from H-bridge topology. The disadvantage is in the use of higher number of switches with respect to bi-directional buck-boost topology.

After careful comparison of different possible topologies for bi-directional DC-DC converter for the regenerative controllable DC load, from the points of view of simplicity of design, number of components used, and ease of control, H-bridge and bi-directional buck-boost topologies stood out. After performing simulations with each topology, the bi-directional buck-boost topology emerged as the superior design. The H-bridge topology required two low-pass L-C filters, one on each side, and a larger number of switches. This would result in a comparatively higher cost and degree of complexity. The bi-directional buck-boost converter showed a better performance, lower cost and complexity, and fewer switching spikes. As a result, the bi-directional buck-boost converter was selected and used for the design of the controllable load.

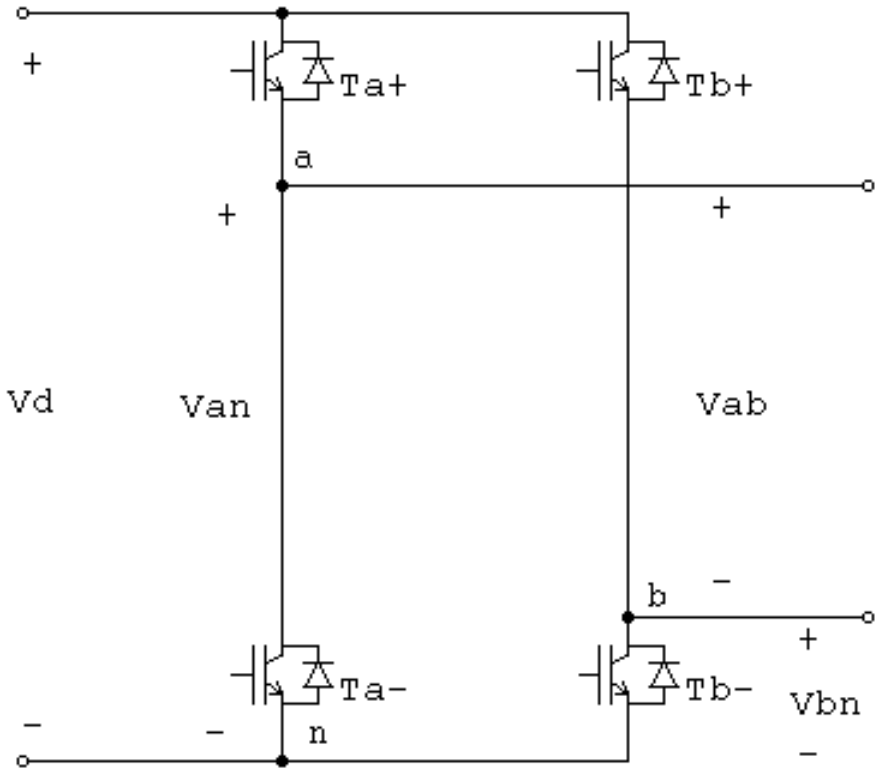

Figure 3.4 H-bridge converter [14]

3.2 Topology

The principle behind the operation of the bi-directional buck-boost converter is very simple. The circuit diagram of the proposed bi-directional controllable DC load based on this topology is shown in Figure 3.5. The two main switches S_1 and S_2 form a converter leg and are controlled by complementary gating signals based on the mode of operation of the circuit. When the power flow direction is from the high-voltage (source) side to the low-voltage (battery) side, the converter operates as a buck converter (see Figure 3.6(a)). When power flows in the opposite direction, the converter operates as a boost converter (see Figure 3.6(b)). In each mode of operation, one switch and the anti-parallel diode connected across the other switch are operational. At the low-voltage side of the converter, a resistor and a battery are connected in parallel. The resister-battery combination represents the power consumed by the load (power flow from the high-voltage side to the low-voltage side) and the energy stored in the load to be recovered and returned to the source (power flow from low-voltage side to the high-voltage side). When the system of Figure 3.5 represents a vehicular load in an electric or hybrid fuel cell vehicle test bed, the power flow from the high-voltage side to the low-voltage side represents motoring mode of the electric motor driving the wheels, whereas power flow from low-voltage side to the high-voltage side emulates regenerative braking.

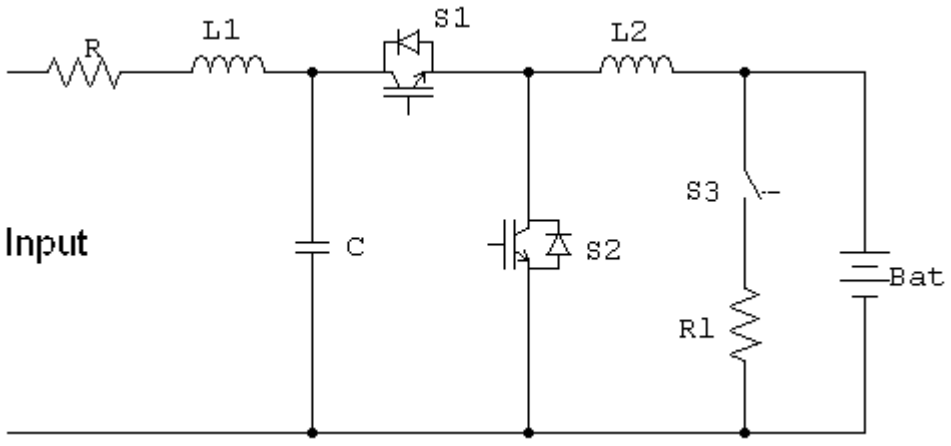

Figure 3.5 Proposed bi-directional controllable DC load

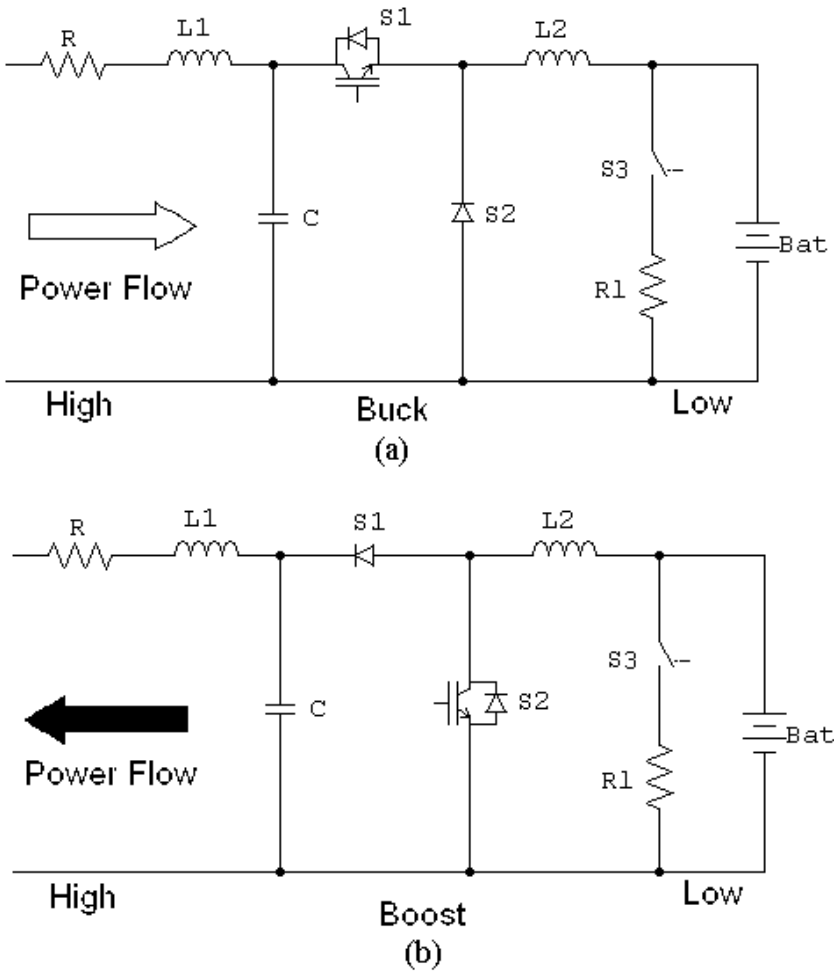

Figure 3.6 Topological modes of bi-directional controllable load. (a) Mode 1: Buck - load is drawing power. (b) Mode 2: Boost – load is providing power to the source.

Buck mode is considered the normal operational mode, and is used when the vehicle is requesting power from the high-voltage DC bus for propulsion (positive direction of power flow). This power is used to recharge the battery until the state-of-charge of the battery exceeds a pre-set level. This ensures that the battery will be able to provide the power equivalent to regenerative braking power when required at a later time. When the charge of the battery exceeds the pre-determined level, the power will be dissipated in R_l by turning the switch S_3 on.

Boost mode is the mode that simulates the regenerative braking (negative direction of power flow). In this case, R_l is disconnected by turning the switch S_3 off, and the battery discharges as power flows

out of its terminals towards the high-voltage side. The energy supplied by the battery simulates the electric power recovered through regenerative braking. The regenerative braking energy is normally stored in storage batteries or ultra-capacitors on the high-voltage bus for future acceleration and high-power-demand periods in the drive cycle.

The resistor, R, connected in series at the input terminals of the controllable load has a very small resistance and results in a very small power loss. The purpose of this resistor is to convert the difference between the input voltage of the controllable load and the voltage reflected on the source-side of the bi-directional buck-boost converter into a current. The direction of this current depends on the sign of the potential difference across the resistor (positive in the buck mode and negative in the boost mode), and represents the direction of power flow. Note that the series equivalent resistance of the input filter inductor may be large enough to serve the purpose of resistor, R, without any need for an additional resistor.

To design the load for the Nexa test-station setup, the load had to be designed to draw more power than the fuel cell could provide. This is necessary to test the full capability of the test-station. As mentioned in chapter 1, if a fuel cell is chosen based on the full power requirement of the vehicle, then the fuel cell will rarely operate at maximum power, and no energy storage is needed and the fuel cell would not be utilized to its full potential. By choosing a smaller fuel cell and installing adequate energy storage capacity, the propulsion system of the vehicle is more efficient. It was shown in chapter 2 and in appendix A that the maximum power output of the Nexa Fuel Cell was 1.2kW; therefore, the maximum power of the load was chosen to be 3kW.

It was stated in chapter 2 that the voltage of the high-voltage DC bus was 100V. This is the input voltage of the load. The battery voltage was chosen to be 60V to limit the current necessary for any amount of power flow. A battery model to simulate the battery was desired to observe the operation of the battery and monitor its state-of-charge (SOC), to incorporate actual limits on the amount of power it can provide for a given length of time, and also to make the simulation more realistic. The battery model found in [13] can be seen in Figure 3.7.

The lookup table in Figure 3.7 provides the actual output voltage of the battery based on its state-of-charge. The battery cell that was used for this model was EnerSys's Genesis EP, Purelead 12V battery, and the information for the lookup table and the capacity (in kWh) was found on its specifications sheet provided on the EnerSys website. To achieve 60V at the low-voltage side, five of these cells are combined in series.

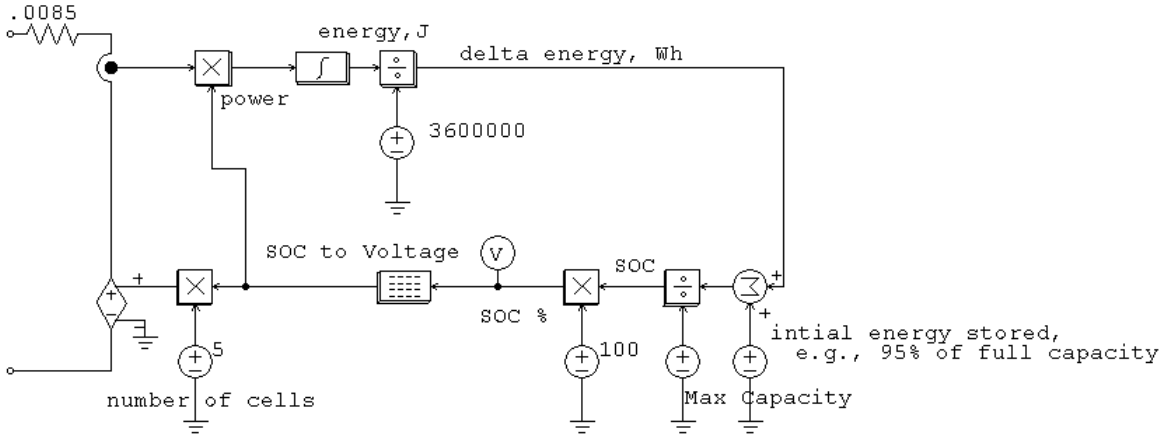

Figure 3.7 Battery model for simulation [13]

Now that the power level of the load and the voltage levels of each side of the converter have been chosen, the value for R_l can be calculated [25].

$$P_{\max} = \frac{V_{bat}^2}{R_l} \rightarrow R_l = \frac{V_{bat}^2}{P_{\max}} = \frac{60V^2}{3000W} = 1.2\Omega \tag{3-1}$$

By using Ohm's Law [17], the maximum current drawn by the load can be calculated.

$$I = \frac{V_{bat}}{R_l} = \frac{60V}{1.2\Omega} = 50A \tag{3-2}$$

In (3-1) and (3-2), V_{bat} is the battery terminal voltage, which is assumed to be equal to 60V. This is a reasonable assumption since the resistor R_l is switched in when the battery's state-of-charge is high, and battery voltage does not deviate considerably from 60V under such conditions. R_l will always draw 50A when S_3 is closed. If the load is not operating at maximum power, the remaining current will be provided by the battery. For instance, if the battery is fully charged, and the load draws

1000W, S_3 will be closed and thus R_l will draw 50A. But at 1000W, the current received by the resistor–battery combination is only 16.667A according to (3-1) and (3-2). As a result, the battery will discharge to provide the remaining current (by KCL [17]). So when the charge of the battery drops below the set point, S_3 will open and the battery will resume charging until it exceeds the set point again, in which case the cycle repeats. This will be shown in section 3.4.

3.3 Control

3.3.1 Reference Signal Calculation

In order for the controllable load to function properly, we must have a reference signal for the power at the terminals of the load. First, a drive cycle must be established for the test vehicle that will be simulated. The Environmental Protection Agency (EPA) provides several drive cycles on their website which are used for testing emissions on new vehicles manufactured by automotive companies that sell vehicles in the United States [26]. The urban drive cycle was used for its frequent stops and accelerations. The data was provided in mph. This can be seen in Figure 3.8.

Once an acceptable drive cycle was established, an algorithm was needed to convert from speed to power. First a simple conversion from mph to m/s was performed so that SI units can be used. Then to convert from meters per second to watts per second an algorithm needed to be derived. In order to do this, the power requirements for the vehicle had to be defined. To propel a vehicle forward, the power requirement for acceleration had to be determined. Power loss also had to be considered. Vehicles generally loose power through friction between the tires and the road, and through drag. The derivation for the algorithm is as follows [17] where *F* is force and *P* is power:

Gross Power:

$$F = m \times a \tag{3-3}$$

$$P = F \times v \tag{3-4}$$

$$P_{accel} = m \times a \times v \tag{3-5}$$

Friction:

$$F_{friction} = \mu \times F_N = \mu \times mg \tag{3-6}$$

$$P_{friction} = \mu \times mg \times v \tag{3-7}$$

Drag:

$$F_{drag} = \frac{1}{2} C\rho A v^2 \tag{3-8}$$

$$P_{drag} = \frac{1}{2} C\rho A v^3 \tag{3-9}$$

Total Power:

$$\begin{aligned} P_{net} &= P_{drag} + P_{friction} + P_{accel} \\ &= \frac{1}{2} C\rho A v^3 + mg\mu v + vma \end{aligned} \tag{3-10}$$

The power curve will vary based on the mass, *m*, cross-sectional area, *A*, drag coefficient, *C*, and the coefficient of friction, μ, of each vehicle. Thus, a vehicle needed to be specified to obtain a power curve. A 2008 Honda Civic was chosen as the test vehicle because it is a typical vehicle in North America. The parameters associated with the specific vehicle used for the study were obtained from the manufacturer's website. Velocity, *v*, was designated by the drive cycle from the EPA and acceleration, *a*, was calculated from the change in velocity from one point to the next. Others are well known, such as the gravitational constant, *g*, and the density of air at sea level, ρ.

After performing the calculations using (3-3) through (3-10), the maximum power needed to propel the vehicle is on the order of 25kW. It is impractical to build and operate a load of this power rating in a small laboratory; therefore, the power curve was scaled down to 10% of the nominal. This power can be realized by the 3000W controllable load designed and explained above. Figure 3.8 shows the calculated power versus time together with the corresponding EPA urban drive cycle.

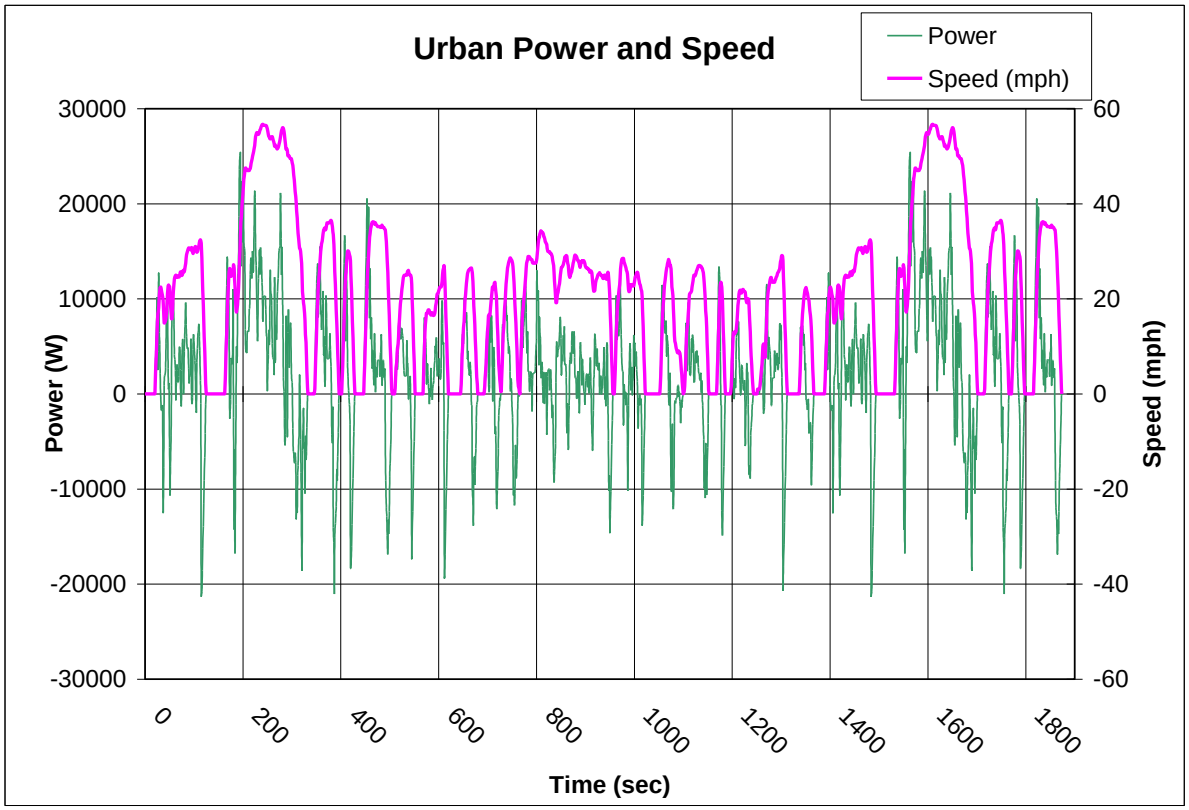

Figure 3.8 Speed and Power of Urban Drive Cycle [26]

3.3.2 Control Circuit

The control of the controllable load is rather simple. It consists of two very similar control loops, each responsible for one mode of operation. The output of the buck control loop goes to S_1, and the output of the boost control loop goes to S_2. The reference signal for power was calculated in the previous section. The actual reference signal that goes to the control loops is a current reference signal. The power reference is divided by the measured voltage on the low-voltage side to obtain the current reference signal. The current feedback from the low-voltage side is then compared with the current reference to obtain an error signal. It was established in the section 3.2 that the buck mode of the converter refers to the positive direction of power flow, whereas the boost mode refers to the negative direction of power flow. Since the voltage polarity does not change, the only way to obtain

a negative power is to reverse the direction of current. A negation block is used in the boost control loop to compensate for the fact that both reference and actual values for the current are negative. The control scheme is shown in Figure 3.9.

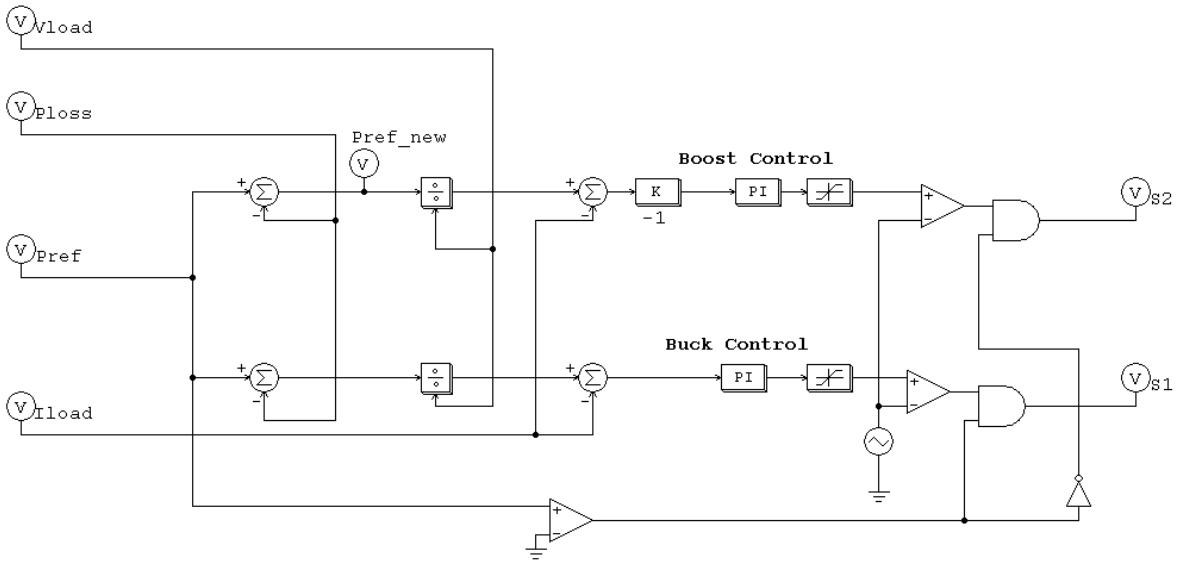

Figure 3.9 Control scheme of bi-directional DC controllable load

The objective is to control the power at the input terminals of the controllable DC load. However, it is more efficient to control the power on the low-voltage side. To derive the reference signal for the desired power on the low-voltage side from the reference signal for the desired power at the controllable load terminals, the power loss due to current flowing in the resistor, R, at the load input terminals has to be taken into consideration. The calculations involved in finding the power loss in R and the current reference signals on the low-voltage side are given by (3-11) and (3-12) [25].

$$P_{loss} = I^2 R = \left(\frac{P_{ref}}{V_{input}} \right)^2 \times R \tag{3-11}$$

$$\frac{P_{ref} - P_{loss}}{V_{load}} = I_{ref} \tag{3-12}$$

Note that for buck mode, the power on the low-voltage side is less than the power needed at the input terminals; therefore, the power loss must be subtracted from the load input power reference. For the

boost mode, the power on the low-voltage side should be greater than the power at the input terminals. However, this power is negative, i.e., the absolute value of the power on the low-voltage side should be greater than that required at the load terminals. Thus, equation (3-12) will work for both loops.

In addition to the control loops, there is some logic circuitry that contributes to controlling the load. As shown in Figure 3.9, this circuit is used to determine the mode of the converter. The power reference signal is compared with zero. The output is 1 if the power reference is positive, meaning buck mode has to be used. The output is 0 if the power reference is negative, indicating that boost mode must be used. This mode identification signal is then sent to a pair of AND gates where this signal is ANDed with output of each control loop. The signal leading to the AND gate of the boost control loop is inverted with a NOT gate. Thus when the mode signal is 1, the AND gate for the boost control loop will output a low signal to S_2 thus turning the switch off. When the mode signal is 0, the AND gate for the buck control outputs a low signal to S_1 thus turning the switch off.

The other operation that needs a logic circuit is the control of S_3 that dictates when the load resistor is to be switched in or out. This was briefly explained in section 3.2. To control the switch, it must be determined when the power should go to the battery and when it should go to the resistor. Obviously, if the converter is in boost mode, the load resistor must be disconnected. When the converter is in buck mode, there are two conditions under which the battery-resistor combination can be connected. If the battery needs to be charged, the incoming power should go to the battery, thus the resistor should be disconnected. If the battery is fully charged to its set value then the resistor should consume any incoming power. For the logic circuit, the state-of-charge (SOC) of the battery is compared with a set value. 95% was chosen to allow for a safety margin of error to prevent the battery from overcharging. Assuming the converter is in buck mode, if the SOC is greater than or equal to 95% then the output of the comparator is 1. This signal is then sent to the switch to close it. When the switch is closed, the resistor will draw 50A. However, if the load is not operating at maximum power then the incoming current will be less than that. The remaining current will come from the battery forcing the battery to discharge. When the battery discharges, the SOC will drop

below 95%. When this occurs, the output of the comparator will be zero thus turning the switch off. Then the incoming current will charge the battery back to 95%, causing the switch to close again. This cycle will repeat itself until a braking sequence occurs. When the drive cycle calls for a braking sequence, the converter will go into boost mode and cause the battery to discharge. In this case, switch S_3 is opened and the battery supplies power to the load terminals. These simulation results are illustrated in section 3.4.

3.4 Simulation Results

The bi-directional controllable DC load was designed and simulated on the computer using PSIM, a power electronic circuit simulation package by PowerSim Inc. Several simulations were run to test the load under normal conditions as well as under stress to show its maximum capabilities.

The first test was under normal conditions for longevity. Only a portion of the drive cycle shown in Figure 3.8 was used for this longevity test, to reduce the simulation run time and to prevent redundancy. This portion is shown in Figure 3.10. As stated in section 3.3.1, the load was designed for a small scale laboratory set-up; therefore, the power request of the full-size vehicle was scaled down to 10% of its original value. This will keep the power reference within the range that the load has been designed for. The control circuit also uses a limiter that the power reference signal must pass through before it is fed to the control circuits. This is another safety feature that has been designed into the load so when an experimental prototype is built, the power reference cannot go beyond the capabilities of the load. Similar to the tests that were run for the FCE, the time interval chosen was 100ms, so the load is held at each point in Figure 3.10 for 100ms.

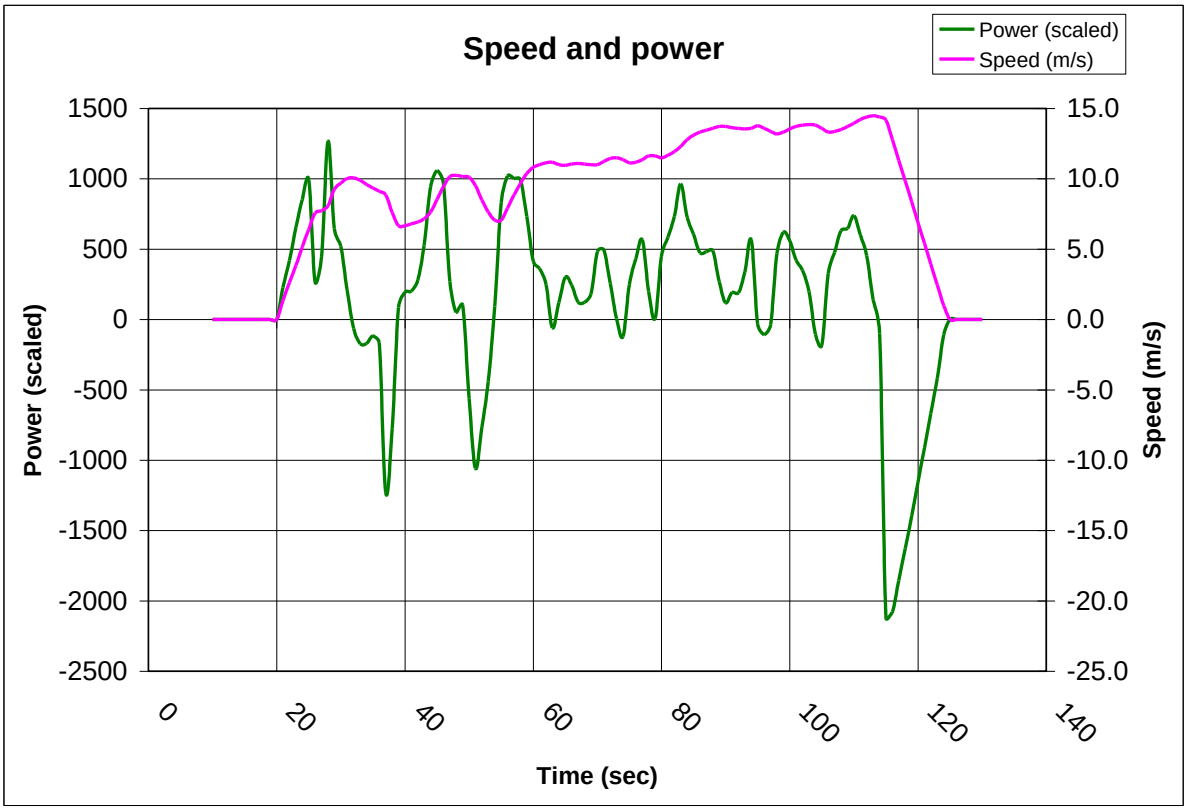

Figure 3.10 Selected portion of the drive cycle shown in Figure 3.8 and the corresponding power used for the load simulation in PSIM.

The PSIM simulation results are shown in Figure 3.11 and Figure 3.12. The power reference and the actual power at the load input terminals are shown in two ways. In Figure 3.11, the two signals are shown on the same plot to show that the power at the input terminals is controlled very well, in accordance with the reference. Since it is difficult to tell the two signals apart on one plot, they are shown individually in Figure 3.12. This figure shows that there is a slight difference between the two signals. The actual power experiences some small spikes when the load goes to a new operating point following a step change in the reference. This is the result of a fast controller and switching harmonics. The spikes have been minimized by the L-C filter.

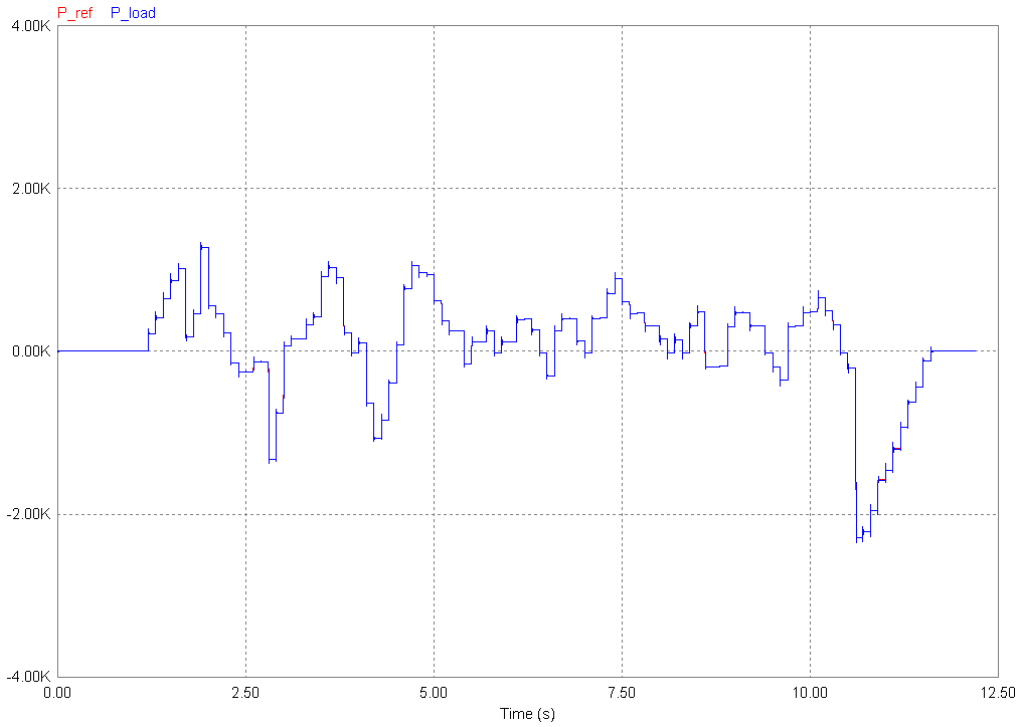

Figure 3.11 Simulation results: Power reference and actual power at the load input terminals

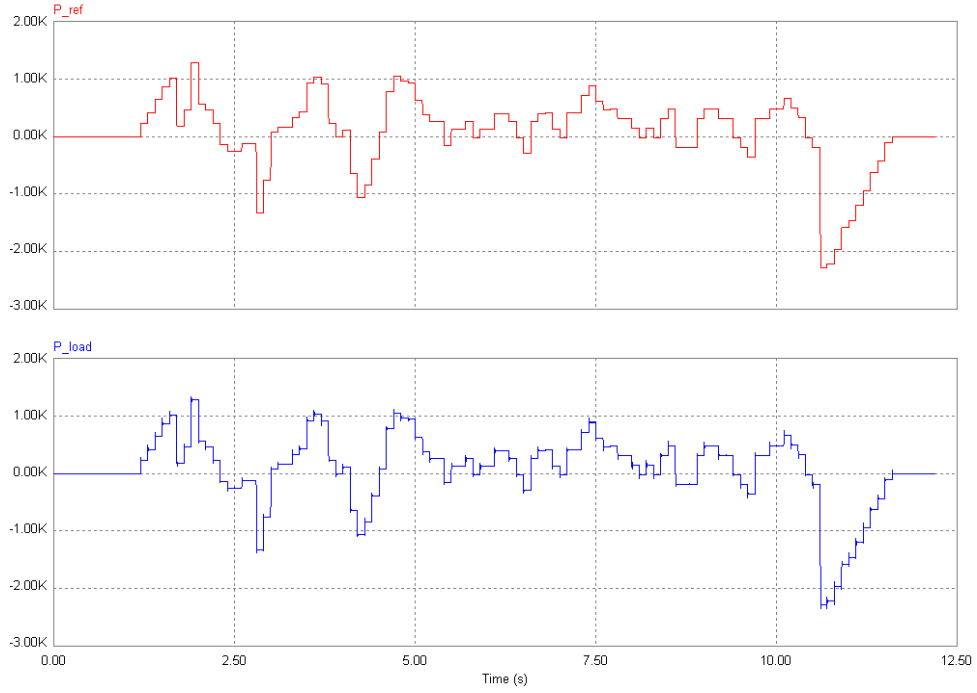

Figure 3.12 Simulation results: Power reference (top) and actual power (bottom)

Another interesting result to show is the functionality of the battery-resistor combination. Figure 3.13 shows the load current on the low-voltage side of the converter, the load resistor current, and the battery current. This operation has been explained in sections 3.2 and 3.3.2. The battery current matches the load current on the low-voltage side when the resistor is not switched in. When the resistor is switched in, it draws 50A. During this time the battery discharges to provide the difference between the load current on the low-voltage side and the 50A of the resistor current. Then the SOC of the battery will fall below 95% and the resistor is disconnected. The load current and the battery current will be equal again as the load current begins to charge the battery. When the SOC of the battery reaches 95% again, the resistor switches in and the whole cycle repeats itself. Since this can be difficult to see in Figure 3.13, Figure 3.14 provides a close up of the switching of the resistor in conjunction with the charging and discharging of the battery.

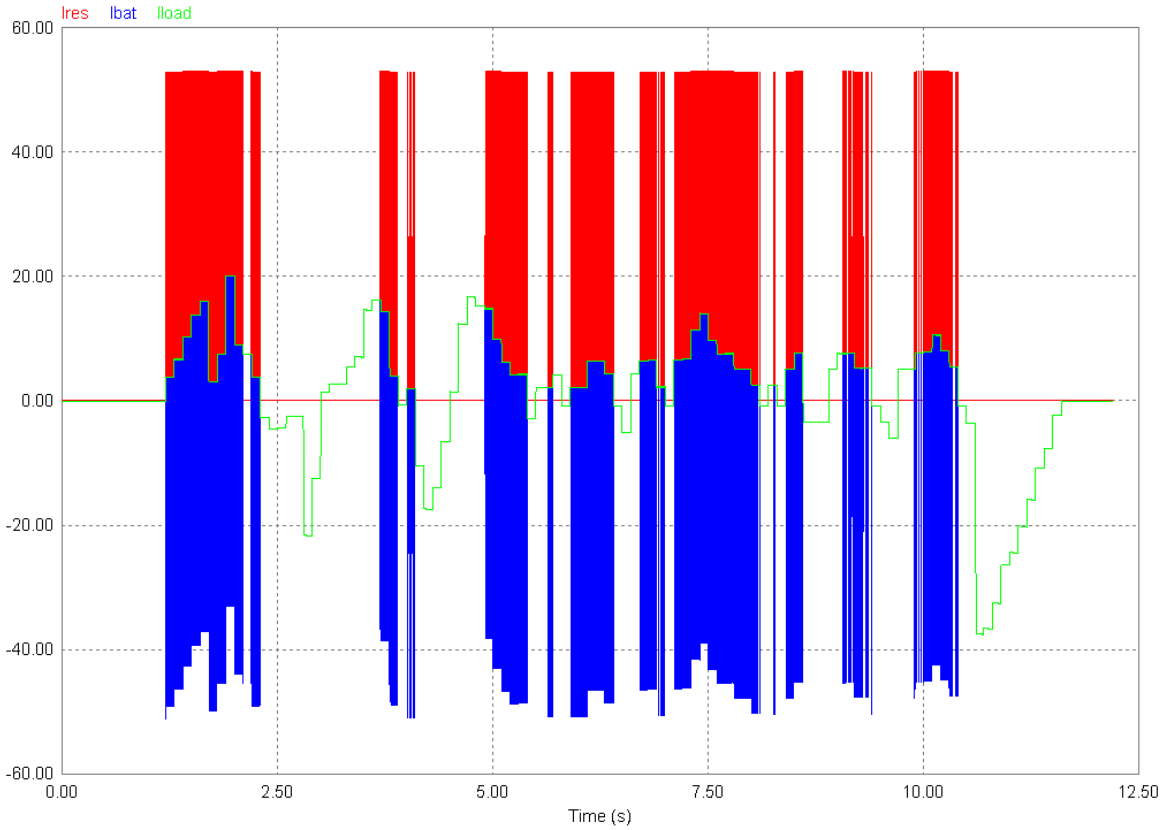

Figure 3.13 Battery-resistor combination simulation results of bi-directional converter: Low-voltage side load current (green), load resistor current (red) and battery current (blue).

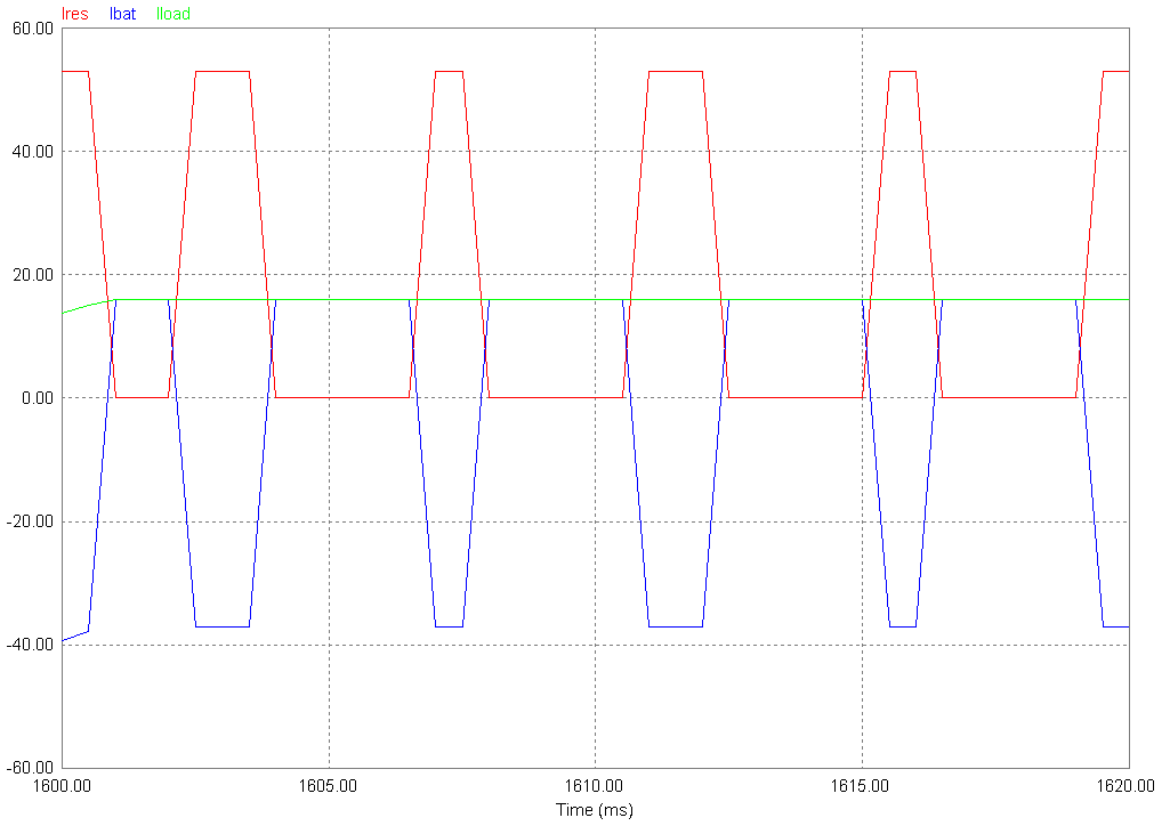

Figure 3.14 Close-up of battery-resistor combination simulation results of Figure 3.13

The final result to show from the longevity simulation test is the SOC of the battery. There is no logic, or safety measures in place to prevent the battery from over-discharging because the braking periods of a vehicle are not long enough to fully discharge the battery. In reality, assume a vehicle is traveling at 60mph. If the driver were to brake immediately, it would take 3 seconds for the vehicle to come to a full stop. As the vehicle slows down, less and less energy can be extracted from the regenerative braking system during the braking time [27]. Most braking periods are not for emergency stops so they will take longer. But again, the vehicle will slow down and its energy will decrease over the time period. In the simulation, the battery that provides the power of the regenerative braking system will discharge during the braking period. As the speed of the drive cycle decreases, the power reference will be reduced and the battery will discharge more slowly until the drive cycle indicates a full stop or begins an acceleration period. The drive cycle that was used for

this test was an average drive cycle, with average braking times. The SOC of the battery is shown in Figure 3.15. It can be seen that the SOC of the battery does not come close enough to 0% for over-discharging to be a concern. It can also be seen that the battery charges and discharges in accordance with the reference signal. It is also shown that the battery is not allowed to fully charge beyond 95%; it appears to remain constant at 95%. The changes in the SOC, when the load resistor is switched in, are not large enough to be seen.

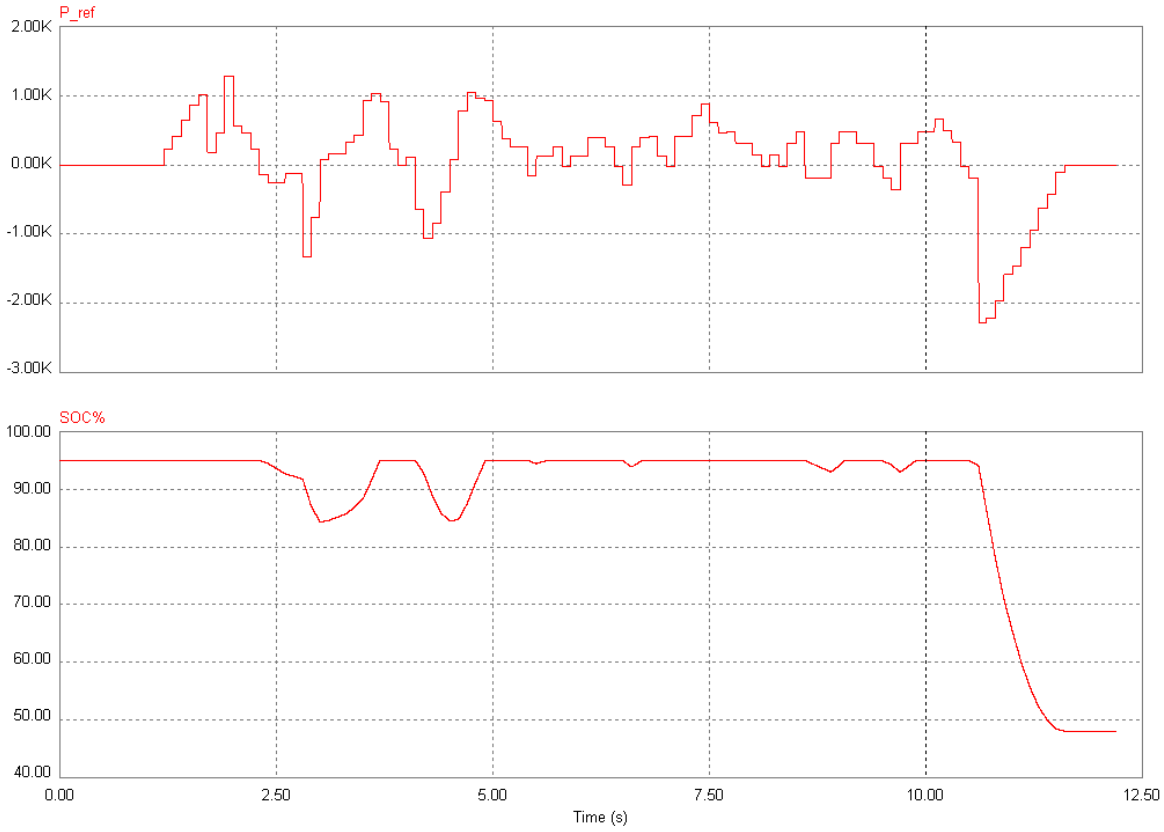

Figure 3.15 Power reference and SOC of battery during longevity simulation

The second simulation performed in PSIM was a stress test to demonstrate the maximum capabilities of the load. The drive cycle was replaced with a reference signal that begins at 3000W and decreases by 1000W every 100ms, until -3000W is reached. In Figure 3.16, the power reference and actual power at the input terminals, as well as the power reference and actual power on the low-voltage side are shown. Recalling from section 3.3.2, the power reference on the low-voltage side of

the converter was adjusted by subtracting the power loss from the power reference at the load input terminals. The difference between these signals can be seen in Figure 3.16. Actual power at the terminals is in red, the power reference at the input terminals is in blue, the power reference on the low-voltage side is in green and actual power on the low-voltage side is in pink. It is also shown that the power on both sides of the converter is controlled very well over the entire range of load power variations. There is also no significant delay from one operating point to the next. This mimics the fact that the power in a vehicle can change almost instantly depending on the actions of the driver and its environment. It will be shown in chapter 4 that this is much faster than the FCE is able to follow. The remedy for this problem will be discussed in chapter 4.

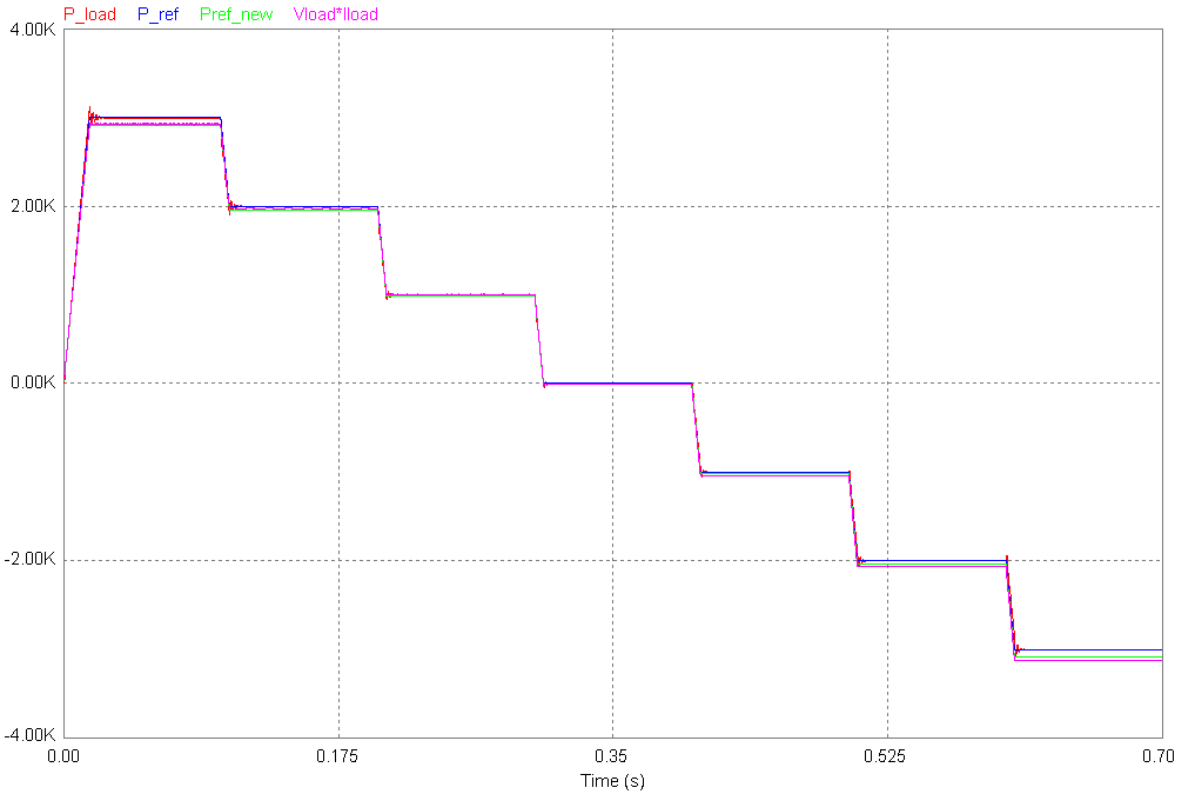

Figure 3.16 Stress test simulation results of bi-directional controllable DC load.

3.5 Summary

In this chapter, a few bi-directional DC-DC converter topologies were reviewed and a novel bi-directional DC load was proposed. In section 3.1, a literature review of bi-directional DC-DC converters was performed, stating the advantages and disadvantages of each configuration. Some were complicated and expensive to implement. In an effort to keep the design simple and inexpensive, a basic bi-directional buck-boost topology was selected to realize the bi-directional controllable DC load.

In section 3.2, the topology of the load was discussed. The modes of operation were determined by the sign of the power reference signal. If the power reference is positive, then the load circuit is in buck mode, with power flowing from the high-voltage side to the low-voltage side. If the reference is negative, then the load circuit is in boost mode, with power flowing from the low-voltage side to the high-voltage side. For the power to change direction either the current must change direction or the voltage must change polarity. The bi-directional load has been designed so that the current will change direction. The bi-directional load has also been designed with a battery-resistor parallel combination. When the converter is in buck mode, the battery will charge up. When the battery is charged to the pre-specified level, the resistor will switch in to prevent the battery from over charging. When the bi-directional load is in boost mode, the resistor is disconnected and the battery discharges to simulate regenerative braking. The power provided by the battery represents the power that would be recovered in a vehicle with a regenerative braking system. This power is returned to the source.

In section 3.3 the control of bi-directional load was explained. The control system incorporates two different control loops, one for each mode the converter operates in. To determine which mode the converter is in, the reference signal is compared to zero. If it is positive, the load circuit is operated in buck mode. When the reference signal is negative, the load circuit is operated in boost mode. The switch for the load resistor is controlled separately. The SOC measured for the battery is compared with a set point. If it is greater than or equal to the set point then the resistor is switched in. When the SOC drops below the set point the resistor is disconnected.

Lastly, in section 3.4, the simulation results of the bi-directional controllable DC load are presented. The results show that the load can simulate the scaled-down power requirements of a vehicular load. The results also show the operation of the battery and the load resistor.

Chapter 4

Test Station

4.1 The Setup

Now that the main components of the test station have been introduced and discussed in chapters 2 and 3, the test station can now be explained. The goal of this chapter is to prove, through simulation, that a fuel cell-based vehicular drive train can be effectively emulated by a test station with the structure shown in Figure 4.1.

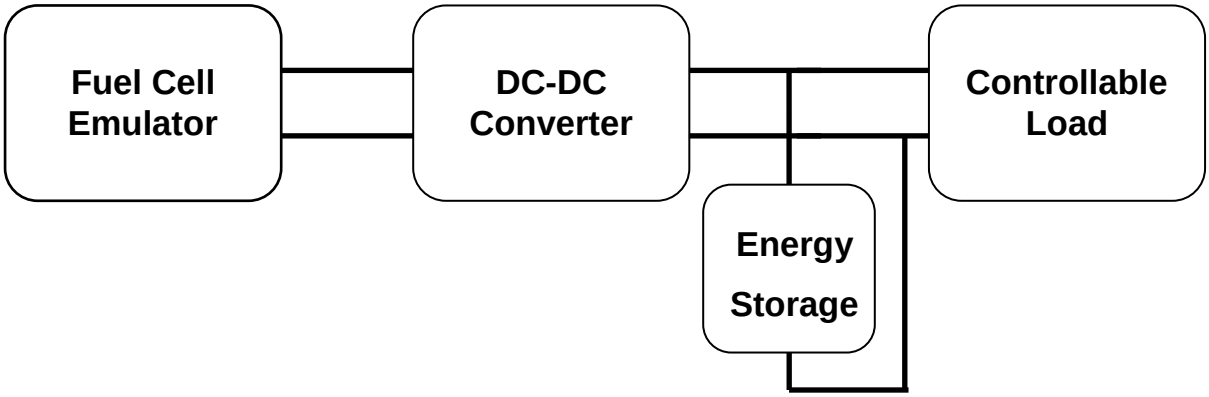

Figure 4.1 Proposed topology of test station

The fuel cell emulator (FCE) is the main power source and the bi-directional controllable load is made to draw power according to a given drive cycle. The DC-DC converter controls the output power of the FCE and maintains the voltage on the high-voltage DC bus. As mentioned in chapter 2, the design of the fuel cell emulator is based on the Nexa Fuel Cell module. Typically, fuel cells are slow in response to variations in the load [10]; therefore, some energy storage must be implemented to supply the required supplemental power during the transients. The energy storage system must provide the difference in power when there is a deficit, and absorb it when there is a surplus. Since,

for the system under study, only one energy storage device was chosen, there is no need for a converter to interface with the high-voltage DC bus and the power from or to the energy storage device will be automatically decided and controlled. In fact, both the DC-DC converter and the bi-directional controllable DC load are current controlled, and thus, by KCL, the battery will provide (or absorb) the remaining current.

The energy storage device that was chosen for this topology is a battery. Other energy storage devices as well as combinations of different types can be utilized as well; this will be explained in further detail in chapter 5. The storage battery was modeled using the same model from [13] that was used for the load. The battery that was modeled was a High Power Lithium Ion ANR26650ml battery manufactured by A123 Systems Inc. A Lithium Ion battery was chosen because Lithium Ion batteries are much lighter and can charge and discharge more quickly than lead-acid batteries. They also have a wider range of operation from 0 to 100% of their charge capacity, have a longer life span, and are more environmentally friendly. Lead-acid batteries are safer and more efficient if they are operated at a narrow range like 50% - 90% of their charge capacity; however, their charging and discharging time is still not fast enough for this purpose. They are also one of the heaviest batteries and can be hazardous and dangerous if not properly maintained. The model is shown in Figure 4.2 below.

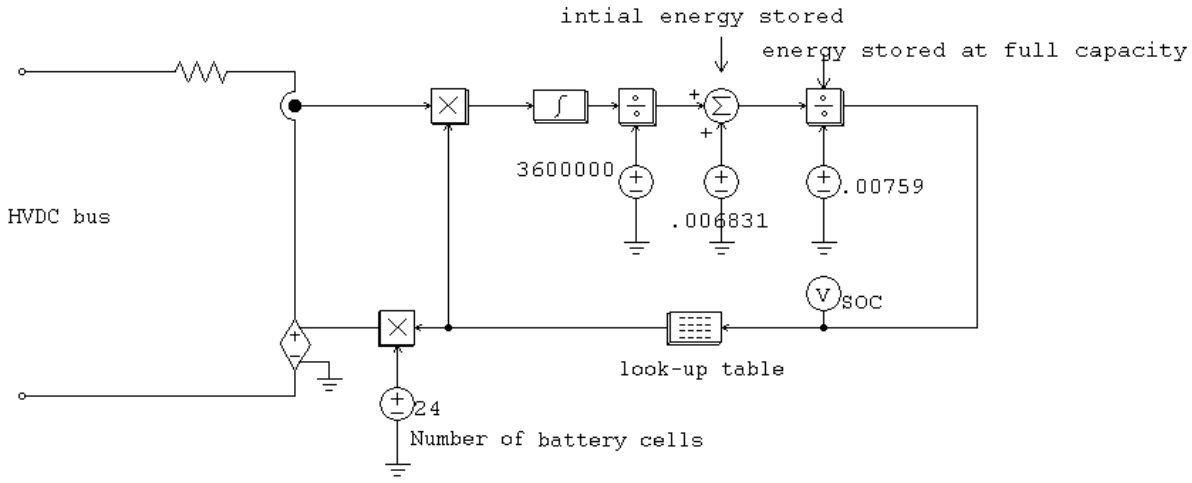

Figure 4.2 Model of storage battery that is connected to the high-voltage DC bus

The battery has a maximum voltage capability of 3.3V. To connect it directly to the high-voltage DC bus, the voltage must be close to 100V. Figure 4.2 shows that 24 batteries were connected to reach approximately 80V. This voltage is acceptable for both the FCE and the bi-directional controllable DC load. The information from the lookup table was acquired from the data sheet of the Lithium Ion battery. From Table 4-1, it can be seen that the Lithium Ion battery can maintain a constant voltage over a wide range of charge storage. This is a major advantage to using this type of battery.

Table 4-1 Data of A123 Systems'Lithium Ion Storage Battery

SOC	Voltage
0	2
10	3.2
20	3.3
30	3.3
40	3.3
50	3.3
60	3.4
70	3.4
80	3.4
90	3.4
100	3.6

Now that the energy storage has been chosen, the test bench can be simulated. In order for the components to work together, some information must be exchanged between them. These signal exchanges are shown in Figure 4.3.

To prevent the storage battery from overcharging, the load must know when it can perform regenerative braking and when a mechanical brake should be used. Regenerative braking can be

performed as long as there is a place to store the energy. If the storage battery is fully charged, then mechanical braking must be used. To accomplish this, the SOC of the storage battery is sent to the load where a logic circuit selects to send the power reference (derived from the drive cycle) or zero to the control circuit of the load. If the SOC of the storage battery is greater than a pre-determined set point and the reference signal is negative, indicating a braking period is occurring, then the logic circuit will send a zero to the control circuit of the load indicating that mechanical braking has to take place. The zero reference signal is chosen because there is no electrical power being requested or stored while the vehicle is executing mechanical braking. All of the kinetic energy the vehicle has in its momentum is being expelled in the mechanical brakes as heat and none of it is being stored because the storage component is full. The storage battery must have a pre-determined set threshold to implement mechanical braking to prevent it from overcharging. If the set point was at 100%, when the power drawn by the load goes to zero, the FCE will take time to reach zero and thus there will be a surplus of power that the battery is forced to absorb by conservation of power. This surplus will overcharge the battery. If the set point were lower, around 80%-90% then the battery will still have room to absorb the surplus power and will not overcharge.

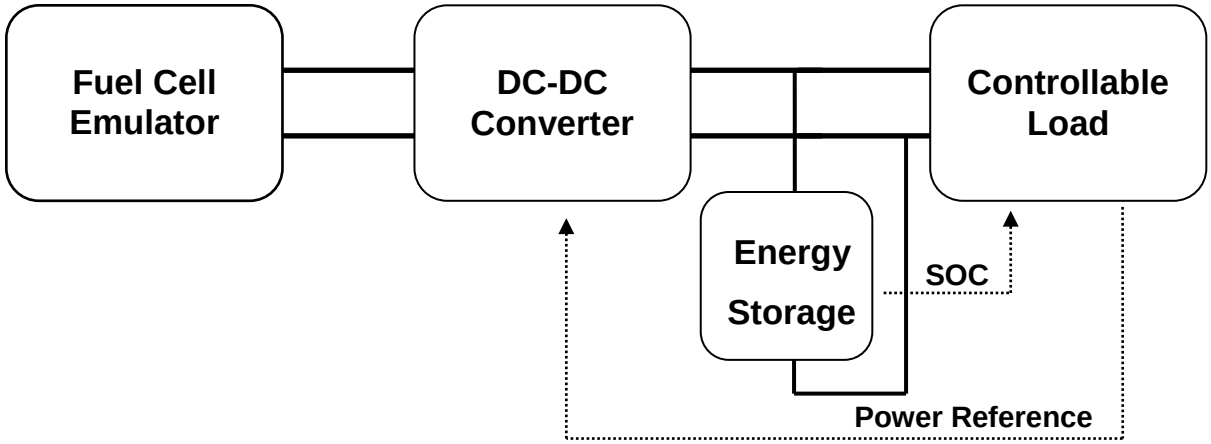

Figure 4.3 Signal exchange between modules in the test bench

It was mentioned in section 2.2.3 that the DC-DC converter uses the power reference signal of the load to determine the current reference of the boost converter. It uses Table 2-1 as a lookup table to

convert from power to current. This also ensures that the output of the FCE is on the polarization curve of the Nexa Fuel Cell power module.

4.2 Simulation Results

The test bench setup was simulated on the computer using PSIM, a power electronic circuit simulation package by PowerSim Inc. Only one simulation was needed as the maximum capabilities of the load and FCE were shown in previous chapters.

The simulation was performed using the same drive cycle that was used to test the bi-directional controllable DC load. It is repeated in Figure 4.4 for ease of reference.

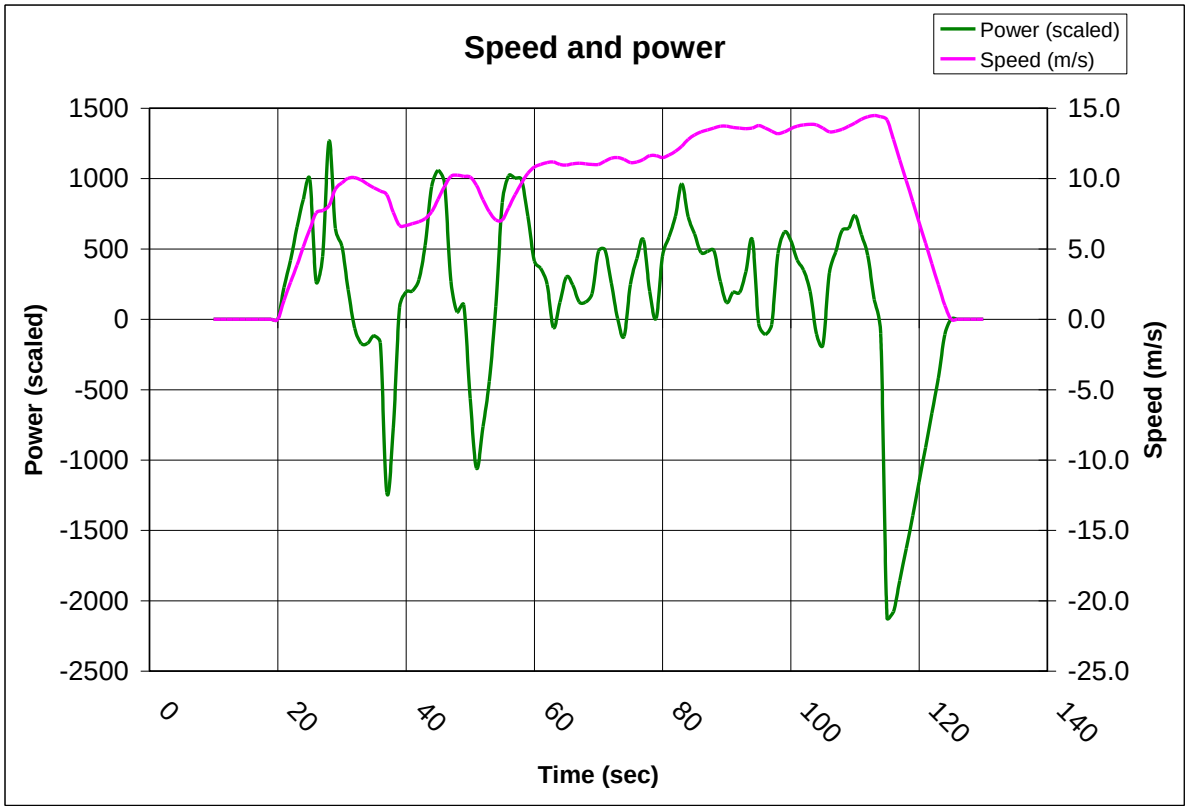

Figure 4.4 Drive cycle used to evaluate the test bench set up [26]

First, the power requested by the load and the total power provided by the FCE and the battery are shown in Figure 4.5.

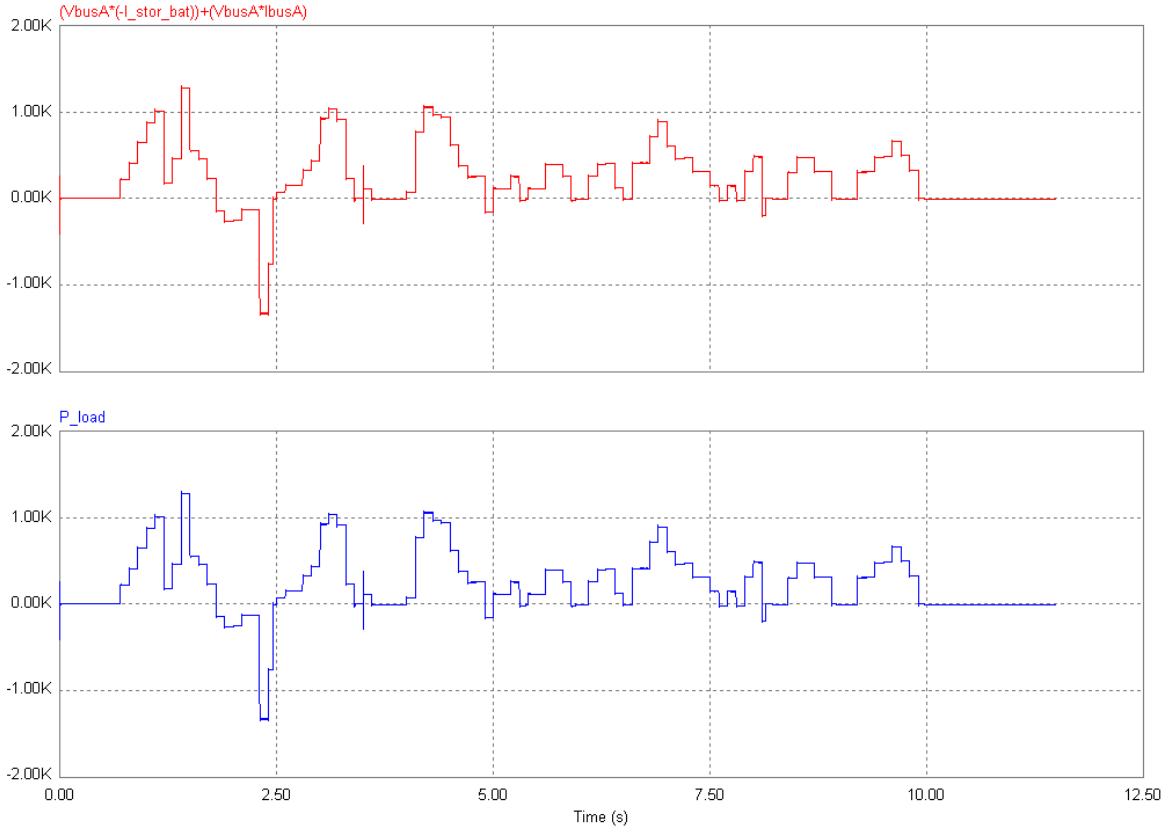

Figure 4.5 Test bench simulation results: total power provided by the test bench system (top), power requested by the load (bottom)

Next, Figure 4.6 shows the powers supplied by the individual components. The output power of the FCE is shown in red, the output power of the boost converter is in blue, and the output power of the battery is in green. The difference between the output powers of the FCE and the boost converter demonstrates the power loss in the converter. The power supplied and absorbed by the battery makes up for the difference between the power of the load and the power of the FCE, as expected. The sum of the powers supplied by the DC-DC converter and the battery equal to the power supplied signal in Figure 4.5.

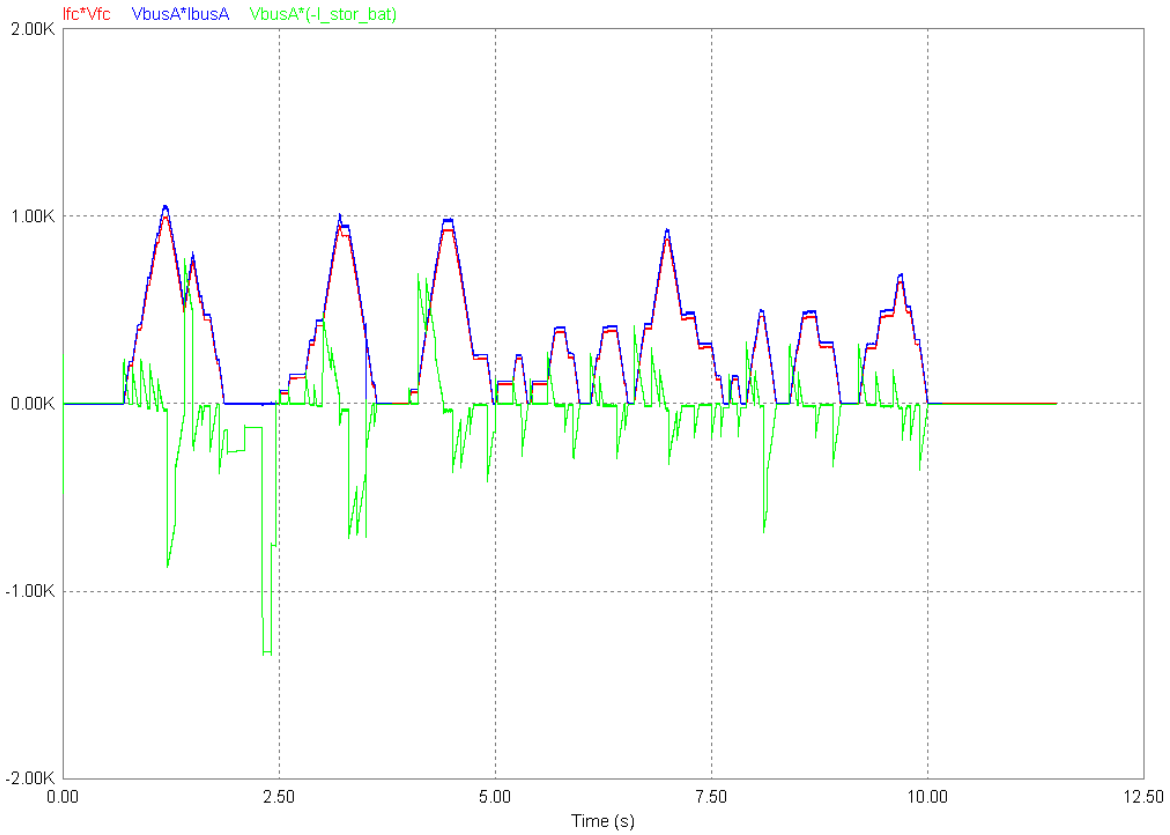

Figure 4.6 Simulation results of power sources in the test bench

Lastly, the SOC of the storage battery is shown in Figure 4.7 to prove that the battery will not overcharge or over-discharge during a normal drive cycle. When the SOC of the storage battery surpasses the pre-determined set point (90%), mechanical braking is implemented and the power surplus provided by the FCE while ramping down to no load will be absorbed by the storage battery. The dramatic increase in the SOC to 97% is caused by the abrupt drop in the power reference. The power requested is originally at about 1000W before going to zero, suddenly leading to mechanical braking. The FCE must ramp down from nearly full power to zero taking about 500ms. During this time, the battery absorbs all of the excess power. This can also be seen in Figure 4.6, when the battery power reverses direction and stays negative for a relatively long time.

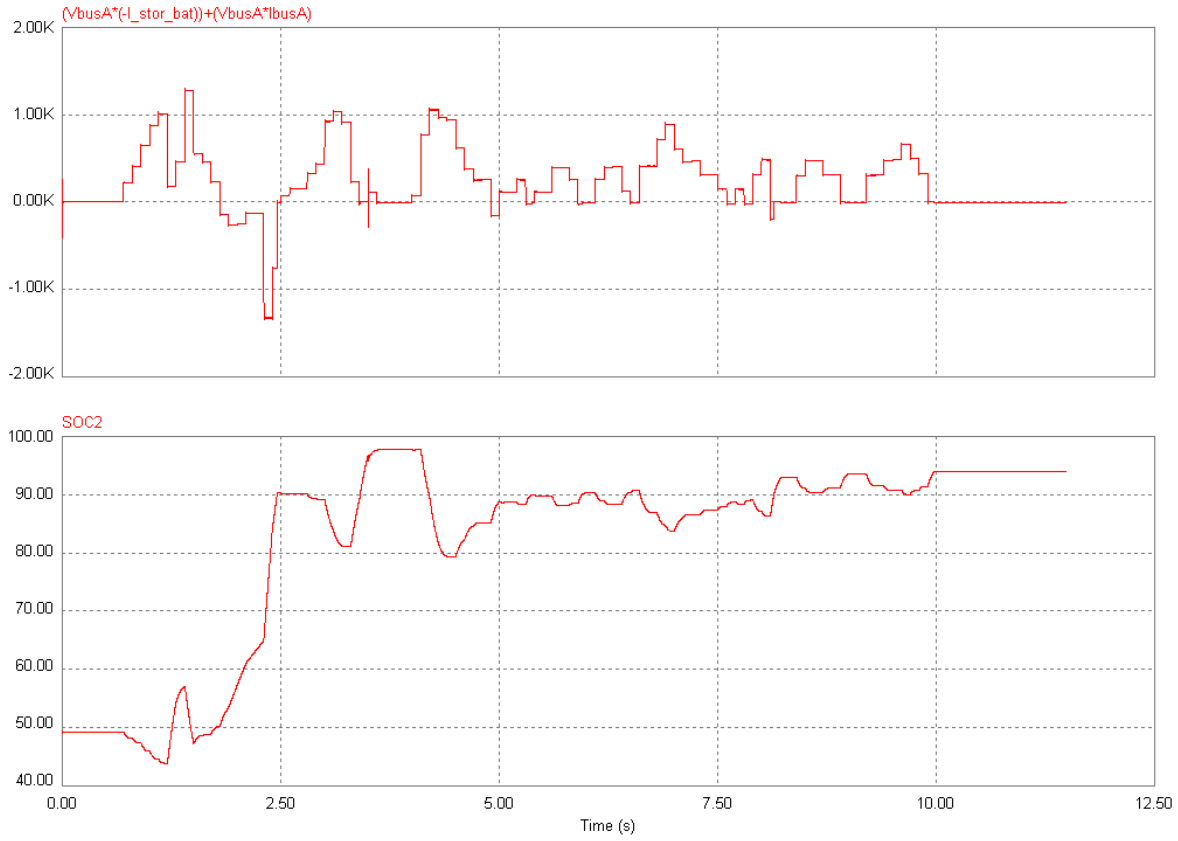

Figure 4.7 Total power provided by the test bench system (top), SOC of storage battery (bottom)

To avoid this problem, one way is to increase the storage capacity of the system by adding another bank of batteries in parallel on the high-voltage DC bus. Advantages to this include allowing for more regenerative braking cycles to occur due to the increased storage capacity. Also changes in the SOC due to the charging and discharging of the batteries are less pronounced; therefore the 10% buffer for storing the residual power from the FCE when it is ramping down is less likely to be needed and this set point at 90% can be more generally used for other drive cycles. The downside to the second battery bank is the added cost and weight to the station making it physically larger as well. The results of the simulation can be seen in Figure 4.8.

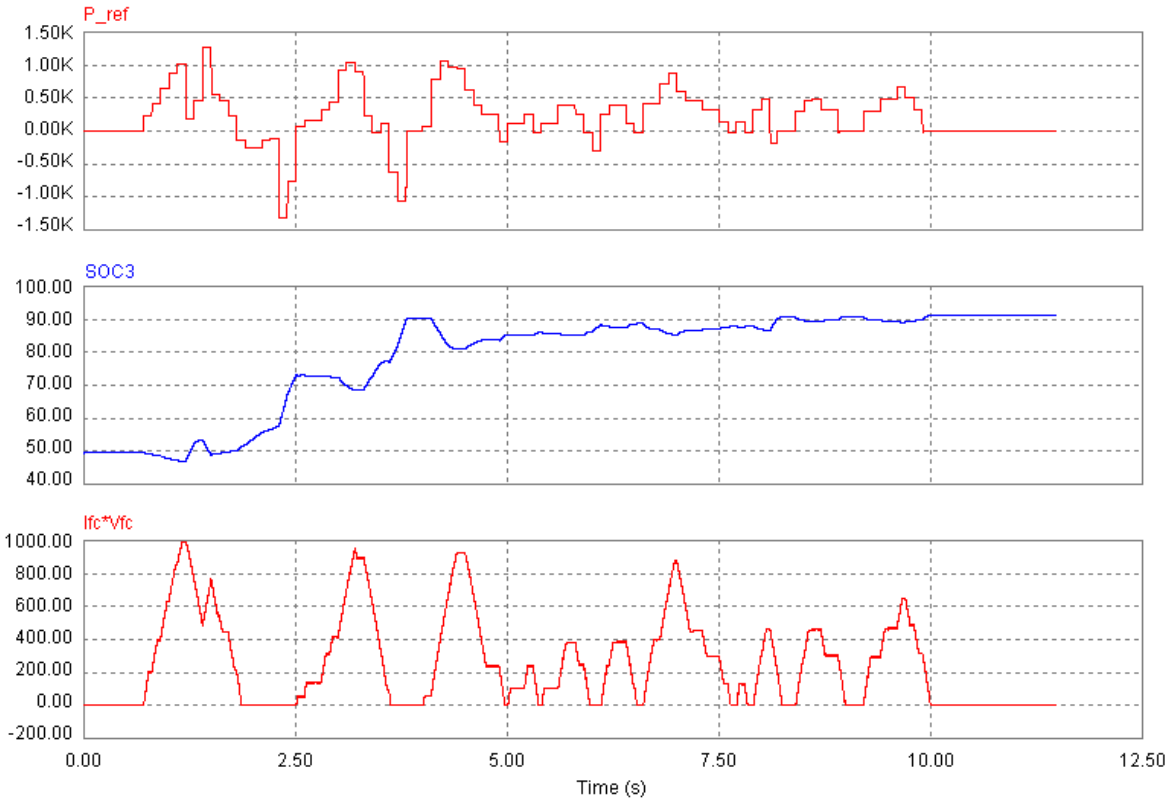

Figure 4.8 Total power provided by the test bench system (top), SOC of storage batteries (middle), power output of the FCE (bottom)

Chapter 5

Conclusions and Future Work

5.1 Summary

This chapter will review the contents of the thesis, assess the conclusions of the research, and suggest ideas for future work.

In chapter 1, the subject of research was introduced and possible power management topologies were discussed. All the topologies that were considered used a fuel cell as the main power source. Most utilized a buck converter to lower the output voltage of the fuel cell to the input voltage of the load. Many attempted to solve the problem of the slow response time of the fuel cell by adding a battery or an ultra-capacitor to the system. The energy storage device was usually connected to the system through a converter which adds components, as well as complexity, and requires extra control. The topology that was chosen for the work reported in this thesis used a boost converter to connect the fuel cell to the high-voltage DC bus. No converter was needed for the battery, which was chosen as the energy storage device, or the load. Both of these components could be connected directly to the high-voltage DC bus because the input voltage of the load and the battery voltage were designed to be the same. Converters were not needed to control the current either. The load had an internal control for the input current, therefore leaving the storage battery current to be controlled naturally by KCL. The goal of this work was to design a test station and demonstrate, through simulation, that it emulates a fuel cell-powered vehicle's drive-train. There are many facets to the test station that were described in chapters 2, 3, and 4.

In chapter 2, the first component of the test station, the fuel cell emulator, was presented. The chapter began with an overview of fuel cells including their history, the different types, and applications in vehicular systems. The operation of a fuel cell was also explained. It was pointed out

that fuel cells are still quite expensive, and thus, using them in all stages of design and development is impractical from an economical point of view, considering the cost of facilities, fuel costs, fuel storage, and running costs of the fuel cell. For such an application, a safer, more cost-effective and time-efficient way to develop a new system using a fuel cell is to use a fuel cell emulator. The FCE design proposed in chapter 2 consisted of a buck converter with some input and output power conditioning. The system was designed for an input voltage of 120V AC. The input power conditioning circuit rectified the 120-V AC input voltage to a 170-V DC voltage and shaped the bridge rectifier DC-side current so that an AC current would be reflected back on the source-side. The input power to the buck converter was delivered at 170V DC. The buck converter was designed to output power in such a way that the terminal voltage and current track the polarization curve of the Nexa Fuel Cell power module from Ballard Power Systems Inc. The output power was then stepped up via a boost converter to connect the FCE to the high-voltage DC bus. The boost converter also implemented a delay to simulate the slow response of the Nexa Fuel Cell module. The results that were shown in section 2.3 illustrate that the FCE indeed reflected the behavior of the Nexa Fuel Cell module.

In chapter 3, the controllable load for the test bench was introduced. Many designs of new "green" vehicles incorporate a regenerative braking system. In order to model this, a bi-directional converter design was needed to not only draw power when the vehicle was driving, but also provide power back to the source during a braking period. A number of bi-directional converters were studied but a simple bi-directional buck-boost converter was chosen for the topology of the load. The high-voltage side is connected to the high-voltage DC bus and the low-voltage side incorporates a parallel resistor-battery combination. It was explained that the converter had two modes of operation. In buck mode, the power reference signal is positive and power flows from the high-voltage side to the low-voltage side. This power either charges the battery or is dissipated in the resistor. In boost mode, the resistor is disconnected and the battery discharges to provide the power, which would be recovered during regenerative braking, back to the high-voltage DC bus. These modes are controlled by the power reference signal which is calculated from the drive cycle. The derivation was shown in section 3.3.1.

The results shown in section 3.4 demonstrate that the load can realize the scaled power of a vehicle with regenerative braking during a given drive cycle.

In chapter 4, the entire test bench topology was discussed. The only component added to the test station that was not previously discussed was the energy storage battery on the high-voltage DC bus. This battery does not need a converter because the battery voltage is the same as the bus voltage and the current supplied or absorbed by the battery is determined automatically according to KCL. Some logic was incorporated to prevent the battery over charging. If the battery's SOC was beyond a set point, then the power reference signal went to zero indicating that the vehicle was performing mechanical braking. If the storage battery is charged beyond its set-point then no more energy can be recovered from the regenerative braking so mechanical braking must be implemented. The results showed that the cooperation of the FCE and the battery makes it possible to provide enough power when the load requests it.

5.2 Conclusions

The following conclusions can be made based on the simulation results obtained for the test station in this thesis:

- The fuel cell emulator developed is able to output power according to the polarization curve of a Nexa power module. The design can be adapted to realize the characteristics of any fuel cell stack. The emulator can be used in design and development of fuel cell-powered hybrid vehicular systems and testing power management algorithms.
- The bi-directional controllable DC load design presented in this thesis is capable of realizing the scaled power of a given vehicle with regenerative braking capability during a given drive cycle within its design limits.
- The test station can be used to design and test different energy storage devices and configurations, together with their converters, that can provide, in cooperation with the fuel cell, the power demands of a vehicular load and perform regenerative braking.

5.3 Suggestions for Future Work

In the following, some options for future work are listed:

- To build an experimental setup of the simulated test bench to ensure that the design will work as expected in a laboratory. Once the concept has been proven experimentally, the design can be refined and optimized.
- To experiment with ultra-capacitors, different types of batteries, or a combination of ultra-capacitors and batteries, and explore the most efficient energy management system.
- To optimize the system from points of view of cost and size.
- To investigate different converter topologies and control strategies in conjunction with energy storage systems composed of batteries and ultra-capacitors.

.

Appendix A

Nexa Fuel Cell Module

The Nexa Fuel Cell module is a compact fuel cell module that is manufactured by Ballard Power Systems Inc. According to [16], "the Nexa power module is a small, low-maintenance and fully-automated fuel cell system designed to be integrated into products for portable and back-up power markets." It encompasses, not only a fuel cell stack, but also all the ancillary systems that the stack needs to function. The ancillary systems include a system to deliver the fuel and oxidant to the reaction sites, a cooling system, and sensors to monitor the system performance. The feedback signals from the sensors are sent to an on-board microprocessor where the measurements are analyzed. The only external support it needs is the hydrogen for the fuel and the air as the oxidant, as well as battery power and a communications link for start up and shut down sequences. The length of operation is limited only by fuel storage capacity. Nexa also produces very little noise and zero harmful gaseous emissions with the only by-product from its operation being water. The product specifications from [16] are listed in tables A-1 and A-2.

Table A-1 Output specifications of the Nexa Fuel Cell Module.

Outputs	Requirement	Definition	Quantity
Power	Rated Power	Capacity at Standard Conditions, BOL	1200W
	Voltage	Operating voltage range	22V to 50V
		Voltage at Rated Power	26V
	Start-up Time	Minimum time to achieve Rated Power from a Cold Start condition	2 minutes
Emissions	Noise	Maximum noise emission at 1m	72dBA
	Water	Maximum quantity of liquid water produced at Rated Power	870mL/hr
Lifetime	Operating Life	Minimum number of operating hours before EOL	1500 hrs
	Cyclic Life	Minimum number of start-up & shut down cycles before EOL	500
	Shelf Life	Minimum storage (non-operation) before EOL	2 years

Table A-2 Input specifications of the Nexa Fuel Cell Module.

Inputs	Requirement	Definition	Quantity
Fuel	Purity	Lowest acceptable concentration of hydrogen	99.99% H_2 (vol)
	Pressure	Allowable range of inlet supply pressure	70-1720 kPa (g)
	Temperature	Allowable range of inlet supply temperature	5°C - 80°C
	Acceptable Impurities	Maximum total inert fluids (including helium, argon, nitrogen and water vapour)	0.01% (vol)
		Maximum CO and CO_2 combined	2 ppm (vol)
		Maximum total hydrocarbon	1 ppm (vol)
		Maximum oxygen	500 ppm (vol
	Consumption	Maximum fuel consumption at Rated Power	<18.5 SLPM
Power Conditioning	Current Ripple	Maximum acceptable current ripple at 120Hz, with respect to average DC net output current	24.7 % RMS 35% peak-peak
DC Power Supply	Voltage	Allowable range of input voltage	18 to 30V
	Power	Maximum Power draw during start up	60W
Operating Environment	Location	Acceptable locations for use	Indoors & Outdoors
	Temperature Range	Range of acceptable ambient cooling air and oxidant air temperatures	3°C to 40°C
	Relative Humidity	Range of acceptable ambient relative humidity	0% to 95% (non-condensing)

Appendix B

Hydrogen Consumption Calculation of the Nexa Fuel Cell Module

This Appendix shows the calculation of hydrogen consumption over the temperature and pressure ranges of the Nexa Fuel Cell which are 278 – 353K and 70-1720 kPa, respectively. The calculations were performed using the flow rate at maximum load. According to [16], the hydrogen consumption at maximum load is 18 SLPM. In chapter 2, the number of moles of hydrogen was calculated at this load level. The calculation is repeated here for convenience. Using the same equations that were given in chapter 2, the flow rate can be calculated in m^3/min, over both pressure and temperature ranges of the Nexa Fuel Cell. A sample calculation using 895kPa and 315K for pressure and temperature is given by (B-1) and (B-2). The data obtained is shown both in tabular form and in chart form. A similar chart and table must be generated every load level on the graph shown in Figure 2.8.

$$n = \frac{pv}{RT} = \frac{(1.013\times10^{5}\,Pa)(18\times10^{-3}\,m^{3})}{(8.31\,J/mol\cdot K)(273K)} = 0.804\,mol/\min \tag{B-1}$$

$$v = \frac{nRT}{p} = \frac{(0.804\,mol/\min)\ (8.31\,J/mol\cdot K)(315K)}{895kPa} = 0.002\,m^{3}/\min \tag{B-2}$$

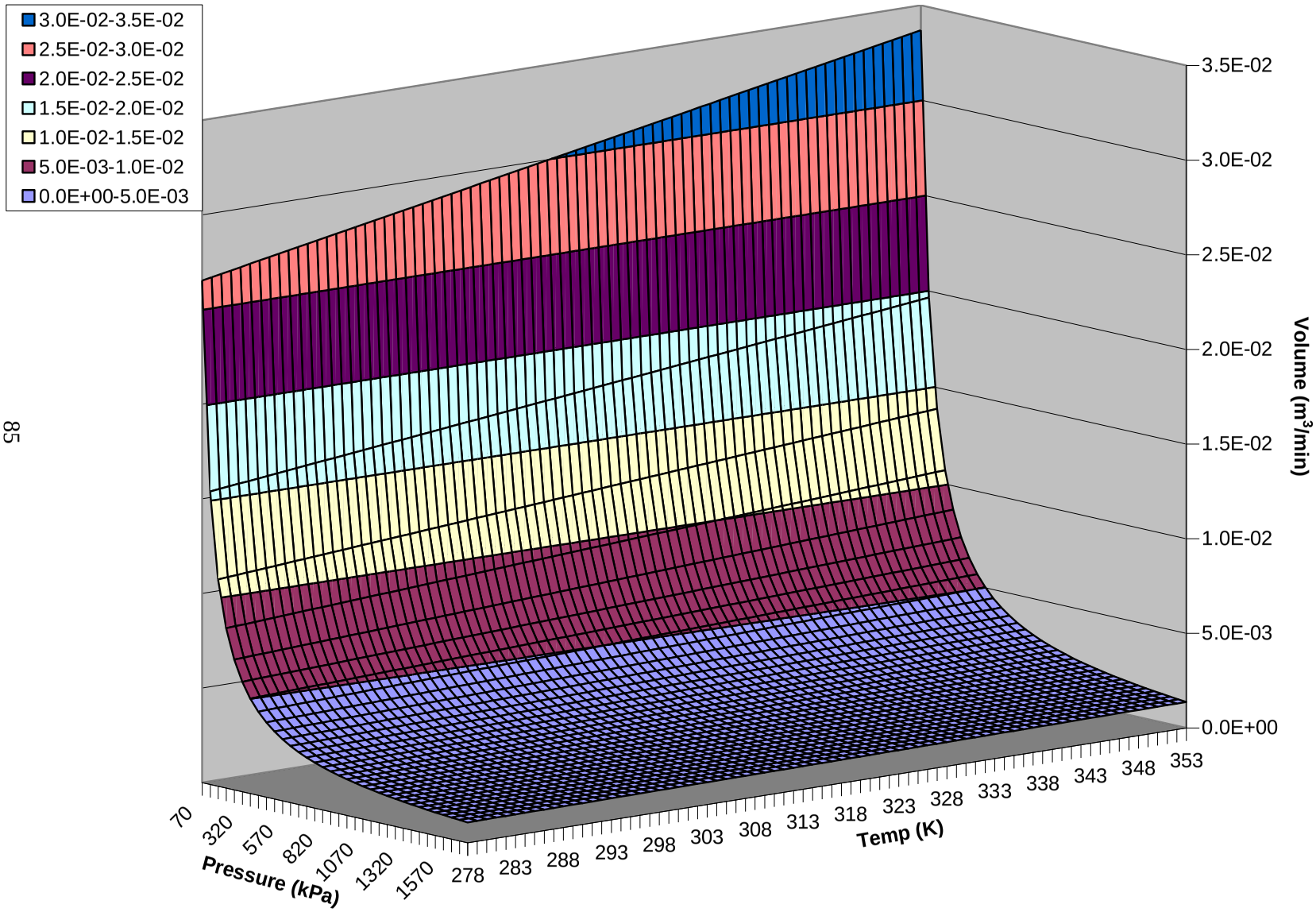

Figure B.1 3-D surface chart of flow rates of the Nexa Fuel Cell at 18 SLPM

Table B-1 Calculations of flow rate at 18 SPLM

Temperature (K)	Pressure (kPa)						
	70	120	170	220	270	320	370
278	2.652E-02	1.547E-02	1.092E-02	8.440E-03	6.877E-03	5.802E-03	5.018E-03
280	2.671E-02	1.558E-02	1.100E-02	8.500E-03	6.926E-03	5.844E-03	5.054E-03
282	2.691E-02	1.570E-02	1.108E-02	8.561E-03	6.976E-03	5.886E-03	5.090E-03
284	2.710E-02	1.581E-02	1.116E-02	8.622E-03	7.025E-03	5.927E-03	5.126E-03
286	2.729E-02	1.592E-02	1.124E-02	8.682E-03	7.075E-03	5.969E-03	5.162E-03
288	2.748E-02	1.603E-02	1.131E-02	8.743E-03	7.124E-03	6.011E-03	5.199E-03
290	2.767E-02	1.614E-02	1.139E-02	8.804E-03	7.173E-03	6.053E-03	5.235E-03
292	2.786E-02	1.625E-02	1.147E-02	8.865E-03	7.223E-03	6.094E-03	5.271E-03
294	2.805E-02	1.636E-02	1.155E-02	8.925E-03	7.272E-03	6.136E-03	5.307E-03
296	2.824E-02	1.647E-02	1.163E-02	8.986E-03	7.322E-03	6.178E-03	5.343E-03
298	2.843E-02	1.659E-02	1.171E-02	9.047E-03	7.371E-03	6.220E-03	5.379E-03
300	2.862E-02	1.670E-02	1.179E-02	9.107E-03	7.421E-03	6.261E-03	5.415E-03
302	2.881E-02	1.681E-02	1.186E-02	9.168E-03	7.470E-03	6.303E-03	5.451E-03
304	2.900E-02	1.692E-02	1.194E-02	9.229E-03	7.520E-03	6.345E-03	5.487E-03
306	2.920E-02	1.703E-02	1.202E-02	9.290E-03	7.569E-03	6.387E-03	5.524E-03
308	2.939E-02	1.714E-02	1.210E-02	9.350E-03	7.619E-03	6.428E-03	5.560E-03
310	2.958E-02	1.725E-02	1.218E-02	9.411E-03	7.668E-03	6.470E-03	5.596E-03
312	2.977E-02	1.736E-02	1.226E-02	9.472E-03	7.718E-03	6.512E-03	5.632E-03
314	2.996E-02	1.748E-02	1.234E-02	9.532E-03	7.767E-03	6.554E-03	5.668E-03
316	3.015E-02	1.759E-02	1.241E-02	9.593E-03	7.817E-03	6.595E-03	5.704E-03
318	3.034E-02	1.770E-02	1.249E-02	9.654E-03	7.866E-03	6.637E-03	5.740E-03
320	3.053E-02	1.781E-02	1.257E-02	9.715E-03	7.916E-03	6.679E-03	5.776E-03
322	3.072E-02	1.792E-02	1.265E-02	9.775E-03	7.965E-03	6.720E-03	5.812E-03
324	3.091E-02	1.803E-02	1.273E-02	9.836E-03	8.014E-03	6.762E-03	5.848E-03
326	3.110E-02	1.814E-02	1.281E-02	9.897E-03	8.064E-03	6.804E-03	5.885E-03
328	3.129E-02	1.826E-02	1.289E-02	9.957E-03	8.113E-03	6.846E-03	5.921E-03
330	3.149E-02	1.837E-02	1.296E-02	1.002E-02	8.163E-03	6.887E-03	5.957E-03
332	3.168E-02	1.848E-02	1.304E-02	1.008E-02	8.212E-03	6.929E-03	5.993E-03
334	3.187E-02	1.859E-02	1.312E-02	1.014E-02	8.262E-03	6.971E-03	6.029E-03
336	3.206E-02	1.870E-02	1.320E-02	1.020E-02	8.311E-03	7.013E-03	6.065E-03
338	3.225E-02	1.881E-02	1.328E-02	1.026E-02	8.361E-03	7.054E-03	6.101E-03
340	3.244E-02	1.892E-02	1.336E-02	1.032E-02	8.410E-03	7.096E-03	6.137E-03
342	3.263E-02	1.903E-02	1.344E-02	1.038E-02	8.460E-03	7.138E-03	6.173E-03
344	3.282E-02	1.915E-02	1.351E-02	1.044E-02	8.509E-03	7.180E-03	6.209E-03
346	3.301E-02	1.926E-02	1.359E-02	1.050E-02	8.559E-03	7.221E-03	6.246E-03
348	3.320E-02	1.937E-02	1.367E-02	1.056E-02	8.608E-03	7.263E-03	6.282E-03
350	3.339E-02	1.948E-02	1.375E-02	1.063E-02	8.658E-03	7.305E-03	6.318E-03
352	3.358E-02	1.959E-02	1.383E-02	1.069E-02	8.707E-03	7.347E-03	6.354E-03

Temperature (K)	Pressure (kPa)						
	420	470	520	570	620	670	720
278	4.421E-03	3.950E-03	3.571E-03	3.257E-03	2.995E-03	2.771E-03	2.579E-03
280	4.452E-03	3.979E-03	3.596E-03	3.281E-03	3.016E-03	2.791E-03	2.597E-03
282	4.484E-03	4.007E-03	3.622E-03	3.304E-03	3.038E-03	2.811E-03	2.616E-03
284	4.516E-03	4.036E-03	3.648E-03	3.328E-03	3.059E-03	2.831E-03	2.634E-03
286	4.548E-03	4.064E-03	3.673E-03	3.351E-03	3.081E-03	2.851E-03	2.653E-03
288	4.580E-03	4.093E-03	3.699E-03	3.375E-03	3.102E-03	2.871E-03	2.671E-03
290	4.612E-03	4.121E-03	3.725E-03	3.398E-03	3.124E-03	2.891E-03	2.690E-03
292	4.643E-03	4.149E-03	3.750E-03	3.421E-03	3.145E-03	2.911E-03	2.709E-03
294	4.675E-03	4.178E-03	3.776E-03	3.445E-03	3.167E-03	2.931E-03	2.727E-03
296	4.707E-03	4.206E-03	3.802E-03	3.468E-03	3.189E-03	2.951E-03	2.746E-03
298	4.739E-03	4.235E-03	3.827E-03	3.492E-03	3.210E-03	2.971E-03	2.764E-03
300	4.771E-03	4.263E-03	3.853E-03	3.515E-03	3.232E-03	2.990E-03	2.783E-03
302	4.802E-03	4.291E-03	3.879E-03	3.539E-03	3.253E-03	3.010E-03	2.801E-03
304	4.834E-03	4.320E-03	3.904E-03	3.562E-03	3.275E-03	3.030E-03	2.820E-03
306	4.866E-03	4.348E-03	3.930E-03	3.585E-03	3.296E-03	3.050E-03	2.838E-03
308	4.898E-03	4.377E-03	3.956E-03	3.609E-03	3.318E-03	3.070E-03	2.857E-03
310	4.930E-03	4.405E-03	3.982E-03	3.632E-03	3.339E-03	3.090E-03	2.876E-03
312	4.961E-03	4.434E-03	4.007E-03	3.656E-03	3.361E-03	3.110E-03	2.894E-03
314	4.993E-03	4.462E-03	4.033E-03	3.679E-03	3.382E-03	3.130E-03	2.913E-03
316	5.025E-03	4.490E-03	4.059E-03	3.703E-03	3.404E-03	3.150E-03	2.931E-03
318	5.057E-03	4.519E-03	4.084E-03	3.726E-03	3.426E-03	3.170E-03	2.950E-03
320	5.089E-03	4.547E-03	4.110E-03	3.749E-03	3.447E-03	3.190E-03	2.968E-03
322	5.120E-03	4.576E-03	4.136E-03	3.773E-03	3.469E-03	3.210E-03	2.987E-03
324	5.152E-03	4.604E-03	4.161E-03	3.796E-03	3.490E-03	3.230E-03	3.005E-03
326	5.184E-03	4.632E-03	4.187E-03	3.820E-03	3.512E-03	3.250E-03	3.024E-03
328	5.216E-03	4.661E-03	4.213E-03	3.843E-03	3.533E-03	3.270E-03	3.043E-03
330	5.248E-03	4.689E-03	4.238E-03	3.867E-03	3.555E-03	3.290E-03	3.061E-03
332	5.279E-03	4.718E-03	4.264E-03	3.890E-03	3.576E-03	3.309E-03	3.080E-03
334	5.311E-03	4.746E-03	4.290E-03	3.914E-03	3.598E-03	3.329E-03	3.098E-03
336	5.343E-03	4.775E-03	4.315E-03	3.937E-03	3.619E-03	3.349E-03	3.117E-03
338	5.375E-03	4.803E-03	4.341E-03	3.960E-03	3.641E-03	3.369E-03	3.135E-03
340	5.407E-03	4.831E-03	4.367E-03	3.984E-03	3.663E-03	3.389E-03	3.154E-03
342	5.438E-03	4.860E-03	4.393E-03	4.007E-03	3.684E-03	3.409E-03	3.172E-03
344	5.470E-03	4.888E-03	4.418E-03	4.031E-03	3.706E-03	3.429E-03	3.191E-03
346	5.502E-03	4.917E-03	4.444E-03	4.054E-03	3.727E-03	3.449E-03	3.210E-03
348	5.534E-03	4.945E-03	4.470E-03	4.078E-03	3.749E-03	3.469E-03	3.228E-03
350	5.566E-03	4.974E-03	4.495E-03	4.101E-03	3.770E-03	3.489E-03	3.247E-03
352	5.597E-03	5.002E-03	4.521E-03	4.124E-03	3.792E-03	3.509E-03	3.265E-03

Temperature (K)	Pressure (kPa)					
	770	820	870	920	970	1020
278	2.411E-03	2.264E-03	2.134E-03	2.018E-03	1.914E-03	1.820E-03
280	2.429E-03	2.281E-03	2.149E-03	2.033E-03	1.928E-03	1.833E-03
282	2.446E-03	2.297E-03	2.165E-03	2.047E-03	1.942E-03	1.846E-03
284	2.463E-03	2.313E-03	2.180E-03	2.062E-03	1.955E-03	1.860E-03
286	2.481E-03	2.329E-03	2.196E-03	2.076E-03	1.969E-03	1.873E-03
288	2.498E-03	2.346E-03	2.211E-03	2.091E-03	1.983E-03	1.886E-03
290	2.515E-03	2.362E-03	2.226E-03	2.105E-03	1.997E-03	1.899E-03
292	2.533E-03	2.378E-03	2.242E-03	2.120E-03	2.011E-03	1.912E-03
294	2.550E-03	2.395E-03	2.257E-03	2.134E-03	2.024E-03	1.925E-03
296	2.567E-03	2.411E-03	2.272E-03	2.149E-03	2.038E-03	1.938E-03
298	2.585E-03	2.427E-03	2.288E-03	2.163E-03	2.052E-03	1.951E-03
300	2.602E-03	2.443E-03	2.303E-03	2.178E-03	2.066E-03	1.964E-03
302	2.619E-03	2.460E-03	2.318E-03	2.192E-03	2.079E-03	1.977E-03
304	2.637E-03	2.476E-03	2.334E-03	2.207E-03	2.093E-03	1.991E-03
306	2.654E-03	2.492E-03	2.349E-03	2.221E-03	2.107E-03	2.004E-03
308	2.671E-03	2.509E-03	2.364E-03	2.236E-03	2.121E-03	2.017E-03
310	2.689E-03	2.525E-03	2.380E-03	2.250E-03	2.134E-03	2.030E-03
312	2.706E-03	2.541E-03	2.395E-03	2.265E-03	2.148E-03	2.043E-03
314	2.724E-03	2.557E-03	2.410E-03	2.279E-03	2.162E-03	2.056E-03
316	2.741E-03	2.574E-03	2.426E-03	2.294E-03	2.176E-03	2.069E-03
318	2.758E-03	2.590E-03	2.441E-03	2.309E-03	2.190E-03	2.082E-03
320	2.776E-03	2.606E-03	2.457E-03	2.323E-03	2.203E-03	2.095E-03
322	2.793E-03	2.623E-03	2.472E-03	2.338E-03	2.217E-03	2.108E-03
324	2.810E-03	2.639E-03	2.487E-03	2.352E-03	2.231E-03	2.121E-03
326	2.828E-03	2.655E-03	2.503E-03	2.367E-03	2.245E-03	2.135E-03
328	2.845E-03	2.671E-03	2.518E-03	2.381E-03	2.258E-03	2.148E-03
330	2.862E-03	2.688E-03	2.533E-03	2.396E-03	2.272E-03	2.161E-03
332	2.880E-03	2.704E-03	2.549E-03	2.410E-03	2.286E-03	2.174E-03
334	2.897E-03	2.720E-03	2.564E-03	2.425E-03	2.300E-03	2.187E-03
336	2.914E-03	2.737E-03	2.579E-03	2.439E-03	2.313E-03	2.200E-03
338	2.932E-03	2.753E-03	2.595E-03	2.454E-03	2.327E-03	2.213E-03
340	2.949E-03	2.769E-03	2.610E-03	2.468E-03	2.341E-03	2.226E-03
342	2.966E-03	2.786E-03	2.625E-03	2.483E-03	2.355E-03	2.239E-03
344	2.984E-03	2.802E-03	2.641E-03	2.497E-03	2.369E-03	2.252E-03
346	3.001E-03	2.818E-03	2.656E-03	2.512E-03	2.382E-03	2.266E-03
348	3.018E-03	2.834E-03	2.671E-03	2.526E-03	2.396E-03	2.279E-03
350	3.036E-03	2.851E-03	2.687E-03	2.541E-03	2.410E-03	2.292E-03
352	3.053E-03	2.867E-03	2.702E-03	2.555E-03	2.424E-03	2.305E-03

Temperature (K)	Pressure (kPa)					
	1070	1120	1170	1220	1270	1320
278	1.735E-03	1.658E-03	1.587E-03	1.522E-03	1.462E-03	1.407E-03
280	1.748E-03	1.670E-03	1.598E-03	1.533E-03	1.472E-03	1.417E-03
282	1.760E-03	1.682E-03	1.610E-03	1.544E-03	1.483E-03	1.427E-03
284	1.773E-03	1.694E-03	1.621E-03	1.555E-03	1.494E-03	1.437E-03
286	1.785E-03	1.705E-03	1.633E-03	1.566E-03	1.504E-03	1.447E-03
288	1.798E-03	1.717E-03	1.644E-03	1.577E-03	1.515E-03	1.457E-03
290	1.810E-03	1.729E-03	1.655E-03	1.588E-03	1.525E-03	1.467E-03
292	1.823E-03	1.741E-03	1.667E-03	1.599E-03	1.536E-03	1.477E-03
294	1.835E-03	1.753E-03	1.678E-03	1.609E-03	1.546E-03	1.488E-03
296	1.848E-03	1.765E-03	1.690E-03	1.620E-03	1.557E-03	1.498E-03
298	1.860E-03	1.777E-03	1.701E-03	1.631E-03	1.567E-03	1.508E-03
300	1.873E-03	1.789E-03	1.712E-03	1.642E-03	1.578E-03	1.518E-03
302	1.885E-03	1.801E-03	1.724E-03	1.653E-03	1.588E-03	1.528E-03
304	1.898E-03	1.813E-03	1.735E-03	1.664E-03	1.599E-03	1.538E-03
306	1.910E-03	1.825E-03	1.747E-03	1.675E-03	1.609E-03	1.548E-03
308	1.922E-03	1.837E-03	1.758E-03	1.686E-03	1.620E-03	1.558E-03
310	1.935E-03	1.849E-03	1.770E-03	1.697E-03	1.630E-03	1.568E-03
312	1.947E-03	1.861E-03	1.781E-03	1.708E-03	1.641E-03	1.579E-03
314	1.960E-03	1.872E-03	1.792E-03	1.719E-03	1.651E-03	1.589E-03
316	1.972E-03	1.884E-03	1.804E-03	1.730E-03	1.662E-03	1.599E-03
318	1.985E-03	1.896E-03	1.815E-03	1.741E-03	1.672E-03	1.609E-03
320	1.997E-03	1.908E-03	1.827E-03	1.752E-03	1.683E-03	1.619E-03
322	2.010E-03	1.920E-03	1.838E-03	1.763E-03	1.693E-03	1.629E-03
324	2.022E-03	1.932E-03	1.849E-03	1.774E-03	1.704E-03	1.639E-03
326	2.035E-03	1.944E-03	1.861E-03	1.785E-03	1.714E-03	1.649E-03
328	2.047E-03	1.956E-03	1.872E-03	1.796E-03	1.725E-03	1.660E-03
330	2.060E-03	1.968E-03	1.884E-03	1.807E-03	1.735E-03	1.670E-03
332	2.072E-03	1.980E-03	1.895E-03	1.817E-03	1.746E-03	1.680E-03
334	2.085E-03	1.992E-03	1.907E-03	1.828E-03	1.756E-03	1.690E-03
336	2.097E-03	2.004E-03	1.918E-03	1.839E-03	1.767E-03	1.700E-03
338	2.110E-03	2.016E-03	1.929E-03	1.850E-03	1.777E-03	1.710E-03
340	2.122E-03	2.027E-03	1.941E-03	1.861E-03	1.788E-03	1.720E-03
342	2.135E-03	2.039E-03	1.952E-03	1.872E-03	1.799E-03	1.730E-03
344	2.147E-03	2.051E-03	1.964E-03	1.883E-03	1.809E-03	1.741E-03
346	2.160E-03	2.063E-03	1.975E-03	1.894E-03	1.820E-03	1.751E-03
348	2.172E-03	2.075E-03	1.986E-03	1.905E-03	1.830E-03	1.761E-03
350	2.185E-03	2.087E-03	1.998E-03	1.916E-03	1.841E-03	1.771E-03
352	2.197E-03	2.099E-03	2.009E-03	1.927E-03	1.851E-03	1.781E-03

Temperature (K)	Pressure (kPa)			
	1370	1420	1470	1520
278	1.355E-03	1.308E-03	1.263E-03	1.222E-03
280	1.365E-03	1.317E-03	1.272E-03	1.230E-03
282	1.375E-03	1.326E-03	1.281E-03	1.239E-03
284	1.384E-03	1.336E-03	1.290E-03	1.248E-03
286	1.394E-03	1.345E-03	1.299E-03	1.257E-03
288	1.404E-03	1.355E-03	1.308E-03	1.265E-03
290	1.414E-03	1.364E-03	1.318E-03	1.274E-03
292	1.423E-03	1.373E-03	1.327E-03	1.283E-03
294	1.433E-03	1.383E-03	1.336E-03	1.292E-03
296	1.443E-03	1.392E-03	1.345E-03	1.301E-03
298	1.453E-03	1.402E-03	1.354E-03	1.309E-03
300	1.462E-03	1.411E-03	1.363E-03	1.318E-03
302	1.472E-03	1.420E-03	1.372E-03	1.327E-03
304	1.482E-03	1.430E-03	1.381E-03	1.336E-03
306	1.492E-03	1.439E-03	1.390E-03	1.345E-03
308	1.501E-03	1.449E-03	1.399E-03	1.353E-03
310	1.511E-03	1.458E-03	1.408E-03	1.362E-03
312	1.521E-03	1.467E-03	1.418E-03	1.371E-03
314	1.531E-03	1.477E-03	1.427E-03	1.380E-03
316	1.540E-03	1.486E-03	1.436E-03	1.388E-03
318	1.550E-03	1.496E-03	1.445E-03	1.397E-03
320	1.560E-03	1.505E-03	1.454E-03	1.406E-03
322	1.570E-03	1.514E-03	1.463E-03	1.415E-03
324	1.579E-03	1.524E-03	1.472E-03	1.424E-03
326	1.589E-03	1.533E-03	1.481E-03	1.432E-03
328	1.599E-03	1.543E-03	1.490E-03	1.441E-03
330	1.609E-03	1.552E-03	1.499E-03	1.450E-03
332	1.618E-03	1.562E-03	1.508E-03	1.459E-03
334	1.628E-03	1.571E-03	1.517E-03	1.468E-03
336	1.638E-03	1.580E-03	1.527E-03	1.476E-03
338	1.648E-03	1.590E-03	1.536E-03	1.485E-03
340	1.657E-03	1.599E-03	1.545E-03	1.494E-03
342	1.667E-03	1.609E-03	1.554E-03	1.503E-03
344	1.677E-03	1.618E-03	1.563E-03	1.512E-03
346	1.687E-03	1.627E-03	1.572E-03	1.520E-03
348	1.696E-03	1.637E-03	1.581E-03	1.529E-03
350	1.706E-03	1.646E-03	1.590E-03	1.538E-03
352	1.716E-03	1.656E-03	1.599E-03	1.547E-03

Temperature (K)	Pressure (kPa)			
	1570	1620	1670	1720
278	1.183E-03	1.146E-03	1.112E-03	1.079E-03
280	1.191E-03	1.154E-03	1.120E-03	1.087E-03
282	1.200E-03	1.163E-03	1.128E-03	1.095E-03
284	1.208E-03	1.171E-03	1.136E-03	1.103E-03
286	1.217E-03	1.179E-03	1.144E-03	1.111E-03
288	1.225E-03	1.187E-03	1.152E-03	1.118E-03
290	1.234E-03	1.196E-03	1.160E-03	1.126E-03
292	1.242E-03	1.204E-03	1.168E-03	1.134E-03
294	1.251E-03	1.212E-03	1.176E-03	1.142E-03
296	1.259E-03	1.220E-03	1.184E-03	1.149E-03
298	1.268E-03	1.229E-03	1.192E-03	1.157E-03
300	1.276E-03	1.237E-03	1.200E-03	1.165E-03
302	1.285E-03	1.245E-03	1.208E-03	1.173E-03
304	1.293E-03	1.253E-03	1.216E-03	1.180E-03
306	1.302E-03	1.262E-03	1.224E-03	1.188E-03
308	1.310E-03	1.270E-03	1.232E-03	1.196E-03
310	1.319E-03	1.278E-03	1.240E-03	1.204E-03
312	1.327E-03	1.286E-03	1.248E-03	1.211E-03
314	1.336E-03	1.295E-03	1.256E-03	1.219E-03
316	1.344E-03	1.303E-03	1.264E-03	1.227E-03
318	1.353E-03	1.311E-03	1.272E-03	1.235E-03
320	1.361E-03	1.319E-03	1.280E-03	1.243E-03
322	1.370E-03	1.328E-03	1.288E-03	1.250E-03
324	1.378E-03	1.336E-03	1.296E-03	1.258E-03
326	1.387E-03	1.344E-03	1.304E-03	1.266E-03
328	1.395E-03	1.352E-03	1.312E-03	1.274E-03
330	1.404E-03	1.360E-03	1.320E-03	1.281E-03
332	1.412E-03	1.369E-03	1.328E-03	1.289E-03
334	1.421E-03	1.377E-03	1.336E-03	1.297E-03
336	1.429E-03	1.385E-03	1.344E-03	1.305E-03
338	1.438E-03	1.393E-03	1.352E-03	1.312E-03
340	1.446E-03	1.402E-03	1.360E-03	1.320E-03
342	1.455E-03	1.410E-03	1.368E-03	1.328E-03
344	1.463E-03	1.418E-03	1.376E-03	1.336E-03
346	1.472E-03	1.426E-03	1.384E-03	1.344E-03
348	1.480E-03	1.435E-03	1.392E-03	1.351E-03
350	1.489E-03	1.443E-03	1.400E-03	1.359E-03
352	1.497E-03	1.451E-03	1.408E-03	1.367E-03

Bibliography

[1] "Alternative Fuels," http://www.oee.nrcan.gc.ca/transportation/personal/vehicle_fuels.cfm, accessed on March 6, 2008.

[2] G. Liu, W. Yu, and Z. Tu, "Power Management for Alleviation of the Impact on PEM Fuel Cell due to Load Fluctuation" in *Proceedings of the 6th International Conference on Intelligent Systems Design and Applications*, Piscataway, NJ, USA, vol. 1, October 2006, pp. 1104-1110.

[3] A. Ohkawa, "Electric Power Control System for a Fuel Cell Vehicle Employing Electric Double-Layer Capacitor" in *SAE International 2004 World Congress and Exhibition*, Detroit, MI, USA, pp. 21-27.

[4] L. Solero, A. Lidozzi, and J. A. Pomilio, "Design of Multiple-Input Power converter for Hybrid Vehicles" in *IEEE Transactions on Power Electronics*, vol. 20, issue 5, Sept. 2005, pp. 1007 – 1016.

[5] Z. Jiang, "Power Management of Hybrid Photovoltaic-Fuel Cell Power Systems" in *IEEE Power Engineering Society General Meeting 2006*, 18-22 June 2006, pp.1-6.

[6] G. Hoogers, Ed., *Fuel Cell Technology Handbook*. New York: CRC Press, 2003.

[6] F. Babir, *PEM Fuel Cells: Theory and Practice*. New York: Elsevier Academic Press, 2005.

[8] D. Hakim, New York Times, "Technology; GM Announces Plans For Fuel Cells," published: Aug. 8, 2001, http://query.nytimes.com/gst/fullpage.html?res=990DE3DD163FF93BA3575BC0A9679C8B63.

[9] "Fuel Economy and Alternative Fuels," http://www.gm.com/explore/fuel_economy/, accessed on March 27, 2008.

[10] J. Larminie, A. Dicks, *Fuel Cell Systems Explained, 2nd ed*. West Sussex, John Wiley & Sons Inc. 2003.

[11] J. Correa. F. A. Farret, J. R. Gomes, M. G. Simoes, "Simulation of Fuel-Cell Stacks using a Computer-Controlled Power Rectifier With the Purposes of Actual High-Power Injection Applications," in *IEEE Transactions on Industry Applications*, vol. 39, no. 4, July 2003, pp. 1136-1142.

[12] R. H. Thring, ed., *Fuel Cells for Automotive Applications*. New York: American Society of Mechanical Engineers Press, 2004.

[13] J. Marshall, M. Kazerani, "Design of an Efficient Fuel Cell Vehicle Drive Train, Featuring a Novel Boost Converter," *in 32nd Annual Conference of IEEE Industrial Electronics Society*, 2005, Page(s): 1229-1234.

[14] N. Mohan, T. Undeland, W. Robbins, *Power Electronics: Converters, Applications, and Design, 2nd ed.* New York: John Wiley & Sons Inc. 1995.

[15] M. Kazerani, T. Pan, "Improving Performance of Isolated Fuel Cell Power Conditioners Through Series Capacitive Compensation," in *Society of Automotive Engineers Power Systems Conference* 2004.

[16] Ballard Power System Technical Staff, *Nexa Power Module User Manual*, Ballard Power Systems Inc. 2003.

[17] D. Halliday, R. Resnick, J. Walker, *Fundementals of Physics, 7th ed.* New York: John Wiley & Sons, Inc. 2005.

[18] M. Kazerani, "Active Input Current Waveshaping Techniques for Single-Phase Front-End Diode Rectifiers," M.S. thesis, Concordia University, Montreal, QC, 1990.

[19] F. Wicks, K. Donnelly, "Modeling Regenerative Braking and Storage for Vehicles" *in Proceedings of the 32nd Intersociety of the Energy Conversion Engineering Conference*, 1997 Vol. 3, page(s) 2030-2035.

[20] Z. Chuanwei, B. Zhifeng, C. Binggang, L. Jingcheng, "Study on Regenerative Braking of

Electric Vehicle," *The 4th International Power Electronics and Motion Control Conference*, 2004 Volume 2, page(s): 836- 839.

[21] M. Kazerani, "A High-Performance Controllable DC Load", in *Proceedings of 2007 International Symposium on Industrial Electronics*, 2007.

[22] K. Jin, X. Ruan, M. Yang, M. Xu, "A Novel Hybrid Fuel Cell Power System", in *37th IEEE Proceedings of the Power Electronics Specialists Conference*, 2006. Page(s):1 – 7.

[23] S. Jang, T. Lee, W. Lee, C. Won, "Bi-directional DC-DC Converter for Fuel Cell Generation System", in *IEEE 35th Annual* Power Electronics Specialists Conference, 2004, Vol. 6, Page(s): 4722 – 4728.

[24] S. Inoue, H. Akagi "A Bidirectional DC–DC Converter for an Energy Storage System With Galvanic Isolation", in *IEEE Transactions on Power Electronics*, 2007, Vol. 22, No. 6, pp. 2299-2306.

[25] A. R. Bergen, V. Vittal, *Power Systems Analysis 2nd ed*. Singapore: Addison Wesley Longman Pte.Ltd, 2000.

[26] Environmental Protection Agency, "Federal Test Procedure Revisions," http://www.epa.gov/otaq/sftp.htm#cycles, accessed 07/19/07.

[27] P. Smith, "Braking,"http://www.safespeed.org.uk/braking.html, accessed 04/04/08.